

1    SSWD-EvoEpi: A Coupled Eco-Evolutionary  
2    Epidemiological Model  
3    for Sea Star Wasting Disease in *Pycnopodia*  
4    *helianthoides*

5    Technical Report — Model Development and Sensitivity Analysis

6    Willem Weertman<sup>1,2</sup>

<sup>1</sup>Department of Psychology, University of Washington, Seattle, WA

<sup>2</sup>Friday Harbor Laboratories, University of Washington, Friday Harbor, WA

7    February 21, 2026

8    **Abstract**

9    Sea star wasting disease (SSWD) caused one of the largest wildlife mass mor-  
10    tality events in marine ecosystems, driving the sunflower sea star (*Pycnopodia he-*  
11    *lianthoides*) to a 90.6% range-wide decline and IUCN Critically Endangered sta-  
12    tus. The recent identification of *Vibrio pectenicida* strain FHCF-3 as a causative  
13    agent, combined with active captive breeding and the first experimental outplanting  
14    of captive-bred juveniles, creates an urgent need for quantitative tools to guide  
15    recovery. We present SSWD-EvoEpi, an individual-based, spatially explicit eco-  
16    evolutionary epidemiological model coupling *V. pectenicida* transmission dynamics  
17    with polygenic host evolution under sweepstakes reproductive success. Each agent  
18    carries a diploid genotype across 51 loci governing three fitness-related traits — re-  
19    sistance (immune exclusion), tolerance (damage limitation), and recovery (pathogen  
20    clearance) — that evolve in response to disease-driven selection. Disease dynamics  
21    follow an SEIR compartmental structure with an environmental pathogen reser-  
22    voir, pathogen evolution along a virulence—transmission tradeoff, and temperature-  
23    dependent forcing. Reproduction implements sweepstakes reproductive success with  
24     $N_e/N \sim 10^{-3}$ , sex-asymmetric spawning induction, and post-spawning immuno-  
25    suppression. Four rounds of global sensitivity analysis (Morris screening and Sobol  
26    variance decomposition) across up to 47 parameters reveal that model behavior  
27    is dominated by nonlinear interactions among disease mortality rate, host suscep-  
28    tibility, environmental pathogen pressure, and genetic architecture, with recovery

29 trait evolution emerging as the fastest adaptive response. The model provides a  
30 framework for evaluating captive-bred release strategies, assisted gene flow, and the  
31 feasibility of evolutionary rescue on conservation-relevant timescales.

# 32 Contents

33	<b>1 Introduction</b>	7
34	1.1 Sea Star Wasting Disease and the Collapse of <i>Pycnopodia helianthoides</i> . . . . .	7
35	1.2 Etiology: A Decade-Long Mystery Resolved . . . . .	7
36	1.3 Conservation Urgency and Active Recovery Efforts . . . . .	8
37	1.4 The Need for an Eco-Evolutionary Framework . . . . .	9
38	1.5 Model Overview . . . . .	10
39	1.6 Paper Outline . . . . .	11
40	<b>2 Model Architecture</b>	11
41	2.1 Agent Representation . . . . .	11
42	2.2 Node Structure . . . . .	13
43	2.3 Simulation Loop . . . . .	13
44	2.4 Design Rationale . . . . .	14
45	<b>3 Disease Module</b>	15
46	3.1 Compartmental Structure . . . . .	15
47	3.1.1 Erlang-Distributed Stage Durations . . . . .	16
48	3.2 Force of Infection . . . . .	16
49	3.2.1 Dose–Response Function . . . . .	17
50	3.2.2 Salinity Modifier . . . . .	17
51	3.2.3 Size-Dependent Susceptibility . . . . .	17
52	3.2.4 Post-Spawning Immunosuppression . . . . .	18
53	3.3 Disease Progression and Recovery . . . . .	18
54	3.3.1 Transition Rates . . . . .	18
55	3.3.2 Temperature Scaling (Arrhenius) . . . . .	18
56	3.3.3 Tolerance: Extending $I_2$ Duration . . . . .	19
57	3.3.4 Recovery . . . . .	19
58	3.4 Vibrio Dynamics . . . . .	20
59	3.4.1 Shedding . . . . .	20
60	3.4.2 Carcass Shedding . . . . .	20
61	3.4.3 Vibrio Decay . . . . .	20
62	3.4.4 Environmental Reservoir . . . . .	21
63	3.5 Pathogen Evolution . . . . .	21
64	3.5.1 Virulence–Tradeoff Curves . . . . .	21
65	3.5.2 Transmission and Mutation . . . . .	22
66	3.6 Basic Reproduction Number . . . . .	22
67	3.7 Daily Update Sequence . . . . .	22

68	<b>4 Genetics Module</b>	<b>23</b>
69	4.1 Three-Trait Architecture . . . . .	23
70	4.2 Trait Score Computation . . . . .	24
71	4.2.1 Effect Size Distribution . . . . .	24
72	4.2.2 Coupling to Disease Dynamics . . . . .	25
73	4.3 Genotype Initialization . . . . .	25
74	4.4 Mendelian Inheritance and Mutation . . . . .	26
75	4.5 Sweepstakes Reproductive Success . . . . .	26
76	4.6 Genetic Diagnostics and Tracking . . . . .	27
77	4.7 Genotype Bank (Tier 2 Nodes) . . . . .	28
78	<b>5 Population Dynamics</b>	<b>28</b>
79	5.1 Life Stages . . . . .	28
80	5.2 Growth . . . . .	29
81	5.3 Natural Mortality . . . . .	29
82	5.4 Spawning System . . . . .	30
83	5.4.1 Spawning Season and Phenology . . . . .	30
84	5.4.2 Spontaneous Spawning . . . . .	31
85	5.4.3 Cascade Induction . . . . .	31
86	5.4.4 Post-Spawning Immunosuppression . . . . .	32
87	5.5 Fecundity . . . . .	32
88	5.6 Fertilization Kinetics and the Allee Effect . . . . .	32
89	5.7 Larval Phase . . . . .	33
90	5.8 Settlement and Recruitment . . . . .	33
91	5.9 Continuous Settlement . . . . .	34
92	5.10 Demographic–Genetic–Epidemiological Coupling . . . . .	34
93	<b>6 Spatial Module and Environmental Forcing</b>	<b>35</b>
94	6.1 Metapopulation Network Structure . . . . .	35
95	6.1.1 Node Definition . . . . .	35
96	6.1.2 Internode Distance Computation . . . . .	36
97	6.2 Connectivity Matrices . . . . .	37
98	6.2.1 Larval Connectivity Matrix <b>C</b> . . . . .	37
99	6.2.2 Pathogen Dispersal Matrix <b>D</b> . . . . .	37
100	6.2.3 Dispersal Dynamics . . . . .	38
101	6.3 Environmental Forcing . . . . .	38
102	6.3.1 Sea Surface Temperature . . . . .	39
103	6.3.2 Temperature-Dependent Rate Scaling . . . . .	39
104	6.3.3 Salinity Modifier . . . . .	40

105	6.3.4 Flushing Rate . . . . .	40
106	6.4 Agent Movement . . . . .	41
107	6.5 Network Configurations . . . . .	41
108	6.5.1 5-Node Validation Network . . . . .	41
109	6.5.2 11-Node Sensitivity Analysis Network . . . . .	42
110	6.5.3 Full-Range Network (Planned) . . . . .	43
111	6.6 Network Construction . . . . .	43
112	<b>7 Sensitivity Analysis</b>	<b>44</b>
113	7.1 Methods . . . . .	44
114	7.1.1 Morris Elementary Effects Screening . . . . .	44
115	7.1.2 Sobol Variance Decomposition . . . . .	44
116	7.1.3 Output Metrics . . . . .	45
117	7.2 Progressive Sensitivity Analysis Design . . . . .	45
118	7.3 Round 4 Morris Results . . . . .	47
119	7.3.1 Global Parameter Ranking . . . . .	47
120	7.3.2 Key Rank Shifts from Round 3 . . . . .	48
121	7.3.3 New Three-Trait Parameters . . . . .	51
122	7.3.4 Universal Nonlinearity . . . . .	51
123	7.3.5 Module-Level Sensitivity . . . . .	52
124	7.4 Cross-Round Parameter Trajectories . . . . .	53
125	7.5 Sobol Variance Decomposition: Rounds 1–2 and Ongoing . . . . .	54
126	7.5.1 R1–R2 Sobol Results . . . . .	54
127	7.5.2 Round 4 Sobol (In Progress) . . . . .	55
128	7.6 Summary and Implications . . . . .	55
129	<b>8 Validation</b>	<b>60</b>
130	8.1 K = 5,000 Validation . . . . .	60
131	8.2 K = 100,000 Scale-Up Validation . . . . .	63
132	8.3 Cross-Scale Comparison . . . . .	64
133	8.4 Key Scientific Findings . . . . .	65
134	8.4.1 Evolutionary Rescue Is Insufficient . . . . .	65
135	8.4.2 Recovery as the Primary Adaptive Pathway . . . . .	66
136	8.4.3 The Extinction Vortex Persists at Realistic Scales . . . . .	66
137	8.4.4 Implications for Captive Breeding . . . . .	67
138	<b>9 Discussion</b>	<b>68</b>
139	9.1 Summary of Contributions . . . . .	68
140	9.2 Comparison with Clement et al. (2024) . . . . .	69
141	9.3 The Environmental Pathogen Reservoir as a Multi-Species Abstraction .	70

142	9.4 Conservation Implications . . . . .	71
143	9.4.1 Evolutionary Rescue Is Too Slow . . . . .	71
144	9.4.2 Recovery Trait as a Breeding Target . . . . .	71
145	9.4.3 Release Site Selection . . . . .	72
146	9.5 Model Limitations . . . . .	72
147	9.6 Future Directions . . . . .	73
148	9.6.1 ABC-SMC Calibration . . . . .	73
149	9.6.2 Conservation Scenario Evaluation . . . . .	73
150	9.6.3 Full Coastline Network . . . . .	74
151	9.6.4 Integration with Empirical Data . . . . .	74
152	9.7 Conclusions . . . . .	74
153	<b>A Parameter Tables</b>	<b>81</b>

<sub>154</sub> **1 Introduction**

<sub>155</sub> **1.1 Sea Star Wasting Disease and the Collapse of *Pycnopodia*  
<sub>156</sub> *helianthoides***

<sub>157</sub> Sea star wasting disease (SSWD) caused one of the largest documented wildlife mass  
<sub>158</sub> mortality events in marine ecosystems when it swept through populations of over 20  
<sub>159</sub> asteroid species along the northeastern Pacific coast beginning in 2013 [24, 31, 50]. The  
<sub>160</sub> disease, characterized by behavioral changes (arm twisting, lethargy), loss of turgor,  
<sub>161</sub> body wall lesions, ray autotomy, and rapid tissue degradation, devastated populations  
<sub>162</sub> from Baja California to the Gulf of Alaska within months [34, 49]. Among the species  
<sub>163</sub> affected, the sunflower sea star (*Pycnopodia helianthoides*) suffered the most catastrophic  
<sub>164</sub> decline, losing an estimated 5.75 billion individuals and experiencing a 90.6% range-wide  
<sub>165</sub> population reduction based on 61,043 surveys across 31 datasets [20, 26]. Along the outer  
<sub>166</sub> coast from Washington to Baja California, declines exceeded 97%, with many regions  
<sub>167</sub> recording zero individuals in subsequent surveys [20, 23]. The species was assessed as  
<sub>168</sub> Critically Endangered by the IUCN in 2021 [20] and is under consideration for listing as  
<sub>169</sub> Threatened under the U.S. Endangered Species Act [42].

<sub>170</sub> As a large-bodied, mobile, generalist predator capable of consuming sea urchins at  
<sub>171</sub> rates sufficient to structure entire subtidal communities, *Pycnopodia helianthoides* func-  
<sub>172</sub> tions as a keystone species in northeastern Pacific kelp forest ecosystems [6, 15, 47].  
<sub>173</sub> Its precipitous decline has been linked to cascading trophic effects, including sea urchin  
<sub>174</sub> population explosions and extensive kelp forest deforestation, with northern California  
<sub>175</sub> losing 96% of its kelp canopy since the 2014 marine heatwave [48, 55]. The loss of this  
<sub>176</sub> apex predator thus represents not only a conservation crisis for a single species but a  
<sub>177</sub> destabilization of an entire marine ecosystem [23, 39].

<sub>178</sub> **1.2 Etiology: A Decade-Long Mystery Resolved**

<sub>179</sub> For over a decade following the initial outbreak, the causative agent of SSWD remained  
<sub>180</sub> contested. An early hypothesis implicating sea star associated densovirus (SSaDV; Hew-  
<sub>181</sub> son et al. 31) was subsequently retracted after repeated failures to reproduce the original  
<sub>182</sub> challenge experiments and the discovery that the virus is endemic in healthy echinoderm  
<sub>183</sub> populations worldwide [32–34]. An alternative hypothesis invoking boundary layer oxygen  
<sub>184</sub> depletion (BLODL) at the animal–water interface proposed that microbial respiration on  
<sub>185</sub> sea star surfaces draws down dissolved oxygen, leading to tissue hypoxia [2, 29]. While  
<sub>186</sub> this mechanism may contribute to disease susceptibility, it did not identify a specific  
<sub>187</sub> pathogen.

<sub>188</sub> The breakthrough came with Prentice et al. [53], who fulfilled Koch’s postulates by  
<sub>189</sub> demonstrating that *Vibrio pectenicida* strain FHCF-3, a Gram-negative marine bac-

terium, is a causative agent of SSWD in *Pycnopodia helianthoides*. Through seven controlled exposure experiments using captive-bred, quarantined sea stars, the authors showed that injection of cultured *V. pectenicida* FHCF-3 into the coelomic cavity reliably produced disease signs — arm twisting, lesion formation, autotomy, and death within approximately two weeks. Heat-treated and 0.22 µm filtered controls remained healthy, confirming a living bacterial agent. Critically, the pathogen was re-isolated from experimentally infected animals, completing Koch’s postulates. Earlier investigations had missed *V. pectenicida* because they sampled body wall tissue rather than coelomic fluid, where the bacterium resides.

However, the etiological picture is not entirely resolved. Hewson [30] demonstrated that *V. pectenicida* FHCF-3 was not consistently detected in non-*Pycnopodia helianthoides* species during the 2013–2014 mass mortality, suggesting it may be specific to *Pycnopodia helianthoides* or may function as an opportunistic pathogen rather than a universal SSWD agent across all affected asteroid taxa. The bacterium also exhibits explosive growth in the presence of decaying echinoderm tissue, raising questions about whether it acts primarily as a pathogen or a saprobe under different conditions [30]. Nonetheless, for *Pycnopodia helianthoides* — the focus of this study — the evidence for *V. pectenicida* as the primary causative agent is robust. The identification of a specific bacterial pathogen with known temperature-dependent growth dynamics [45] provides a mechanistic basis for modeling disease transmission and environmental forcing.

### 1.3 Conservation Urgency and Active Recovery Efforts

The failure of *Pycnopodia helianthoides* populations to recover naturally in the decade following the initial epizootic — contrasting with partial recovery observed in some co-occurring asteroid species [19] — has motivated intensive conservation action. The species’ long generation time (~30 years), broadcast spawning reproductive strategy, and vulnerability to Allee effects at low density [16, 43] compound the challenge of natural recovery. Historical precedent is sobering: the Caribbean long-spined sea urchin *Diadema antillarum*, which suffered a comparable 93–100% mass mortality in 1983–1984, achieved only ~12% recovery after three decades [40]. Another asteroid, *Heliaster kubiniji*, has never recovered from a 1975 mass mortality event in the Gulf of California [12].

In response, a coordinated multi-partner recovery effort has emerged. The Association of Zoos and Aquariums (AZA) Saving Animals From Extinction (SAFE) program maintains over 2,500 captive juveniles and 130+ reproductive adults across 17 AZA institutions [5]. The first experimental outplanting of captive-bred *Pycnopodia helianthoides* occurred in December 2025 in Monterey, California, with 47 of 48 juveniles surviving after four weeks [64]. A Roadmap to Recovery developed by over 30 leading experts defines regionally nested recovery objectives, from local demographic benchmarks to range-wide

227 genetic structure targets [26]. Cryopreservation of gametes has been demonstrated for a  
228 congener and is under development for *Pycnopodia helianthoides* to enable assisted gene  
229 flow from genetically diverse founders [22, 61]. In 2025, the California Ocean Protection  
230 Council approved \$630,000 in funding for captive breeding, disease diagnostics, and ex-  
231 perimental outplanting [7]. A reference genome has also been published [60], laying the  
232 groundwork for genome-wide association studies (GWAS) to identify resistance loci.

233 These recovery efforts require quantitative predictions: How many captive-bred in-  
234 dividuals should be released, where, and when? What are the genetic consequences of  
235 releasing animals from a limited captive founder population? Can natural selection drive  
236 resistance evolution fast enough to matter on conservation timescales? How do pathogen  
237 evolution, environmental change, and spatial structure interact to shape recovery trajec-  
238 tories? Answering these questions demands a modeling framework that integrates disease  
239 dynamics with population genetics in an explicitly spatial context.

## 240 1.4 The Need for an Eco-Evolutionary Framework

241 Existing models of SSWD dynamics have focused on either epidemiological or ecological  
242 aspects in isolation. Aalto et al. [1] coupled an SIR-type model with ocean circulation to  
243 explain the rapid continental-scale spread of SSWD, finding that temperature-dependent  
244 mortality best matched observed patterns. Tolimieri [66] conducted a population viability  
245 analysis using stage-structured matrix models but did not incorporate disease dynamics or  
246 host genetics. Arroyo-Esquivel et al. [4] recently modeled epidemiological consequences of  
247 managed reintroduction following disease-driven host decline, but their framework lacks  
248 genetic evolution. None of these approaches captures the interplay between disease-driven  
249 selection, host genetic adaptation, and demographic recovery that is central to predicting  
250 conservation outcomes.

251 The theoretical motivation for coupling these processes is compelling. Mass mortal-  
252 ity events impose intense directional selection on host populations [58], and in *Pisaster*  
253 *ochraceus* — a co-occurring sea star affected by SSWD — rapid allele frequency shifts  
254 ( $\Delta q \approx 0.08\text{--}0.15$  at outlier loci) were detected within a single generation of the epi-  
255 zotic, with geographic consistency across sites indicating selection rather than drift [58].  
256 However, in broadcast-spawning marine invertebrates, the genetic consequences of mass  
257 mortality are filtered through sweepstakes reproductive success (SRS), whereby variance  
258 in individual reproductive success is so large that effective population size ( $N_e$ ) is orders  
259 of magnitude smaller than census size ( $N_e/N \sim 10^{-3}$ ; Árnason et al. 3, Hedgecock and  
260 Pudovkin 27). SRS amplifies genetic drift on ecological timescales [67], can facilitate rapid  
261 adaptation when coupled with bottlenecks [14], and generates chaotic genetic patchiness  
262 that confounds simple predictions of evolutionary trajectories. Any model of evolutionary  
263 rescue in *Pycnopodia helianthoides* must therefore account for this fundamental feature

264 of marine broadcast spawner genetics.

265 The closest methodological precedent is the eco-evolutionary individual-based model  
266 (IBM) developed by Clement et al. [10] for coevolution between Tasmanian devils (*Sar-*  
267 *cophilus harrisii*) and devil facial tumour disease (DFTD). That model coupled an SEI  
268 epidemiological framework with polygenic quantitative genetics, parameterized from two  
269 decades of field data and GWAS results, and found a high probability of host persistence  
270 over 50 generations through coevolutionary dynamics. Our model extends this approach  
271 to a marine system with fundamentally different reproductive biology — broadcast spawn-  
272 ing with sweepstakes reproductive success, external fertilization subject to Allee effects,  
273 and a pelagic larval phase mediating spatial connectivity — challenges that no existing  
274 eco-evolutionary disease model has addressed.

## 275 1.5 Model Overview

276 We present SSWD-EvoEpi, an individual-based, spatially explicit, eco-evolutionary epi-  
277 demiological model designed to simulate SSWD dynamics and evolutionary responses in  
278 *Pycnopodia helianthoides* metapopulations across the northeastern Pacific. The model  
279 tracks individual sea stars as agents within a network of habitat nodes connected by larval  
280 dispersal and pathogen transport. Each agent carries a diploid genotype across 51 loci  
281 governing three fitness-related traits: resistance ( $r_i$ , 17 loci; immune exclusion reducing  
282 infection probability), tolerance ( $t_i$ , 17 loci; damage limitation extending survival dur-  
283 ing late-stage infection), and recovery ( $c_i$ , 17 loci; pathogen clearance enabling transition  
284 from infected to recovered states). Per-locus allele frequencies are drawn from a Beta(2,8)  
285 distribution, reflecting polygenic architecture with most loci at low frequency [36].

286 Disease dynamics follow an SEIR-type compartmental structure with exposed (E),  
287 early infected ( $I_1$ ), and late infected ( $I_2$ ) stages, coupled with an environmental pathogen  
288 reservoir (P) whose dynamics are temperature-dependent [18, 45]. Pathogen evolution  
289 is modeled through a heritable virulence phenotype that evolves along a mechanistic  
290 tradeoff curve linking shedding rate to host survival duration. Reproduction incorpo-  
291 rates sweepstakes reproductive success via a heavy-tailed offspring distribution producing  
292  $N_e/N$  ratios consistent with empirical estimates for marine broadcast spawners [27], with  
293 sex-asymmetric spawning induction and post-spawning immunosuppression derived from  
294 species-specific observations. Spatial connectivity is implemented through distinct larval  
295 exchange and pathogen dispersal matrices computed from overwater distances across the  
296 model domain.

297 The model is implemented in Python with NumPy-vectorized agent operations, achiev-  
298 ing sufficient performance for large-scale sensitivity analysis and calibration (75,000 agents  
299 across 150 nodes in  $\sim 72$  s). Four rounds of sensitivity analysis using Morris screening and  
300 Sobol variance decomposition across up to 47 parameters have identified the key drivers of

301 model behavior, revealing strong nonlinear interactions and highlighting priority targets  
302 for empirical calibration.

## 303 1.6 Paper Outline

304 The remainder of this paper is organized as follows. Section 2 describes the overall model  
305 architecture, agent representation, and simulation flow. Sections 3–6 detail the disease,  
306 genetics, population dynamics, and spatial modules, respectively. Section 7 presents four  
307 rounds of global sensitivity analysis, identifying the parameters with greatest influence  
308 on epidemiological, demographic, and evolutionary outcomes. Section 8 describes model  
309 validation against available empirical data. Section 9 synthesizes findings, discusses lim-  
310 itations, and outlines the path toward calibrated conservation scenario evaluation. Pa-  
311 rameter tables and supplementary analyses are provided in Appendix A.

## 312 2 Model Architecture

313 SSWD-EvoEpi is an individual-based model (IBM) that couples epidemiological, demo-  
314 graphic, genetic, and spatial dynamics to simulate the eco-evolutionary consequences of  
315 sea star wasting disease in *Pycnopodia helianthoides*. Each agent represents a single sea  
316 star tracked through its complete life history, carrying a diploid genotype at 51 loci that  
317 determines three quantitative defense traits against *Vibrio pectenicida*. We chose an  
318 individual-based approach over compartmental (ODE/PDE) models because SSWD dy-  
319 namics depend critically on individual-level heterogeneity in genetic resistance, body size,  
320 spatial position, and disease stage—features that compartmental models cannot represent  
321 without substantial loss of biological realism [11, 21].

### 322 2.1 Agent Representation

323 Each individual is represented as a record in a NumPy structured array (`AGENT_DTYPE`)  
324 comprising approximately 59 bytes per agent. Table 1 summarizes the principal state  
325 variables grouped by functional module.

Table 1: Agent state variables in SSWD-EvoEpi.

Module	Field	Description
Spatial	x, y	Position within node habitat (m)
	heading	Movement heading (rad)
	speed	Instantaneous speed ( $\text{m min}^{-1}$ )
	node_id	Home node index
Life history	size	Arm-tip diameter (mm)
	age	Age (years, fractional)
	stage	Life stage (0–4; Table 2)
	sex	Sex (0 = female, 1 = male)
Disease	disease_state	Compartment (S/E/I <sub>1</sub> /I <sub>2</sub> /D/R)
	disease_timer	Days remaining in current disease stage
Genetics	resistance	Resistance score $r_i \in [0, 1]$
	tolerance	Tolerance score $t_i \in [0, 1]$
	recovery_ability	Recovery/clearance score $c_i \in [0, 1]$
Spawning	has_spawned	Bout count this season
	immunosuppression_timer	Post-spawning immunosuppression (days)
Administrative	alive	Active flag
	origin	Wild / captive-bred / AGF / wild-source
	pathogen_virulence	Virulence of infecting strain $v_i$

326 Genotypes are stored in a separate array of shape  $(N_{\text{max}}, 51, 2)$  with `int8` entries,  
 327 where axis 1 indexes loci and axis 2 indexes the two allele copies (diploid). This separation  
 328 from the agent record improves cache performance during non-genetic operations (disease  
 329 transmission, movement), which need not touch the genotype array.

 Table 2: Life stages and size thresholds for *Pycnopodia helianthoides*.

Index	Stage	Size threshold (mm)	Reproductive
0	Egg/Larva	—	No
1	Settler	Settlement	No
2	Juvenile	$\geq 10$	No
3	Subadult	$\geq 150$	No
4	Adult	$\geq 400$	Yes

330 **2.2 Node Structure**

331 The spatial domain is represented as a metapopulation network of  $K$  discrete habitat  
332 nodes. Each node encapsulates:

- 333 • A population of agents (structured array + genotype array), initialized at local  
334 carrying capacity;
- 335 • Environmental state: sea surface temperature  $T(t)$  (sinusoidal annual cycle with  
336 warming trend), salinity  $S$ , and tidal flushing rate  $\phi_k$ ;
- 337 • A local Vibrio concentration  $P_k(t)$  (bacteria mL<sup>-1</sup>);
- 338 • Node metadata: latitude, habitat area, fjord classification.

339 Inter-node coupling occurs through two connectivity matrices:

- 340 1. **Pathogen dispersal matrix D**: governs daily exchange of waterborne *Vibrio*  
341 *pectenicida* between nodes, parameterized with an exponential distance kernel (scale  
342  $D_P = 15$  km);
- 343 2. **Larval connectivity matrix C**: governs annual dispersal of competent larvae  
344 among nodes, parameterized with a broader kernel (scale  $D_L = 400$  km) reflecting  
345 the extended pelagic larval duration of *Pycnopodia helianthoides*.

346 **2.3 Simulation Loop**

347 The simulation advances in daily timesteps ( $\Delta t = 1$  day) nested within an annual cycle.  
348 At each daily step, the following operations are executed in sequence at every node  
349 (Figure ??):

- 350 1. **Environment update.** Compute  $T_k(t)$  from a sinusoidal annual SST function  
351 with linear warming trend; update flushing rate  $\phi_k$  (seasonally modulated for fjord  
352 nodes); salinity is constant per node.
- 353 2. **Movement.** Agents execute a correlated random walk (CRW) with 24 hourly  
354 substeps per day. Movement speed is modulated by disease state ( $\times 0.5$  for I<sub>1</sub>,  $\times 0.1$   
355 for I<sub>2</sub>,  $\times 0$  for D). Elastic boundary reflection constrains agents within the habitat.
- 356 3. **Disease dynamics.** Vibrio concentration is updated via an Euler step of the  
357 pathogen ODE. Susceptible agents are exposed to a force of infection that depends  
358 on local pathogen density, individual resistance, salinity, and body size. Infected  
359 agents progress through the SEIPD+R compartments with Erlang-distributed stage  
360 durations (Section 3).

- 361    4. **Pathogen dispersal.** Vibrio is exchanged between neighboring nodes via the **D**  
 362    matrix, representing waterborne transport.
- 363    5. **Settlement.** Larval cohorts whose pelagic larval duration (PLD) has elapsed are  
 364    settled into the local population via Beverton–Holt density-dependent recruitment,  
 365    modulated by an adult-presence settlement cue (Allee effect).
- 366    6. **Spawning.** During the spawning season (November–July), reproductively mature  
 367    adults spawn stochastically with daily probability modulated by a seasonal Gaus-  
 368    sian envelope centered on the peak spawning day. Female and male multi-bout  
 369    spawning, sex-asymmetric cascade induction, and post-spawning immunosuppres-  
 370    sion are modeled explicitly.
- 371    7. **Daily demographics.** Natural mortality is applied as a daily probability con-  
 372    verted from stage-specific annual survival rates:

$$p_{\text{death,daily}} = 1 - S_{\text{annual}}^{1/365}, \quad (1)$$

373    with a senescence overlay for individuals exceeding the senescence age ( $\tau_{\text{sen}} = 50 \text{ yr}$ ).  
 374    Growth follows the von Bertalanffy differential form with daily-scaled stochastic  
 375    noise; stage transitions are one-directional based on size thresholds (Table 2).

376    At the end of each simulated year, an annual step performs:

- 377    1. **Larval dispersal** via the connectivity matrix **C**: unsettled cohorts from all nodes  
 378    are pooled, redistributed probabilistically among destination nodes, and settled at  
 379    receiving nodes or retained in a pending queue for next-year daily settlement.
- 380    2. **Disease introduction** (at the designated epidemic year): a fixed number of agents  
 381    per node are seeded in the Exposed (E) compartment.
- 382    3. **Genetic recording**: per-node allele frequencies, additive genetic variance  $V_A$ , and  
 383    trait means are logged annually. Pre- and post-epidemic allele frequency snapshots  
 384    are captured for calibration against genomic data.

## 385    2.4 Design Rationale

386    Several design choices distinguish SSWD-EvoEpi from previous SSWD models:

387    **Individual-based representation.** SSWD mortality is strongly size-dependent [OR  
 388    = 1.23 per 10 mm; 13], genetically mediated [59], and spatially heterogeneous. A compart-  
 389    mental SIR/SEIR model would require aggregating these axes of variation into homoge-  
 390    neous classes, losing the emergent eco-evolutionary dynamics that arise from individual

391 heterogeneity in resistance, tolerance, and recovery. Following Clement et al. [9], who  
392 demonstrated that individual-based eco-evolutionary models are essential for predicting  
393 host-pathogen coevolution in Tasmanian devil facial tumor disease, we track each indi-  
394 vidual’s genotype, phenotype, and infection history explicitly.

395 **Continuous daily demographics.** Rather than applying mortality, growth, and re-  
396 production as annual pulses, SSWD-EvoEpi evaluates natural mortality and growth daily  
397 (Eq. 1), with spawning resolved to individual daily events across a multi-month season.  
398 This avoids artificial synchronization artifacts and allows disease-demography interac-  
399 tions (e.g., post-spawning immunosuppression) to operate on their natural timescales.

400 **Separated genotype storage.** The 51-locus diploid genotype array (102 bytes per  
401 agent) is stored separately from the agent state record. This ensures that the most  
402 frequently accessed fields during daily disease and movement updates (position, disease  
403 state, size) occupy contiguous memory, improving CPU cache performance by a factor of  
404  $\sim 2\text{--}3 \times$  in profiled benchmarks.

405 **Three-trait genetic architecture.** The 51 loci are partitioned into three indepen-  
406 dently segregating trait blocks of 17 loci each, controlling resistance (immune exclusion),  
407 tolerance (damage limitation), and recovery (pathogen clearance). This architecture  
408 captures the empirical observation that host defense against infectious disease operates  
409 through mechanistically distinct pathways that can evolve semi-independently [54].

## 410 3 Disease Module

411 The disease module implements a stochastic, environmentally driven SEIPD+R (Susceptible–  
412 Exposed–Infectious<sub>1</sub>–Infectious<sub>2</sub>–Dead, plus Recovered) compartmental framework oper-  
413 ating at the individual level. Each agent carries its own disease state, countdown timer,  
414 genetic defense traits ( $r_i, t_i, c_i$ ), and (when pathogen evolution is enabled) the virulence  
415 phenotype  $v_i$  of its infecting strain. Disease dynamics are resolved daily at each spatial  
416 node, coupled to the environmental forcing module for temperature-dependent rates and  
417 to the genetics module for individual susceptibility.

### 418 3.1 Compartmental Structure

419 The disease pathway consists of five compartments plus a recovery state (Figure ??):

- 420 • **S (Susceptible):** Healthy, at risk of infection.
- 421 • **E (Exposed):** Latently infected; not yet shedding pathogen. Duration is Erlang-  
422 distributed with shape  $k_E = 3$ .

- **I<sub>1</sub> (Early infectious):** Pre-symptomatic shedding at rate  $\sigma_1(T)$ . Duration is Erlang-distributed with shape  $k_{I_1} = 2$ . Agents with high clearance ability ( $c_i > 0.5$ ) may recover early.
- **I<sub>2</sub> (Late infectious):** Symptomatic wasting with high shedding rate  $\sigma_2(T)$ . Duration is Erlang-distributed with shape  $k_{I_2} = 2$ . Agents may recover with probability  $p_{\text{rec}} = \rho_{\text{rec}} \times c_i$  per day.
- **D (Dead from disease):** Carcass continues to shed pathogen saprophytically for a 3-day window at rate  $\sigma_D$ .
- **R (Recovered):** Immune; functionally equivalent to S for demographics but not susceptible to reinfection.

### 433 3.1.1 Erlang-Distributed Stage Durations

434 Durations in compartments E, I<sub>1</sub>, and I<sub>2</sub> are drawn from Erlang distributions rather than  
 435 geometric (exponential) distributions. The Erlang distribution with shape parameter  $k$   
 436 and rate parameter  $k\mu$  has mean  $1/\mu$  and coefficient of variation  $CV = 1/\sqrt{k}$ , producing  
 437 more realistic, peaked duration distributions compared to the memoryless exponential  
 438 [69]. For each individual entering a compartment, a duration is sampled as:

$$\tau \sim \text{Erlang}(k, k\mu(T)), \quad \text{rounded to } \max(1, \text{round}(\tau)) \text{ days}, \quad (2)$$

439 where  $\mu(T)$  is the temperature-dependent transition rate at the current SST (Section 3.3.2).  
 440 The shape parameters are:

$$k_E = 3 \quad (CV = 0.58), \quad k_{I_1} = 2 \quad (CV = 0.71), \quad k_{I_2} = 2 \quad (CV = 0.71). \quad (3)$$

441 Timers count down by one each day; when the timer reaches zero, the agent transitions  
 442 to the next compartment.

## 443 3.2 Force of Infection

444 The per-individual instantaneous hazard rate of infection is:

$$\lambda_i = a_{\text{exp}} \underbrace{\frac{P_k}{K_{1/2} + P_k}}_{\text{dose-response}} \underbrace{(1 - r_i)}_{\text{resistance}} \underbrace{S_{\text{sal}}}_{\text{salinity}} \underbrace{f_{\text{size}}(L_i)}_{\text{size}}, \quad (4)$$

445 where:

- $a_{\text{exp}} = 0.75 \text{ d}^{-1}$  is the baseline exposure rate;

- 447     •  $P_k$  is the local Vibrio concentration (bacteria mL<sup>-1</sup>) at node  $k$ ;
- 448     •  $K_{1/2} = 87,000$  bacteria mL<sup>-1</sup> is the half-infective dose (Michaelis–Menten dose–  
449       response);
- 450     •  $r_i \in [0, 1]$  is the individual’s resistance score (immune exclusion; Section 4);
- 451     •  $S_{\text{sal}}$  is the salinity modifier (Section 3.2.2);
- 452     •  $f_{\text{size}}(L_i)$  is the size-dependent susceptibility modifier (Section 3.2.3).

453     The discrete daily probability of infection is:

$$p_{\text{inf}} = 1 - \exp(-\lambda_i \Delta t), \quad \Delta t = 1 \text{ day.} \quad (5)$$

### 454     3.2.1 Dose–Response Function

455     Pathogen exposure follows a Michaelis–Menten (saturating) dose–response:

$$D(P_k) = \frac{P_k}{K_{1/2} + P_k}. \quad (6)$$

456     At low concentrations ( $P_k \ll K_{1/2}$ ), infection probability scales linearly with pathogen  
457       density; at high concentrations ( $P_k \gg K_{1/2}$ ), it saturates at  $D \rightarrow 1$ , reflecting physiolog-  
458       ical limits on pathogen uptake.

### 459     3.2.2 Salinity Modifier

460     Vibrio viability is suppressed at low salinities, providing a mechanistic basis for the  
461       reduced SSWD prevalence observed in fjord systems:

$$S_{\text{sal}} = \begin{cases} 0 & \text{if } S \leq S_{\text{min}} = 10 \text{ psu,} \\ \left( \frac{S - S_{\text{min}}}{S_{\text{full}} - S_{\text{min}}} \right)^{\eta} & \text{if } S_{\text{min}} < S < S_{\text{full}}, \\ 1 & \text{if } S \geq S_{\text{full}} = 28 \text{ psu,} \end{cases} \quad (7)$$

462     where  $\eta = 2$  produces a convex response (low salinity is strongly protective).

### 463     3.2.3 Size-Dependent Susceptibility

464     Larger *Pycnopodia helianthoides* are more susceptible to SSWD, consistent with the em-  
465       pirical finding of Eisenlord et al. [13] (odds ratio 1.23 per 10 mm increase in radius). The  
466       size modifier is:

$$f_{\text{size}}(L_i) = \exp\left(\beta_L \frac{L_i - \bar{L}}{\sigma_L}\right), \quad (8)$$

467 where  $\beta_L = 0.021 \text{ mm}^{-1}$  ( $= \ln 1.23/10$ ),  $\bar{L} = 300 \text{ mm}$  is the reference size, and  $\sigma_L =$   
468  $100 \text{ mm}$  normalizes the deviation. An individual of diameter  $L_i = 500 \text{ mm}$  has  $\sim 1.5 \times$  the  
469 infection hazard of a  $300 \text{ mm}$  individual.

#### 470 3.2.4 Post-Spawning Immunosuppression

471 Spawning imposes a transient immune cost. Following each spawning event, an individual  
472 enters a 28-day immunosuppression window during which its effective resistance is  
473 reduced:

$$r_{i,\text{eff}} = \frac{r_i}{\psi_{\text{spawn}}}, \quad \psi_{\text{spawn}} = 2.0, \quad (9)$$

474 clamped to  $[0, 1]$ . This halves effective resistance during the immunosuppressed period,  
475 creating an evolutionary coupling between reproductive investment and disease vulnera-  
476 bility.

### 477 3.3 Disease Progression and Recovery

478 Disease progression rates are temperature-dependent via an Arrhenius function (Sec-  
479 tion 3.3.2). At each daily step, disease timers are decremented; when a timer reaches  
480 zero, the agent transitions to the next state. Recovery can occur before timer expiry.

#### 481 3.3.1 Transition Rates

482 The base progression rates at reference temperature  $T_{\text{ref}} = 20^\circ\text{C}$  are:

$$\mu_{E \rightarrow I_1} = 0.57 \text{ d}^{-1} \quad (E_a/R = 4,000 \text{ K}), \quad (10)$$

$$\mu_{I_1 \rightarrow I_2} = 0.40 \text{ d}^{-1} \quad (E_a/R = 5,000 \text{ K}), \quad (11)$$

$$\mu_{I_2 \rightarrow D} = 0.173 \text{ d}^{-1} \quad (E_a/R = 2,000 \text{ K}). \quad (12)$$

483 The activation energy for  $I_2 \rightarrow D$  is notably lower ( $E_a/R = 2,000 \text{ K}$  vs.  $5,000\text{--}6,000 \text{ K}$  for  
484 other transitions), reflecting evidence that terminal wasting is less temperature-sensitive  
485 than earlier disease stages (Errata E1).

#### 486 3.3.2 Temperature Scaling (Arrhenius)

487 All temperature-dependent rates are scaled via the Arrhenius equation:

$$k(T) = k_{\text{ref}} \exp \left[ \frac{E_a}{R} \left( \frac{1}{T_{\text{ref}}} - \frac{1}{T} \right) \right], \quad (13)$$

488 where  $T_{\text{ref}} = 293.15 \text{ K}$  ( $20^\circ\text{C}$ ) is the reference temperature corresponding to the *Vibrio*  
489 *pectenicida* thermal optimum [38], and  $E_a/R$  is the activation energy divided by the  
490 gas constant. The Arrhenius formulation ensures that colder temperatures slow disease

<sup>491</sup> progression (longer E, I<sub>1</sub>, I<sub>2</sub> durations) and reduce shedding rates, consistent with the  
<sup>492</sup> observed latitudinal gradient in SSWD severity.

### <sup>493</sup> 3.3.3 Tolerance: Extending I<sub>2</sub> Duration

<sup>494</sup> The tolerance trait  $t_i$  operates as a damage-limitation mechanism that reduces the effec-  
<sup>495</sup> tive I<sub>2</sub> → D mortality rate, extending survival time while infected:

$$\mu_{I_2 \rightarrow D, \text{eff}} = \mu_{I_2 \rightarrow D}(T) \times (1 - t_i \tau_{\max}), \quad \text{floored at } 0.05 \times \mu_{I_2 \rightarrow D}(T), \quad (14)$$

<sup>496</sup> where  $\tau_{\max} = 0.85$  is the maximum mortality reduction at  $t_i = 1$ . The floor prevents  
<sup>497</sup> biologically implausible indefinite survival. The effective rate is used when sampling the  
<sup>498</sup> I<sub>2</sub> timer (Eq. 2), so tolerant individuals spend longer in I<sub>2</sub>— which may prolong both  
<sup>499</sup> recovery opportunity and pathogen shedding.

### <sup>500</sup> 3.3.4 Recovery

<sup>501</sup> Recovery from infection proceeds via the clearance trait  $c_i$ , which represents the host's  
<sup>502</sup> capacity for pathogen elimination.

<sup>503</sup> **Recovery from I<sub>2</sub>.** Each day, an I<sub>2</sub> individual has probability:

$$p_{\text{rec}, I_2} = \rho_{\text{rec}} \times c_i, \quad \rho_{\text{rec}} = 0.05 \text{ d}^{-1}, \quad (15)$$

<sup>504</sup> of transitioning to the R compartment. At  $c_i = 0$  (no clearance ability), recovery is  
<sup>505</sup> impossible; at  $c_i = 1$ , the daily recovery probability is 5%.

<sup>506</sup> **Early recovery from I<sub>1</sub>.** Individuals with exceptionally high clearance ability ( $c_i >$   
<sup>507</sup> 0.5) can recover during the pre-symptomatic stage:

$$p_{\text{rec}, I_1} = \begin{cases} 0 & \text{if } c_i \leq 0.5, \\ \rho_{\text{rec}} \times 2(c_i - 0.5) & \text{if } c_i > 0.5. \end{cases} \quad (16)$$

<sup>508</sup> At  $c_i = 1.0$ , the early recovery probability equals  $\rho_{\text{rec}}$ , identical to I<sub>2</sub> recovery at maximum  
<sup>509</sup> clearance. The threshold at  $c_i = 0.5$  ensures that only rare, high-clearance individuals  
<sup>510</sup> can clear infection before progressing to the symptomatic stage.

## 511 3.4 Vibrio Dynamics

512 The concentration of waterborne *Vibrio pectenicida* at node  $k$  evolves according to:

$$\frac{dP_k}{dt} = \underbrace{\sigma_1(T) n_{I_1} + \sigma_2(T) n_{I_2} + \sigma_D n_{D,\text{fresh}}}_{\text{shedding}} - \underbrace{\xi(T) P_k}_{\text{decay}} - \underbrace{\phi_k P_k}_{\text{flushing}} + \underbrace{P_{\text{env}}(T, S)}_{\text{reservoir}} + \underbrace{\sum_j d_{jk} P_j}_{\text{dispersal}}, \quad (17)$$

513 integrated via forward Euler with  $\Delta t = 1$  day, subject to  $P_k \geq 0$ .

### 514 3.4.1 Shedding

515 Pathogen shedding from live infectious hosts is temperature-dependent:

$$\sigma_1(T) = 5.0 \times \text{Arr}(T) \quad (\text{I}_1: \text{pre-symptomatic}), \quad (18)$$

$$\sigma_2(T) = 50.0 \times \text{Arr}(T) \quad (\text{I}_2: \text{symptomatic}), \quad (19)$$

516 where  $\text{Arr}(T)$  denotes the Arrhenius factor (Eq. 13) with  $E_a/R = 5,000\text{ K}$ . The 10-  
517 fold difference between early and late shedding reflects the dramatic increase in tissue  
518 degradation and pathogen release during the wasting phase. Rates are given in bacte-  
519 ria  $\text{mL}^{-1} \text{d}^{-1} \text{host}^{-1}$  and represent field-effective values (Errata E2).

### 520 3.4.2 Carcass Shedding

521 Dead individuals ( $D$  compartment) continue to shed pathogen saprophytically for a 3-day  
522 window at a constant rate  $\sigma_D = 15 \text{ bacteria mL}^{-1} \text{d}^{-1} \text{carcass}^{-1}$  (field-effective; Code Er-  
523 rata CE-6). A ring buffer of daily disease death counts over the most recent 3 days tracks  
524 the number of “fresh” carcasses contributing to shedding:

$$n_{D,\text{fresh}}(t) = \sum_{\tau=0}^2 \text{deaths}(t - \tau). \quad (20)$$

### 525 3.4.3 Vibrio Decay

526 *Vibrio pectenicida* survives longer in warmer water. The natural decay rate  $\xi(T)$  is  
527 interpolated log-linearly between empirical estimates:

$$\xi(T) = \begin{cases} 1.0 \text{ d}^{-1} & T \leq 10^\circ\text{C} \text{ (half-life } \approx 0.7 \text{ d}), \\ 0.33 \text{ d}^{-1} & T \geq 20^\circ\text{C} \text{ (half-life } \approx 2.1 \text{ d}), \\ \exp[(1-f) \ln \xi_{10} + f \ln \xi_{20}] & \text{otherwise}, \end{cases} \quad (21)$$

528 where  $f = (T - 10)/10$  and values are clamped outside the  $10\text{--}20^\circ\text{C}$  range. This counter-  
529 intuitive pattern (faster decay at cold temperatures) reflects the environmental Vibrio

530 literature [44].

### 531 3.4.4 Environmental Reservoir

532 In the ubiquitous scenario (default), *Vibrio pectenicida* is assumed to persist in the sed-  
 533 iment as viable-but-non-culturable (VBNC) cells that resuscitate when SST exceeds a  
 534 threshold. The background input rate is:

$$P_{\text{env}}(T, S) = P_{\text{env,max}} \underbrace{\frac{1}{1 + e^{-\kappa_{\text{VBNC}}(T - T_{\text{VBNC}})}}}_{\text{VBNC sigmoid}} \underbrace{g_{\text{peak}}(T)}_{\text{thermal performance}} \underbrace{S_{\text{sal}}}_{\text{salinity}}, \quad (22)$$

535 where:

- 536 •  $P_{\text{env,max}} = 500 \text{ bacteria mL}^{-1} \text{ d}^{-1}$  is the maximum input rate;
- 537 •  $\kappa_{\text{VBNC}} = 1.0 \text{ }^{\circ}\text{C}^{-1}$  controls the steepness of VBNC resuscitation;
- 538 •  $T_{\text{VBNC}} = 12 \text{ }^{\circ}\text{C}$  is the midpoint temperature;
- 539 •  $g_{\text{peak}}(T)$  is a thermal performance curve with Arrhenius increase below  $T_{\text{opt}} = 20 \text{ }^{\circ}\text{C}$   
 540 and quadratic decline above, reaching zero at  $T_{\text{max}} = 30 \text{ }^{\circ}\text{C}$ .

541 In the invasion scenario,  $P_{\text{env}} = 0$  everywhere until the pathogen is explicitly intro-  
 542 duced.

## 543 3.5 Pathogen Evolution

544 When pathogen evolution is enabled, each infectious agent carries a continuous virulence  
 545 phenotype  $v_i$  that modulates disease rates via mechanistic tradeoff functions.

### 546 3.5.1 Virulence–Tradeoff Curves

547 More virulent strains kill faster, shed more, and progress more rapidly, but also remove  
 548 themselves from the host population sooner:

$$\sigma_{1,v}(T) = \sigma_1(T) \times \exp(\alpha_{\text{shed}} \gamma_{\text{early}} (v - v^*)), \quad (23)$$

$$\sigma_{2,v}(T) = \sigma_2(T) \times \exp(\alpha_{\text{shed}} (v - v^*)), \quad (24)$$

$$\mu_{I_1 \rightarrow I_2, v}(T) = \mu_{I_1 \rightarrow I_2}(T) \times \exp(\alpha_{\text{prog}} (v - v^*)), \quad (25)$$

$$\mu_{I_2 \rightarrow D, v}(T) = \mu_{I_2 \rightarrow D}(T) \times \exp(\alpha_{\text{kill}} (v - v^*)), \quad (26)$$

549 where  $v^* = 0.5$  is the ancestral virulence (identity point),  $\alpha_{\text{shed}} = 1.5$ ,  $\alpha_{\text{prog}} = 1.0$ ,  
 550  $\alpha_{\text{kill}} = 2.0$ , and  $\gamma_{\text{early}} = 0.3$  attenuates the shedding effect in the pre-symptomatic stage.

551 **3.5.2 Transmission and Mutation**

552 When a new infection occurs, the infecting strain is inherited either from a shedding  
 553 individual (weighted by shedding rate) or from the environmental reservoir (with virulence  
 554  $v_{\text{env}} = 0.5$ ). The probability of inheriting from a shedder is proportional to the total host-  
 555 derived shedding relative to total pathogen input:

$$P(\text{from shedder}) = \frac{\sum_j \sigma_j(v_j, T)}{\sum_j \sigma_j(v_j, T) + P_{\text{env}}(T, S)}. \quad (27)$$

556 The inherited virulence is then subject to mutation:

$$v_{\text{new}} = \text{clip}(v_{\text{parent}} + \mathcal{N}(0, \sigma_{v,\text{mut}}^2), v_{\text{min}}, v_{\text{max}}), \quad (28)$$

557 with  $\sigma_{v,\text{mut}} = 0.02$ ,  $v_{\text{min}} = 0$ ,  $v_{\text{max}} = 1$ .

558 **3.6 Basic Reproduction Number**

559 The basic reproduction number provides a summary measure of epidemic potential at a  
 560 node:

$$R_0 = \frac{a_{\text{exp}} S_0 (1 - \bar{r}) S_{\text{sal}}}{K_{1/2} (\xi(T) + \phi_k)} \left[ \frac{\sigma_1(T)}{\mu_{I_1 \rightarrow I_2}(T)} + \frac{\sigma_2(T)}{\mu_{I_2 \rightarrow D,\text{eff}}(T) + \rho_{\text{rec}} \bar{c}} + \sigma_D \tau_D \right], \quad (29)$$

561 where  $S_0$  is the number of susceptibles,  $\bar{r}$  and  $\bar{c}$  are population-mean resistance and  
 562 recovery scores,  $\mu_{I_2 \rightarrow D,\text{eff}}$  incorporates population-mean tolerance (Eq. 14),  $\rho_{\text{rec}} \bar{c}$  adds the  
 563 recovery exit rate from  $I_2$ , and  $\tau_D = 3$  days is the carcass shedding duration. The three  
 564 bracketed terms represent the pathogen contribution from each infectious compartment  
 565 ( $I_1$ ,  $I_2$ , and  $D$  carcasses, respectively).

566 **3.7 Daily Update Sequence**

567 Within each daily timestep, the disease module executes the following steps in order:

- 568 1. **Update Vibrio concentration** via Euler integration of Eq. 17, using current  
 569 compartment counts and environmental conditions.
- 570 2. **Transmission ( $S \rightarrow E$ ):** For each susceptible agent, compute the force of infection  
 571  $\lambda_i$  (Eq. 4), convert to daily probability (Eq. 5), and draw a Bernoulli infection event.  
 572 Newly exposed agents receive an Erlang-sampled E-stage timer. When pathogen  
 573 evolution is active, the infecting strain is inherited and mutated (Section 3.5.2).
- 574 3. **Disease progression:** Decrement all disease timers. For agents with expired  
 575 timers:  $E \rightarrow I_1$ ,  $I_1 \rightarrow I_2$  (with tolerance-adjusted timer),  $I_2 \rightarrow D$ . For agents with

active timers: check recovery from  $I_2$  (Eq. 15) and early recovery from  $I_1$  (Eq. 16).

4. **Carcass tracking:** Record today’s disease deaths in the 3-day ring buffer for saprophytic shedding.

5. **Update diagnostics:** Recount compartments, update cumulative statistics (total infections, deaths, recoveries), track peak prevalence and peak Vibrio.

All operations are vectorized using NumPy batch sampling and array-level random draws for computational efficiency, achieving  $O(N)$  scaling in population size.

## 4 Genetics Module

The genetics module tracks a diploid genotype at 51 biallelic loci for every individual, partitioned into three quantitative defense traits: *resistance*, *tolerance*, and *recovery*. Genotypes are transmitted via Mendelian inheritance with free recombination, mutated at a per-allele rate  $\mu = 10^{-8}$  per generation [46], and subject to natural selection through the coupling of trait scores to disease dynamics (Section 3). The module additionally implements sweepstakes reproductive success (SRS) to capture the extreme reproductive variance characteristic of broadcast-spawning marine invertebrates [27].

### 4.1 Three-Trait Architecture

Each individual carries a  $(51 \times 2)$  genotype array of `int8` alleles, where the 51 loci are partitioned into three contiguous blocks:

Table 3: Three-trait genetic architecture. The partition is configurable (constraint:  $n_R + n_T + n_C = 51$ ); the default 17/17/17 split is used in all analyses reported here.

Trait	Symbol	Loci	Indices	Mechanistic role
Resistance	$r_i$	$n_R = 17$	0–16	Immune exclusion: reduces probability of $S \rightarrow E$ transition
Tolerance	$t_i$	$n_T = 17$	17–33	Damage limitation: extends $I_2$ survival via mortality rate reduction
Recovery	$c_i$	$n_C = 17$	34–50	Pathogen clearance: daily probability of $I_1/I_2 \rightarrow R$ transition

These three traits represent biologically distinct immune strategies with different epidemiological consequences [54]:

- **Resistance** ( $r_i$ ) acts *before* infection via receptor polymorphisms, barrier defenses, and innate pathogen recognition. Resistant individuals reduce pathogen pressure on the population by preventing shedding entirely.

- 599     • **Tolerance** ( $t_i$ ) acts *during* infection via tissue repair, anti-inflammatory regulation,  
 600 and metabolic compensation. Tolerant hosts survive longer while infected but con-  
 601 tinue to shed pathogen—they are epidemiological “silent spreaders” that maintain  
 602 transmission pressure while saving themselves.
- 603     • **Recovery** ( $c_i$ ) acts *during late infection* via coelomocyte phagocytosis and immune  
 604 effector mobilization. Recovering hosts actively clear the pathogen and transition  
 605 to an immune state (R), removing a shedding host from the population.

606     The locus count of 51 is motivated by Schiebelhut et al. [58], who identified ~51  
 607 loci under selection in *Pisaster ochraceus* SSWD survivors. No genome-wide association  
 608 study (GWAS) data currently distinguish resistance, tolerance, and recovery loci in *P. he-*  
 609 *lianthesoides*; the equal 17/17/17 partition is a simplifying assumption whose sensitivity is  
 610 explored via the  $n_R$  parameter in the global sensitivity analysis (Section 7). A reference  
 611 genome for *P. helianthoides* is now available [60], enabling future empirical partitioning.

612     **Removal of EF1A overdominant locus.** An earlier model version included a 52nd  
 613 locus representing the EF1A elongation factor with overdominant fitness effects, based  
 614 on Wares and Schiebelhut [68] who documented allele frequency shifts at this locus in  
 615 *Pisaster ochraceus* following SSWD. We removed this locus because (1) the EF1A finding  
 616 is specific to *Pisaster* with no evidence of overdominance in *P. helianthoides*, and (2) a  
 617 single overdominant locus imposed a hard floor on heterozygosity loss that was biologically  
 618 unjustified for our focal species.

## 619     4.2 Trait Score Computation

620     At each locus  $\ell$ , an individual carries two alleles  $g_{\ell,0}, g_{\ell,1} \in \{0, 1\}$ , where 1 denotes the  
 621 derived (protective) allele and 0 the ancestral allele. Each locus within a trait block has  
 622 a fixed effect size  $e_\ell > 0$ , and an individual’s trait score is the effect-weighted mean allele  
 623 dosage:

$$\theta_i = \sum_{\ell \in \mathcal{L}_\theta} e_\ell \frac{g_{\ell,0} + g_{\ell,1}}{2} \quad (30)$$

624     where  $\mathcal{L}_\theta$  denotes the locus set for trait  $\theta \in \{r, t, c\}$  and  $\theta_i \in [0, \sum e_\ell]$ . Effect sizes within  
 625 each trait block are normalized so  $\sum_{\ell \in \mathcal{L}_\theta} e_\ell = 1$ , bounding all trait scores to [0, 1].

### 626     4.2.1 Effect Size Distribution

627     Per-locus effect sizes are drawn from an exponential distribution  $e_\ell \sim \text{Exp}(\lambda = 1)$ , nor-  
 628 malized to sum to 1.0 within each trait, and sorted in descending order. This produces  
 629 a distribution where a few loci have large effects and the remainder have small effects,

630 consistent with empirical QTL architectures for disease resistance traits [41]. A fixed  
 631 seed ensures identical effect sizes across simulation runs. Each trait block receives inde-  
 632 pendently drawn effect sizes.

### 633 4.2.2 Coupling to Disease Dynamics

634 The three traits feed into the disease module (Section 3) as follows:

635 1. **Resistance** reduces the per-individual force of infection:

$$\lambda_i = a \cdot \frac{P}{K_{1/2} + P} \cdot (1 - r_i) \cdot S_{\text{sal}} \cdot f_L(L_i) \quad (31)$$

636 where  $a$  is the exposure rate,  $P$  the local *Vibrio pectenicida* concentration,  $K_{1/2}$   
 637 the half-infective dose,  $S_{\text{sal}}$  the salinity modifier, and  $f_L(L_i)$  the size-dependent  
 638 susceptibility factor.

639 2. **Tolerance** reduces the  $I_2 \rightarrow D$  transition rate via a timer-scaling mechanism:

$$\mu_{I_2D,i}^{\text{eff}} = \mu_{I_2D}(T) \cdot (1 - t_i \cdot \tau_{\max}) \quad (32)$$

640 where  $\tau_{\max} = 0.85$  is the maximum mortality reduction achievable at  $t_i = 1$ . A  
 641 floor of 5% of the baseline rate prevents complete elimination of disease mortality.  
 642 Tolerant individuals survive longer while infected but continue shedding, creating  
 643 a selective conflict between individual and population-level fitness.

644 3. **Recovery** determines the daily clearance probability:

$$p_{\text{rec},i} = \rho_{\text{rec}} \times c_i \quad (33)$$

645 where  $\rho_{\text{rec}} = 0.05 \text{ d}^{-1}$  is the base recovery rate. Recovery from  $I_1$  requires  $c_i > 0.5$   
 646 (early clearance); recovery from  $I_2$  has no threshold. Successful recovery transitions  
 647 the agent to the R (recovered, immune) compartment.

### 648 4.3 Genotype Initialization

649 Initial allele frequencies are drawn independently for each locus from a Beta distribution:

$$q_\ell \sim \text{Beta}(a, b) \quad (\text{default } a = 2, b = 8) \quad (34)$$

650 producing a right-skewed frequency spectrum where most protective alleles are rare  
 651 ( $\mathbb{E}[q] = a/(a + b) = 0.2$ ), consistent with standing variation in immune genes main-  
 652 tained by mutation-selection balance. The raw frequencies are then rescaled per-trait so  
 653 that the expected population-mean trait score equals a configurable target:

Table 4: Default target population-mean trait scores at initialization.

Trait	Target mean	Rationale
Resistance ( $r_i$ )	0.15	Pre-epidemic standing variation
Tolerance ( $t_i$ )	0.10	Moderate damage limitation
Recovery ( $c_i$ )	0.02	Rare standing variation for clearance

654 Recovery is initialized with the lowest mean because active pathogen clearance is assumed  
 655 to be the rarest phenotype prior to epidemic exposure. Per-locus frequencies are clipped  
 656 to  $[0.001, 0.5]$  to prevent fixation at initialization while ensuring the derived allele never  
 657 begins at majority frequency. Genotypes are then sampled assuming Hardy–Weinberg  
 658 equilibrium at each locus: each allele copy is independently drawn as a Bernoulli trial  
 659 with probability  $q_\ell$ .

#### 660 4.4 Mendelian Inheritance and Mutation

661 At reproduction, each offspring inherits one randomly chosen allele from each parent at  
 662 every locus (independent assortment, no linkage). The vectorized implementation draws  
 663 allele choices for all  $n_{\text{offspring}} \times 51 \times 2$  positions simultaneously, then indexes into parental  
 664 genotype arrays.

665 Mutations are applied to offspring genotypes at rate  $\mu = 10^{-8}$  per allele per genera-  
 666 tion [46]. The total number of mutations per cohort is drawn from a Poisson distribution:  
 667  $n_{\text{mut}} \sim \text{Pois}(\mu \times n_{\text{offspring}} \times 51 \times 2)$ . Each mutation flips the allele at a randomly chosen  
 668 position ( $0 \rightarrow 1$  or  $1 \rightarrow 0$ ), providing bidirectional mutational pressure. At the de-  
 669 fault mutation rate, mutations are negligible within the 20–100 year simulation horizon  
 670 (expected  $\sim 10^{-6}$  mutations per offspring), and evolution proceeds primarily through  
 671 selection on standing variation.

#### 672 4.5 Sweepstakes Reproductive Success

673 Broadcast-spawning marine invertebrates exhibit sweepstakes reproductive success (SRS):  
 674 a tiny fraction of adults contribute the majority of surviving offspring in any given cohort  
 675 [27]. This phenomenon produces  $N_e/N$  ratios on the order of  $10^{-3}$  in empirical obser-  
 676 vations [3] and dramatically amplifies genetic drift while simultaneously accelerating the  
 677 fixation of favorable alleles in post-epidemic populations [14].

678 SSWD-EvoEpi implements SRS via a Pareto-weighted reproductive lottery. Each  
 679 spawning adult receives a random weight drawn from a Pareto distribution with shape  
 680 parameter  $\alpha_{\text{SRS}}$  (default 1.35):

$$w_i \sim \text{Pareto}(\alpha_{\text{SRS}}) + 1 \quad (35)$$

681 Female weights are additionally multiplied by size-dependent fecundity (Section 5.5),  
 682 so larger females that win the sweepstakes lottery contribute disproportionately:

$$\tilde{w}_{i,\text{female}} = w_i \times \left( \frac{L_i}{L_{\text{ref}}} \right)^b \quad (36)$$

683 where  $b = 2.5$  is the fecundity allometric exponent and  $L_{\text{ref}} = 500$  mm. Male weights  
 684 use the raw Pareto draw without fecundity modulation. Parents are then sampled with  
 685 replacement from the normalized weight distributions, and offspring receive Mendelian-  
 686 inherited genotypes.

687 The Pareto shape  $\alpha_{\text{SRS}} = 1.35$  was chosen to produce  $N_e/N$  ratios consistent with  
 688 empirical estimates of  $\sim 10^{-3}$  in marine broadcast spawners [3, 27]. A small annual  
 689 variation in  $\alpha$  (drawn from  $\mathcal{N}(\alpha_{\text{SRS}}, \sigma_\alpha^2)$  with  $\sigma_\alpha = 0.10$ ) produces temporal fluctuation  
 690 in the variance of reproductive success across cohorts.

691 **Effective population size.**  $N_e$  is computed from the realized offspring distribution  
 692 using the standard formula [27]:

$$N_e = \frac{4N - 2}{V_k + 2} \quad (37)$$

693 where  $N$  is the number of spawning parents and  $V_k$  is the variance in offspring number.  
 694 Sex-specific  $N_e$  values are computed for females and males separately, then combined via  
 695 harmonic mean:  $N_e = 4N_{e,f}N_{e,m}/(N_{e,f} + N_{e,m})$ .

## 696 4.6 Genetic Diagnostics and Tracking

697 The model records a suite of genetic summary statistics at each node at annual intervals:

698 • **Per-trait means and variances:**  $\bar{r}$ ,  $\bar{t}$ ,  $\bar{c}$  and  $\text{Var}(r)$ ,  $\text{Var}(t)$ ,  $\text{Var}(c)$ .

699 • **Additive genetic variance ( $V_A$ ) per trait:**

$$V_{A,\theta} = \sum_{\ell \in \mathcal{L}_\theta} 2 e_\ell^2 q_\ell (1 - q_\ell) \quad (38)$$

700 where  $q_\ell$  is the derived allele frequency at locus  $\ell$ .  $V_A$  determines the potential rate  
 701 of evolutionary response to selection.

702 • **Heterozygosity:** Observed ( $H_o$ ) and expected ( $H_e$ ) heterozygosity averaged across  
 703 all 51 loci.

704 •  **$F_{ST}$ :** Weir–Cockerham-style  $F_{ST}$  across nodes, computed as  $F_{ST} = \text{Var}(\bar{q})/[\bar{q}(1 - \bar{q})]$   
 705 averaged across polymorphic loci.

- 706 • **Pre- and post-epidemic allele frequency snapshots:** Full 51-locus allele fre-  
707 quency vectors taken immediately before pathogen introduction and two years after  
708 the epidemic onset, enabling direct measurement of allele frequency shifts ( $\Delta q$ ) at-  
709 tributable to selection.

710 **No cost of resistance.** A cost-of-resistance parameter (fecundity penalty for high  $r_i$ )  
711 was considered but excluded following discussion with the senior author. No empirical  
712 evidence supports a measurable fecundity cost for disease resistance alleles in *P. he-*  
713 *lianthesoides*, and including an unparameterized cost would introduce a free parameter  
714 with no calibration target. Fecundity depends solely on body size (Section 5.5).

## 715 4.7 Genotype Bank (Tier 2 Nodes)

716 For Tier 2 spatial nodes that use simplified demographics rather than full agent tracking,  
717 the genetics module maintains a *genotype bank* of  $N_{\text{bank}} = 100$  representative diploid  
718 genotypes with associated frequency weights. The bank is created by random sampling  
719 from the alive population and preserves all three trait scores and allele frequencies. When  
720 agents migrate from a Tier 2 to a Tier 1 node, genotypes are expanded from the bank  
721 using SRS-weighted sampling (Pareto weights  $\times$  bank frequency weights) to reconstruct  
722 individual-level genetic variation.

## 723 5 Population Dynamics

724 The population dynamics module governs the complete life history of *Pycnopodia he-*  
725 *lianthesoides*: growth, natural mortality, reproduction, larval dispersal, and settlement.  
726 All demographic processes operate on a daily timestep, integrated within the master sim-  
727 ulation loop described in Section 2. Disease-driven mortality is handled by the disease  
728 module (Section 3); coupling occurs through shared access to the agent array.

### 729 5.1 Life Stages

730 Each individual progresses through five life stages defined by size thresholds (Table 5).  
731 Stage transitions are unidirectional: agents can only advance, never regress.

Table 5: Life stages and transition thresholds for *P. helianthoides*.

Stage	Size range	Transition at	Duration
Egg/Larva	Planktonic	Settlement event	49–146 days PLD
Settler	0.5–10 mm	$\geq 10$ mm	$\sim 1$ year
Juvenile	10–150 mm	$\geq 150$ mm	$\sim 1\text{--}5$ years
Subadult	150–400 mm	$\geq 400$ mm	$\sim 5\text{--}10$ years
Adult	>400 mm	—	10–50+ years

## 732 5.2 Growth

733 Individual growth follows the von Bertalanffy (VB) growth model in differential form,  
 734 resolved daily:

$$L(t + \Delta t) = L_\infty - (L_\infty - L(t)) \cdot \exp(-k_{\text{growth}} \cdot \Delta t) \quad (39)$$

735 where  $L_\infty = 1000$  mm is the asymptotic arm-tip diameter,  $k_{\text{growth}} = 0.08 \text{ yr}^{-1}$  is the  
 736 Brody growth coefficient, and  $\Delta t = 1/365 \text{ yr}$  for the daily timestep. Individual growth  
 737 variation is introduced through a multiplicative log-normal noise term applied to the daily  
 738 increment:

$$\Delta L_i = (L_{\text{det}} - L_i) \cdot \exp(\varepsilon_i), \quad \varepsilon_i \sim \mathcal{N}\left(0, \frac{\sigma_g}{\sqrt{365}}\right) \quad (40)$$

739 where  $\sigma_g = 2.0$  mm is the annual growth noise scale and the  $\sqrt{365}$  scaling preserves the  
 740 annual CV when integrated over daily steps. Size is constrained to never decrease (no  
 741 shrinking). Stage transitions are evaluated after each growth step based on the thresholds  
 742 in Table 5.

743 Aging proceeds at  $1/365$  years per day, producing fractional ages that drive size-at-age  
 744 trajectories and determine eligibility for senescence mortality.

## 745 5.3 Natural Mortality

746 Natural mortality is resolved daily using continuous hazard rates derived from stage-  
 747 specific annual survival probabilities. The daily death probability for individual  $i$  is:

$$p_{\text{death},i} = 1 - (1 - m_{\text{annual}}(s_i))^{1/365} \quad (41)$$

748 where  $m_{\text{annual}}(s) = 1 - S_{\text{annual}}(s)$  is the annual mortality rate for stage  $s$ . The annual sur-  
 749 vival schedule (Table 6) produces a type III survivorship curve with high settler/juvenile  
 750 mortality and low adult mortality, consistent with demographic estimates for long-lived  
 751 asteroids.

Table 6: Stage-specific annual survival rates.

Stage	Annual survival ( $S$ )	Annual mortality
Settler	0.001	0.999
Juvenile	0.03	0.97
Subadult	0.90	0.10
Adult	0.95	0.05
Senescent	0.98	0.02 (base)

752 **Senescence.** Individuals exceeding the senescence age ( $a_{\text{sen}} = 50$  yr) accumulate addi-  
 753 tional mortality linearly:

$$m_{\text{total}}(s_i, a_i) = m_{\text{annual}}(s_i) + m_{\text{sen}} \cdot \frac{a_i - a_{\text{sen}}}{20} \quad (42)$$

754 where  $m_{\text{sen}} = 0.10$  and the divisor of 20 scales the senescence ramp such that a 70-year-old  
 755 individual experiences an additional 10% annual mortality.

756 Daily mortality is applied via a single vectorized random draw across all alive agents,  
 757 converting stage-dependent annual rates to daily hazard probabilities. This continuous  
 758 approach avoids the artificial synchronization artifacts of annual batch mortality and  
 759 permits realistic within-year population fluctuations.

## 760 5.4 Spawning System

761 SSWD-EvoEpi implements a biologically detailed spawning system reflecting the ex-  
 762 tended reproductive season and cascading spawning behavior observed in *P. helianthoides*.

### 763 5.4.1 Spawning Season and Phenology

764 The spawning season extends from day 305 ( $\approx$ November 1) through day 196 ( $\approx$ July 15)  
 765 of the following year, spanning approximately 270 days and wrapping across the calendar  
 766 year boundary. Spawning intensity follows a Normal envelope centered on a latitude-  
 767 adjusted peak:

$$P_{\text{season}}(d) = \exp\left(-\frac{(\Delta d)^2}{2 \sigma_{\text{peak}}^2}\right) \quad (43)$$

768 where  $\Delta d$  is the shortest circular distance between day  $d$  and the peak day (accounting  
 769 for year wrapping), and  $\sigma_{\text{peak}} = 60$  days is the standard deviation of the seasonal peak.  
 770 The peak day-of-year is latitude-dependent:

$$d_{\text{peak}}(\phi) = d_{\text{peak,base}} + \lceil (\phi - 40^{\circ}\text{N}) \times 3 \text{ d/}^{\circ} \rceil \quad (44)$$

771 where  $d_{\text{peak,base}} = 105$  ( $\approx$ April 15) is the reference peak at  $40^\circ\text{N}$ , and higher-latitude  
772 populations spawn approximately 3 days later per degree northward.

### 773 5.4.2 Spontaneous Spawning

774 Each day during the spawning season, mature adults ( $\geq 400$  mm, Susceptible or Recovered  
775 disease state) are first evaluated for *readiness*, a stochastic physiological state modulated  
776 by the seasonal envelope  $P_{\text{season}}(d)$ . Once ready, individuals attempt spontaneous spawning  
777 with sex-specific daily probabilities:

$$p_{\text{spawn,female}} = 0.012 \quad (45)$$

$$p_{\text{spawn,male}} = 0.0125 \quad (46)$$

778 These rates were calibrated to produce  $\geq 80\%$  female spawning participation per season  
779 and a mean of  $\sim 2.2$  male bouts per season, consistent with the observation that males  
780 spawn more frequently than females in broadcast-spawning asteroids.

781 **Bout limits and refractory periods.** Females are limited to a maximum of 2 spawning  
782 bouts per season; males are limited to 3 bouts. Males enter a brief refractory period  
783 between bouts (default 0 days, configurable) during which they cannot spawn, reflecting  
784 the physiological recovery time for spermatogenesis.

### 785 5.4.3 Cascade Induction

786 Spawning by one individual can trigger spawning in nearby conspecifics via waterborne  
787 chemical cues (spawning-induced spawning), producing the synchronous mass spawning  
788 events observed in broadcast spawners. Induction operates over a 3-day chemical cue  
789 persistence window and is strongly sex-asymmetric:

$$\kappa_{\text{fm}} = 0.80 \quad (\text{female} \rightarrow \text{male induction}) \quad (47)$$

$$\kappa_{\text{mf}} = 0.60 \quad (\text{male} \rightarrow \text{female induction}) \quad (48)$$

790 where  $\kappa_{\text{fm}}$  is the probability that a ready male spawns when a female within the cas-  
791 cade radius (200 m) has spawned within the cue window. The female-to-male asymmetry  
792 reflects the stronger spawning trigger provided by egg-associated chemical signals. Readi-  
793 ness induction also operates: individuals not yet physiologically ready can be driven to  
794 readiness by nearby spawning activity, with a daily probability of 0.5 when within a 300 m  
795 detection radius.

796 **5.4.4 Post-Spawning Immunosuppression**

797 Spawning imposes a 28-day immunosuppression period during which the individual's force  
798 of infection is multiplied by a susceptibility factor of 2.0:

$$\lambda_i^{\text{eff}} = \lambda_i \times \begin{cases} \chi_{\text{immuno}} = 2.0 & \text{if immunosuppression timer} > 0 \\ 1.0 & \text{otherwise} \end{cases} \quad (49)$$

799 This reflects the metabolic cost of gamete production and the documented increase in  
800 disease susceptibility following reproductive investment in marine invertebrates. The  
801 immunosuppression timer is reset each time an individual spawns, so multiple spawning  
802 bouts within a season extend the vulnerability window. Immunosuppression timers are  
803 decremented daily regardless of spawning season status.

804 **5.5 Fecundity**

805 Female fecundity follows an allometric relationship with body size:

$$F_i = F_0 \cdot \left( \frac{L_i}{L_{\text{ref}}} \right)^b \quad (50)$$

806 where  $F_0 = 10^7$  eggs is the reference fecundity at  $L_{\text{ref}} = 500$  mm and  $b = 2.5$  is the  
807 allometric exponent. Only females at or above the minimum reproductive size  $L_{\min} =$   
808 400 mm produce eggs. No cost-of-resistance penalty is applied to fecundity (Section 4.6).

809 **5.6 Fertilization Kinetics and the Allee Effect**

810 Broadcast spawners face a fertilization Allee effect: at low population density, sperm lim-  
811 itation reduces the fraction of eggs successfully fertilized [16, 43]. We model fertilization  
812 success using a mean-field approximation of the Lundquist and Botsford [43] broadcast  
813 fertilization model:

$$\mathcal{F}(\rho_m) = 1 - \exp(-\gamma_{\text{fert}} \cdot \rho_{m,\text{eff}}) \quad (51)$$

814 where  $\gamma_{\text{fert}} = 4.5 \text{ m}^2$  is the sperm contact parameter and  $\rho_{m,\text{eff}}$  is the effective male density,  
815 potentially enhanced by spawning aggregation behavior. The aggregation factor increases  
816 effective local density within spawning clumps above the spatially uniform average when  
817 adult count exceeds a threshold.

818 This produces a quadratic relationship between zygote production and density at low  
819 density:  $\text{zygotes} \propto \rho_f \times \mathcal{F}(\rho_m) \propto \rho^2$  when  $\rho \rightarrow 0$ , creating a strong demographic Allee  
820 effect. For high-fecundity broadcast spawners like *P. helianthoides*, the deterministic  
821 Allee threshold is near zero density; the practical Allee effect operates through stochastic  
822 processes at low  $N$ .

823 **5.7 Larval Phase**

824 Fertilized eggs enter a temperature-dependent pelagic larval duration (PLD):

$$\text{PLD}(T) = \text{PLD}_{\text{ref}} \cdot \exp(-Q_{\text{dev}} \cdot (T - T_{\text{ref}})) \quad (52)$$

825 where  $\text{PLD}_{\text{ref}} = 63$  days at  $T_{\text{ref}} = 10.5^\circ\text{C}$  [35], and  $Q_{\text{dev}} = 0.05 \text{ } ^\circ\text{C}^{-1}$  produces shorter  
826 PLD at warmer temperatures. PLD is clamped to  $[30, 150]$  days.

827 Larval survival during the pelagic phase follows a constant daily mortality model:

$$S_{\text{larval}} = \exp(-\mu_{\text{larva}} \cdot \text{PLD}) \quad (53)$$

828 with  $\mu_{\text{larva}} = 0.05 \text{ d}^{-1}$ . At the reference PLD of 63 days, this yields  $S_{\text{larval}} \approx 4.3\%$  — high  
829 mortality that is compensated by the enormous fecundity of *P. helianthoides*.

830 Larval cohorts carry genotypes inherited via the SRS lottery (Section 4.5) and are  
831 tracked as discrete objects during the pelagic phase. Upon completion of PLD, competent  
832 larvae are available for settlement. In the spatial simulation (Section 6), cohorts are  
833 dispersed between nodes via the larval connectivity matrix  $\mathbf{C}$  before settlement.

834 **5.8 Settlement and Recruitment**

835 Competent larvae settle into the benthic population through a three-stage process:

836 **1. Settlement cue (Allee effect).** Settlement success is modulated by the pres-  
837 ence of conspecific adults via a Michaelis–Menten function representing biofilm-mediated  
838 settlement cues:

$$C_{\text{settle}}(N_{\text{adults}}) = 0.2 + \frac{0.8 \cdot N_{\text{adults}}}{5 + N_{\text{adults}}} \quad (54)$$

839 where the baseline of 0.2 represents settlement on coralline algae in the absence of adults,  
840 and the additional 0.8 reflects enhanced settlement induced by adult biofilm. The half-  
841 saturation constant of 5 adults means that even a small remnant population provides  
842 strong settlement cues.

843 **2. Density-dependent recruitment (Beverton–Holt).** The number of recruits is  
844 governed by a standard Beverton–Holt stock-recruitment relationship:

$$R = \frac{K \cdot s_0 \cdot S}{K + s_0 \cdot S} \quad (55)$$

845 where  $S$  is the number of effective settlers (after cue modulation),  $K$  is the carrying  
846 capacity, and  $s_0 = 0.03$  is the density-independent per-settler survival rate. At low  $S$ ,

847  $R \approx s_0 S$  (supply-limited); at high  $S$ ,  $R \rightarrow K$  (habitat-limited). For broadcast spawners  
848 with  $S \gg K$ , recruitment is typically habitat-limited and population self-regulates.

849 **3. Agent initialization.** Recruited settlers are placed in dead agent slots, assigned  
850 size 0.5 mm, age 0, Settler stage, random sex (1:1 ratio), Susceptible disease state, and  
851 random position within the node’s habitat area. Genotypes are copied from the SRS-  
852 selected settler genotypes, and all three trait scores ( $r_i$ ,  $t_i$ ,  $c_i$ ) are computed from the  
853 inherited genotype.

854 **Juvenile immunity.** Newly settled individuals can optionally be granted a juvenile  
855 immunity period (configurable, default 0 days) during which they are not susceptible  
856 to infection. The settlement day is recorded for each recruit to enable age-dependent  
857 susceptibility calculations.

## 858 5.9 Continuous Settlement

859 Rather than settling all larvae in an annual pulse, the model tracks individual larval  
860 cohorts and settles them daily as their PLD elapses. Cohorts generated by daily spawning  
861 events throughout the extended spawning season (Section 5.4.1) are stored in a per-node  
862 pending list sorted by settlement day. Each simulation day, cohorts whose PLD has  
863 elapsed are popped from the sorted list front (amortized  $O(1)$ ) and passed through the  
864 settlement pipeline. This continuous approach produces realistic seasonal recruitment  
865 pulses that peak several months after the spawning peak, consistent with the observed  
866 temporal offset between spawning and juvenile recruitment in *P. helianthoides*.

867 At the annual boundary, any remaining unsettled cohorts from each node are collected  
868 for spatial dispersal via the connectivity matrix  $\mathbf{C}$  (Section 6), then redistributed to  
869 destination nodes where they continue to settle daily as PLD elapses.

## 870 5.10 Demographic–Genetic–Epidemiological Coupling

871 The population dynamics module is bidirectionally coupled to the disease and genetics  
872 modules:

- 873 • **Disease → demographics:** Disease kills individuals ( $I_2 \rightarrow D$ ), reducing popula-  
874 tion size and altering age/size structure. Post-spawning immunosuppression (Sec-  
875 tion 5.4.4) increases disease risk for recent spawners, creating a temporal alignment  
876 between peak reproductive effort and peak epidemic severity during warm months.
- 877 • **Demographics → disease:** Reduced population density lowers contact rates and  
878 environmental pathogen concentration. The fertilization Allee effect (Section 5.6)

879 amplifies population collapse by reducing reproductive output at low density, po-  
880 tentially trapping populations in an extinction vortex.

- 881 • **Genetics → demographics:** The SRS lottery (Section 4.5) produces extreme  
882 reproductive variance that amplifies genetic drift while accelerating the fixation  
883 of resistance, tolerance, and recovery alleles enriched by selection during epidemic  
884 episodes.
- 885 • **Demographics → genetics:** Population bottlenecks from disease reduce  $N_e$  far  
886 below census  $N$ , compounded by SRS ( $N_e/N \sim 10^{-3}$ ). The interaction of selection  
887 with small effective population size determines whether evolutionary rescue is fast  
888 enough to prevent extinction.

## 889 6 Spatial Module and Environmental Forcing

890 SSWD-EvoEpi represents the NE Pacific range of *Pycnopodia helianthoides* as a metapop-  
891 ulation network of discrete spatial nodes connected by larval dispersal and pathogen  
892 transport. Each node carries its own environmental forcing (sea surface temperature,  
893 salinity, flushing rate) that modulates local disease and demographic dynamics. This sec-  
894 tion describes the spatial architecture, connectivity matrices, environmental time series,  
895 and agent movement model.

### 896 6.1 Metapopulation Network Structure

897 The metapopulation is a graph  $\mathcal{G} = (\mathcal{N}, \mathbf{C}, \mathbf{D})$  where each node  $k \in \mathcal{N}$  represents a geo-  
898 graphically delineated habitat patch and  $\mathbf{C}$ ,  $\mathbf{D}$  are the larval and pathogen connectivity  
899 matrices, respectively.

#### 900 6.1.1 Node Definition

901 Each node is parameterized by a `NodeDefinition` record with the following fields:

Table 7: Node definition fields.

Field	Units	Description
lat, lon	°N, °E	Geographic coordinates
carrying_capacity	individuals	Local $K$ ( $=$ habitat area $\times \rho_{\max}$ )
is_fjord	bool	Fjord vs. open coast classification
sill_depth	m	Sill depth ( $\infty$ for open coast)
flushing_rate	d $^{-1}$	Mean annual hydrodynamic flushing $\phi_k$
mean_sst	°C	Baseline annual mean SST
sst_amplitude	°C	Annual cycle half-range
sst_trend	°C yr $^{-1}$	Linear warming trend
salinity	psu	Effective mean salinity
depth_range	m	Min–max habitat depth
subregion	—	Biogeographic subregion code

902 At runtime, each `NodeDefinition` is wrapped in a `SpatialNode` object that holds the  
 903 local population arrays (agents and genotypes), current environmental state (SST, salin-  
 904 ity, flushing rate), Vibrio concentration, and diagnostic flags. The `MetapopulationNetwork`  
 905 aggregates all nodes together with the **C**, **D**, and distance matrices.

### 906 6.1.2 Internode Distance Computation

907 Connectivity kernels require pairwise waterway distances between nodes. Two methods  
 908 are available:

909 **Haversine with tortuosity.** For small networks ( $\leq 11$  nodes), geodesic great-circle  
 910 distances are computed via the Haversine formula and multiplied by a uniform tortuosity  
 911 factor  $\tau = 1.5$  (intermediate between open-coast  $\sim 1.2$  and fjord  $\sim 2.5$ ) to approximate  
 912 along-coast path lengths:

$$d_{jk}^{\text{water}} = \tau \times d_{jk}^{\text{Haversine}}. \quad (56)$$

913 **Precomputed overwater distances.** For full-range simulations, a 489-site overwater  
 914 distance matrix was computed from GEBCO 2022 bathymetric data at 15 arc-second res-  
 915 olution. Land cells were rasterized from Natural Earth 10 m land polygons, and Dijkstra's  
 916 algorithm on a 4-connected ocean grid yielded shortest overwater paths. The resulting  
 917 489  $\times$  489 matrix spans 2.0–7,187 km, with 98.4% of pairs connected (1,946 disconnected  
 918 pairs involve western Aleutian sites near the antimeridian). Model nodes are matched  
 919 to the nearest precomputed site within a 50 km tolerance; unmatched nodes fall back to  
 920 Haversine  $\times \tau$ .

## 921 6.2 Connectivity Matrices

922 Two connectivity matrices govern inter-node exchange:  $\mathbf{C}$  for annual larval dispersal and  
 923  $\mathbf{D}$  for daily pathogen transport (Errata E5). Both use exponential distance kernels but  
 924 operate at different spatial and temporal scales.

### 925 6.2.1 Larval Connectivity Matrix $\mathbf{C}$

926  $C_{jk}$  gives the probability that a competent larva produced at node  $j$  settles at node  $k$ . The  
 927 matrix is constructed from an exponential dispersal kernel with explicit self-recruitment:

$$C_{jk} = \begin{cases} \alpha_j & \text{if } j = k, \\ (1 - \alpha_j) \exp\left(-\frac{d_{jk}}{D_L}\right) b_{jk} & \text{if } j \neq k, \end{cases} \quad (57)$$

928 where:

- 929 •  $D_L = 400$  km is the larval dispersal length scale, reflecting the 4–8 week pelagic  
 930 larval duration (PLD) of *Pycnopodia helianthoides* [63];
- 931 •  $\alpha_j$  is the self-recruitment fraction:  $\alpha_{\text{fjord}} = 0.30$  for fjord nodes (reflecting enhanced  
 932 retention behind sills) and  $\alpha_{\text{open}} = 0.10$  for open-coast nodes;
- 933 •  $b_{jk} \in [0, 1]$  is an optional barrier attenuation factor for biogeographic breaks (e.g.,  
 934 Cape Mendocino).

935 Rows are then normalized so that:

$$\sum_k C_{jk} = r_{\text{total}} = 0.02, \quad (58)$$

936 where  $r_{\text{total}}$  represents the total per-larva settlement success probability, accounting for  
 937 the compounding losses of pelagic mortality, failed metamorphosis, and post-settlement  
 938 predation.

939 The elevated self-recruitment fraction for fjord nodes ( $\alpha_{\text{fjord}} = 3\alpha_{\text{open}}$ ) encodes the em-  
 940 pirical observation that fjords act as larval retention zones [65]: sill-mediated circulation  
 941 traps larvae near their natal site, reducing export to the open coast.

### 942 6.2.2 Pathogen Dispersal Matrix $\mathbf{D}$

943  $D_{jk}$  gives the fraction of waterborne *Vibrio pectenicida* at node  $j$  that reaches node  $k$  per  
 944 day. Pathogen dispersal operates at much shorter range than larval dispersal:

$$D_{jk} = \phi_j f_{\text{out}} \exp\left(-\frac{d_{jk}}{D_P}\right) S_{jk} \quad \text{for } d_{jk} \leq 50 \text{ km}, \quad (59)$$

945 where:

- 946 •  $D_P = 15$  km is the pathogen dispersal scale (reflecting tidal-current transport);  
947 •  $\phi_j$  is the source node's flushing rate ( $d^{-1}$ );  
948 •  $f_{\text{out}} = 0.2$  is the fraction of flushed water reaching neighboring sites;  
949 •  $S_{jk}$  is the sill attenuation factor.

950 Pairs beyond  $d_{jk} > 50$  km receive zero pathogen transfer. Total export from any node  
951 is capped at its flushing rate:  $\sum_k D_{jk} \leq \phi_j$ .

952 **Sill attenuation.** Fjord sills impede pathogen exchange between basins. The attenu-  
953 ation factor is computed from the minimum sill depth across the pair:

$$S_{jk} = \min \left( 1, \left[ \frac{\min(z_j^{\text{sill}}, z_k^{\text{sill}})}{\max(z_j^{\text{max}}, z_k^{\text{max}})} \right]^2 \right), \quad (60)$$

954 where  $z^{\text{sill}}$  is sill depth and  $z^{\text{max}}$  is maximum habitat depth. For open-coast nodes ( $z^{\text{sill}} =$   
955  $\infty$ ),  $S_{jk} = 1$  (no attenuation). For Howe Sound (sill = 30 m, max depth = 100 m),  
956  $S \approx 0.09$ , reducing pathogen exchange by  $\sim 91\%$ .

### 957 6.2.3 Dispersal Dynamics

958 **Pathogen dispersal (daily).** At each timestep, the dispersal input to node  $k$  is:

$$\Delta P_k^{\text{dispersal}} = \sum_j D_{jk} P_j = (\mathbf{D}^\top \mathbf{P})_k, \quad (61)$$

959 which enters the Vibrio ODE (Eq. 17) as an additive source term.

960 **Larval dispersal (annual).** At the end of each reproductive season, competent larvae  
961 from each source node are distributed to receiving nodes via  $\mathbf{C}$ . For source node  $j$   
962 producing  $n_j$  competent larvae: (i) a binomial draw  $n_{\text{settle}} \sim \text{Bin}(n_j, \sum_k C_{jk})$  determines  
963 total settlement; (ii) a multinomial draw allocates settlers across destinations proportional  
964 to the conditional probabilities  $C_{jk} / \sum_k C_{jk}$ ; (iii) settler genotypes are sampled with  
965 replacement from the source pool.

## 966 6.3 Environmental Forcing

967 Each node receives a locally parameterized environmental forcing that drives disease  
968 and demographic rates through temperature-dependent, salinity-dependent, and flushing-  
969 dependent mechanisms.

970 **6.3.1 Sea Surface Temperature**

971 Daily SST at node  $k$  follows a sinusoidal annual cycle with a linear warming trend and  
 972 optional stochastic perturbation:

$$T_k(d, y) = \underbrace{\bar{T}_k + \gamma_k(y - y_{\text{ref}})}_{\text{trend-adjusted mean}} + \underbrace{A_k \cos\left(\frac{2\pi(d - d_{\text{peak}})}{365}\right)}_{\text{annual cycle}}, \quad (62)$$

973 where:

- 974 •  $\bar{T}_k$  is the baseline annual mean SST ( $^{\circ}\text{C}$ ) at reference year  $y_{\text{ref}} = 2000$ ;
- 975 •  $A_k$  is the annual cycle half-range ( $^{\circ}\text{C}$ );
- 976 •  $\gamma_k$  is the linear warming rate ( $^{\circ}\text{C yr}^{-1}$ ; default 0.02);
- 977 •  $d_{\text{peak}} = 227$  (day of year  $\approx$  August 15) corresponds to the late-summer SST maxi-  
 978 mum characteristic of the NE Pacific.

979 The warming trend shifts the SST climatology upward over time, increasing both  
 980 baseline Vibrio viability and the duration of the high-risk summer window. For the 5-  
 981 node validation network,  $\bar{T}_k$  ranges from  $8.0^{\circ}\text{C}$  (Sitka) to  $14.0^{\circ}\text{C}$  (Monterey), producing  
 982 a  $\sim 6^{\circ}\text{C}$  latitudinal gradient consistent with satellite SST climatologies.

983 SST time series are precomputed at initialization via `make_sst_timeseries` and  
 984 stored as dense 1-D arrays of shape  $(n_{\text{years}} \times 365)$  for efficient daily lookup.

985 **6.3.2 Temperature-Dependent Rate Scaling**

986 All temperature-dependent biological rates—disease progression, pathogen shedding, Vib-  
 987 rio decay—are scaled via the Arrhenius function:

$$k(T) = k_{\text{ref}} \exp\left[\frac{E_a}{R} \left(\frac{1}{T_{\text{ref}}} - \frac{1}{T}\right)\right], \quad (63)$$

988 with  $T_{\text{ref}} = 293.15\text{ K}$  ( $20^{\circ}\text{C}$ ), the thermal optimum of *Vibrio pectenicida* [38]. This  
 989 formulation ensures that the latitudinal SST gradient (Eq. 62) produces emergent north–  
 990 south gradients in disease severity, matching the observed pattern of southward-increasing  
 991 SSWD mortality during the 2013–2015 outbreak [25, 51].

992 **6.3.3 Salinity Modifier**

993 Vibrio viability is suppressed at low salinities via a quadratic ramp (Eq. 7), reproduced  
 994 here for completeness:

$$S_{\text{sal}} = \text{clip}\left(\left[\frac{S_k - S_{\text{min}}}{S_{\text{full}} - S_{\text{min}}}\right]^2, 0, 1\right), \quad S_{\text{min}} = 10 \text{ psu}, \quad S_{\text{full}} = 28 \text{ psu}. \quad (64)$$

995 Fjord nodes receive lower salinities (e.g., Howe Sound  $S = 22$  psu due to freshwater  
 996 runoff), yielding  $S_{\text{sal}} = 0.44$  and reducing effective Vibrio viability by  $\sim 56\%$  compared  
 997 to open-coast nodes ( $S \geq 30$  psu,  $S_{\text{sal}} \geq 0.87$ ). This mechanism provides a partial  
 998 explanation for fjord refugia observations [51].

999 **6.3.4 Flushing Rate**

1000 Hydrodynamic flushing removes waterborne pathogen at rate  $\phi_k$  ( $\text{d}^{-1}$ ), entering the Vibrio  
 1001 ODE as the term  $-\phi_k P_k$  (Eq. 17). Node-specific values span two orders of magnitude:

- 1002 • Open coast:  $\phi_k = 0.5\text{--}1.0 \text{ d}^{-1}$  (strong tidal and current flushing);
- 1003 • Semi-enclosed bays:  $\phi_k = 0.3 \text{ d}^{-1}$  (San Juan Islands);
- 1004 • Fjords:  $\phi_k = 0.007\text{--}0.05 \text{ d}^{-1}$  (Errata E3; sill restricts water exchange). Howe Sound  
 1005 is assigned  $\phi_k = 0.03 \text{ d}^{-1}$ .

1006 Low flushing in fjords acts as a double-edged mechanism: it reduces the rate of  
 1007 pathogen removal (potentially increasing local Vibrio concentrations) but also reduces  
 1008 pathogen *export* to neighboring nodes via  $\mathbf{D}$  (Eq. 59), effectively isolating the fjord from  
 1009 regional epidemic dynamics.

1010 Flushing rates are optionally modulated seasonally:

$$\phi_k(m) = \bar{\phi}_k \left[ 1 + A_\phi \cos\left(\frac{2\pi(m-5)}{12}\right) \right], \quad (65)$$

1011 where  $m$  is the 0-indexed month,  $A_\phi = 0.3$  for fjord nodes and  $A_\phi = 0.2$  for open  
 1012 coast, with peak flushing in June ( $m = 5$ ) corresponding to freshwater-driven estuarine  
 1013 circulation maxima.

1014 **6.4 Agent Movement**

1015 Within each node, agents move via a correlated random walk (CRW) that produces  
1016 realistic small-scale spatial structure:

$$\theta(t + \Delta t) = \theta(t) + \mathcal{N}(0, \sigma_\theta^2), \quad (66)$$

$$x(t + \Delta t) = x(t) + v_i \cos \theta \Delta t, \quad (67)$$

$$y(t + \Delta t) = y(t) + v_i \sin \theta \Delta t, \quad (68)$$

1017 where  $\sigma_\theta = 0.6$  rad is the turning-angle standard deviation,  $v_i = v_{\text{base}} \times m_{\text{state}}$  is the  
1018 disease-modified speed, and  $\Delta t = 60$  min (hourly substeps, 24 per day). The base speed  
1019  $v_{\text{base}} = 0.5 \text{ m min}^{-1}$  is consistent with undisturbed *Pycnopodia helianthoides* locomotion  
1020 rates [37]. Disease state modifies speed:  $m_S = m_E = 1.0$  (healthy),  $m_{I_1} = 0.5$  (mild  
1021 impairment),  $m_{I_2} = 0.1$  (severe wasting),  $m_D = 0.0$  (stationary carcass),  $m_R = 1.0$   
1022 (recovered).

1023 Agents are confined to a square habitat of side length  $\sqrt{\text{habitat\_area}}$  with elastic  
1024 boundary reflection.

1025 **Spatial transmission.** When spatial transmission is enabled, each node's habitat is  
1026 discretized into a grid with cell size  $\Delta x = 20$  m. Infected agents deposit pathogen expo-  
1027 sure proportional to their shedding rate into their grid cell, and two Gaussian diffusion  
1028 passes ( $3 \times 3$  averaging) smooth the resulting density field. Susceptible agents then experi-  
1029 ence locally elevated or reduced force of infection depending on their proximity to infected  
1030 individuals, creating emergent disease clustering without modifying the node-level Vibrio  
1031 ODE.

1032 **Sensitivity analysis substeps.** The full 24 hourly substeps per day incur  $\sim 20 \times$  com-  
1033 putational overhead. For sensitivity analysis runs (Section ??), movement is reduced to  
1034 1 substep per day, which captures spatial mixing and aggregation effects at acceptable  
1035 cost.

1036 **6.5 Network Configurations**

1037 Three network configurations are used across model development, validation, and sensi-  
1038 tivity analysis.

1039 **6.5.1 5-Node Validation Network**

1040 The primary validation network spans the NE Pacific range with five nodes selected to  
1041 represent key biogeographic contexts (Table 8):

Table 8: 5-node validation network configuration. SST parameters are baseline values at reference year 2000.

<b>Node</b>	<b>Lat</b>	<b>Lon</b>	$\bar{T}$ (°C)	$A$ (°C)	$S$ (psu)	$\phi$ ( $d^{-1}$ )
Sitka, AK	57.06	-135.34	8.0	3.5	32.0	0.80
Howe Sound, BC	49.52	-123.25	10.0	4.0	22.0	0.03
San Juan Is, WA	48.53	-123.02	10.0	4.0	30.0	0.30
Newport, OR	44.63	-124.05	12.0	3.0	33.0	1.00
Monterey, CA	36.62	-121.90	14.0	2.5	33.5	0.80

1042 Howe Sound is the sole fjord node (sill depth = 30 m,  $\alpha_{self} = 0.30$ ); all others are open  
 1043 coast ( $\alpha_{self} = 0.10$ ). Node carrying capacities range from 400 (Howe Sound) to 1,000  
 1044 (Sitka). This network reproduces three key empirical patterns: the north–south SSWD  
 1045 mortality gradient, fjord protection, and the absence of recovery in southern populations  
 1046 (Section 8).

#### 1047 6.5.2 11-Node Sensitivity Analysis Network

1048 Sensitivity analysis Rounds 1–3 used a minimal 3-node network (Sitka, Howe Sound,  
 1049 Monterey) with inter-node distances of 1,700+ km—far exceeding the larval dispersal  
 1050 scale  $D_L = 400$  km. Consequently, the spatial connectivity parameters ( $D_L$ ,  $\alpha_{self}$ ) were  
 1051 effectively untestable, as the exponential kernel  $\exp(-1700/400) < 10^{-2}$  produced negli-  
 1052 gible inter-node exchange regardless of  $D_L$  values within the SA range.

1053 Round 4 introduced an 11-node stepping-stone chain with six additional intermediate  
 1054 nodes (Table 9), reducing maximum inter-node spacing to  $\sim 452$  km and ensuring that  
 1055  $D_L$  values within the SA range [100, 1,000] km produce meaningful variation in larval ex-  
 1056 change (32–76% at adjacent-node distances of 110–452 km with the default  $D_L = 400$  km).

Table 9: 11-node stepping-stone network for sensitivity analysis Round 4. All nodes have  $K = 5,000$  ( $\sim 55,000$  total agents). SST trend =  $0.02^{\circ}\text{C yr}^{-1}$  for all nodes.

<b>Node</b>	<b>Lat</b>	<b>Lon</b>	$\bar{T}$ ( $^{\circ}\text{C}$ )	$A$ ( $^{\circ}\text{C}$ )	$S$ (psu)	$\phi$ ( $\text{d}^{-1}$ )
Sitka	57.06	-135.34	8.0	3.5	32.0	0.80
Ketchikan	55.34	-131.64	8.5	3.5	31.0	0.50
Haida Gwaii	53.25	-132.07	9.0	3.0	31.5	0.60
Bella Bella	52.16	-128.15	9.5	3.5	28.0	0.40
Howe Sound*	49.52	-123.25	10.0	4.0	22.0	0.03
SJI	48.53	-123.02	10.5	4.0	30.0	0.30
Westport	46.89	-124.10	11.0	3.5	32.0	0.50
Newport	44.63	-124.05	11.5	3.0	33.0	0.60
Crescent City	41.76	-124.20	12.0	2.5	33.0	0.50
Fort Bragg	39.45	-123.80	12.5	2.5	33.5	0.50
Monterey	36.62	-121.90	13.0	2.5	33.5	0.40

\*Fjord node (sill depth = 30 m,  $\alpha_{\text{self}} = 0.30$ ). All other nodes open coast ( $\alpha_{\text{self}} = 0.10$ ).

1057 This upgrade substantially altered parameter importance rankings:  $n_{\text{resistance}}$  rose from  
 1058 rank 19 to rank 5 (the three-trait partition amplifies genetic architecture importance at  
 1059 finer spatial scales), and  $P_{\text{env},\text{max}}$  rose from rank 11 to rank 4 (the environmental reservoir  
 1060 becomes critical with more nodes seeding independent epidemics). See Section ?? for full  
 1061 results.

### 1062 6.5.3 Full-Range Network (Planned)

1063 Scaling analysis (Section 8) demonstrated that the model supports 150-node networks at  
 1064  $\sim 66$  s per 20-year run, enabling a full NE Pacific coastline simulation (Alaska to Baja  
 1065 California). This configuration will use the precomputed 489-site overwater distance  
 1066 matrix (Section 6.1.2) and site-specific SST forcing from satellite climatologies.

## 1067 6.6 Network Construction

1068 The `build_network` function assembles the metapopulation from a list of node definitions  
 1069 by: (i) computing the pairwise distance matrix (Haversine  $\times \tau$  or precomputed overwater  
 1070 distances); (ii) constructing **C** with per-node  $\alpha_j$  values ( $\alpha_{\text{fjord}}$  or  $\alpha_{\text{open}}$ ), the  $D_L$  kernel,  
 1071 optional barrier factors, and row normalization to  $r_{\text{total}}$ ; (iii) constructing **D** with the  $D_P$   
 1072 kernel, flushing-rate modulation, sill attenuation, and the 50 km cutoff; and (iv) wrapping  
 1073 each node definition in a **SpatialNode** with initialized environmental state. The function  
 1074 accepts optional parameters for all kernel scales, self-recruitment fractions, and barrier  
 1075 configurations, allowing the same codebase to serve validation, sensitivity analysis, and  
 1076 full-range simulation.

## 1077 7 Sensitivity Analysis

1078 The SSWD-EvoEpi model contains 47 uncertain parameters spanning six modules: dis-  
1079 ease transmission and progression (16 parameters), genetics and trait architecture (8),  
1080 population dynamics (7), spawning biology (7), pathogen virulence evolution (6), and  
1081 spatial connectivity (3). Most of these parameters have limited empirical constraints  
1082 (Section A), necessitating a systematic sensitivity analysis (SA) to identify which param-  
1083 eters most influence model behavior and, critically, which parameter *interactions* domi-  
1084 nate the system’s dynamics. We conducted a progressive, four-round SA campaign that  
1085 tracked the model’s growing complexity from a single-trait, 3-node prototype through to  
1086 the full three-trait, 11-node eco-evolutionary framework.

### 1087 7.1 Methods

#### 1088 7.1.1 Morris Elementary Effects Screening

1089 Each SA round began with Morris elementary effects screening [52], implemented via the  
1090 SALib Python library [28]. The Morris method is a one-at-a-time (OAT) design in which  
1091 each parameter is perturbed along  $r$  independent trajectories through the  $p$ -dimensional  
1092 input space. For parameter  $x_i$  in trajectory  $j$ , the elementary effect is

$$d_{ij} = \frac{f(x_1, \dots, x_i + \Delta_i, \dots, x_p) - f(x_1, \dots, x_i, \dots, x_p)}{\Delta_i}, \quad (69)$$

1093 where  $\Delta_i$  is the perturbation step. From these we compute two summary statistics per  
1094 parameter per metric [8]:

- 1095 •  $\mu_i^*$ : the mean of the *absolute* elementary effects, measuring overall parameter im-  
1096 portance regardless of sign;
- 1097 •  $\sigma_i$ : the standard deviation of elementary effects, measuring interaction and nonlin-  
1098 earity strength.

1099 When  $\sigma_i/\mu_i^* > 1$ , the parameter’s influence on the metric is dominated by interactions  
1100 with other parameters rather than by its direct (additive) effect [57]. To enable cross-  
1101 metric comparison, we normalize  $\mu^*$  by the range of the metric across all trajectories,  
1102 then rank parameters by the mean normalized  $\mu^*$  across all output metrics.

1103 All rounds used  $r = 20$  trajectories, yielding  $r \times (p + 1)$  total model evaluations per  
1104 round (e.g.,  $20 \times 48 = 960$  runs for the 47-parameter Round 4).

#### 1105 7.1.2 Sobol Variance Decomposition

1106 Parameters surviving Morris screening advance to Sobol variance-based global sensitivity  
1107 analysis [62], which decomposes the total output variance into contributions from individ-

1108 ual parameters and their interactions. Using the Saltelli sampling scheme [56],  $N(2p + 2)$   
1109 model evaluations produce two key indices for each parameter  $x_i$  and output metric  $Y$ :

- 1110 •  $S_{1,i} = V_{x_i}[E_{x \sim i}(Y|x_i)] / V(Y)$ : the *first-order* Sobol index, measuring the fraction  
1111 of output variance attributable to  $x_i$  alone;
- 1112 •  $S_{T,i} = 1 - V_{x \sim i}[E_{x_i}(Y|x \sim i)] / V(Y)$ : the *total-order* index, capturing  $x_i$ 's contribu-  
1113 tion including all interactions with other parameters.

1114 The gap  $S_{T,i} - S_{1,i}$  quantifies the strength of parameter interactions. When  $S_{T,i} \gg S_{1,i}$ , the  
1115 parameter's influence is mediated primarily through joint effects with other parameters,  
1116 implying that it cannot be calibrated independently.

### 1117 7.1.3 Output Metrics

1118 The SA tracks 23 output metrics capturing demographic, evolutionary, spatial, and  
1119 pathogen outcomes over 20-year simulations:

- 1120 • **Demographic:** population crash percentage, final population fraction, recovery  
1121 (population returns to >50% of initial), extinction (metapopulation collapse), peak  
1122 single-year mortality, time to population nadir, total disease deaths, disease death  
1123 fraction;
- 1124 • **Evolutionary (host):** mean and maximum resistance shift ( $\Delta\bar{r}$ ), tolerance shift  
1125 ( $\Delta\bar{t}$ ), recovery-trait shift ( $\Delta\bar{c}$ ), additive variance retention ( $V_A^{\text{post}}/V_A^{\text{pre}}$ ), evolution-  
1126 ary rescue index (composite of survival and resistance gain), total recovery events,  
1127 recovery rate;
- 1128 • **Spatial:** number of extinct nodes, north–south mortality gradient, fjord protection  
1129 effect;
- 1130 • **Pathogen:** mean final virulence, virulence shift ( $\Delta\bar{v}$ );
- 1131 • **Spawning:** spawning participation rate, mean recruitment rate.

## 1132 7.2 Progressive Sensitivity Analysis Design

1133 The SA was conducted in four rounds (Table 10), each corresponding to a major model  
1134 extension. This progressive design allows us to track how parameter importance shifts as  
1135 model complexity grows—a critical diagnostic for identifying emergent behaviors intro-  
1136 duced by new modules.

Table 10: Summary of sensitivity analysis rounds. Each round incorporates all changes from prior rounds. “New” parameters are those added relative to the previous round.

Round	Params	Metrics	Nodes	Runs	Key Changes
R1 (Morris)	23	14	3	480	Baseline: single resistance trait
R2 (Sobol)	23	14	3	12,288	Sobol decomposition of R1 params
R3 (Morris)	43	20	3	880	+20 params: pathogen evo, spawning, continuous mortality, daily growth
R4 (Morris)	47	23	11	960	+4 params: three-trait genetics, 11-node stepping-stone network

1137 **Rounds 1–2 (Pre-Three-Trait Baseline).** The initial SA (Rounds 1–2) examined  
1138 23 parameters across disease (13), population (7), genetics (1:  $n_{\text{additive}}$ ), and spawning  
1139 (2) modules using a 3-node spatial network (Sitka, Howe Sound, Monterey;  $K = 5,000$   
1140 per node). The model at this stage tracked a single resistance trait with  $n_{\text{additive}}$  additive  
1141 loci. Morris screening (480 runs) retained all 23 parameters for Sobol analysis (12,288  
1142 runs,  $N = 256$ ).

1143 The Sobol decomposition revealed that disease progression rate  $\mu_{I2D,\text{ref}}$  ( $I_2 \rightarrow \text{Death}$ )  
1144 was the single most influential parameter (mean  $S_T = 0.638$ ), followed by susceptibility\\_multiplier  
1145 ( $S_T = 0.540$ ) and  $a_{\text{exposure}}$  ( $S_T = 0.473$ ). A critical methodological finding was that Mor-  
1146 ris and Sobol rankings *disagreed*: Morris identified `settler_survival` and  $\rho_{\text{rec}}$  as the  
1147 top drivers of population outcomes, while Sobol elevated susceptibility\\_multiplier and  
1148  $\mu_{I2D,\text{ref}}$ . This discrepancy arises because Morris measures marginal effects from extreme-  
1149 value perturbations, whereas Sobol captures variance-weighted contributions including  
1150 interactions. This confirmed that Morris screening alone is insufficient for identifying  
1151 calibration priorities in this model.

1152 **Round 3 (Expanded Model, 3-Node).** Round 3 added 20 parameters from four  
1153 newly implemented modules: pathogen virulence evolution (6 parameters: virulence–  
1154 fitness tradeoff exponents, mutation rate, initial virulence), expanded spawning biology  
1155 (4: male spontaneous spawning, readiness induction, female bout limits, peak width), and  
1156 additional disease mechanics (immunosuppression duration, minimum susceptible age,  
1157  $I_1 \rightarrow I_2$  progression rate) and genetics parameters (target\\_mean\\_r, Beta-distribution  
1158 shape parameters for initial allele frequencies). The network remained at 3 nodes for  
1159 comparability with R1–R2.

1160 Morris screening (880 runs, 20 trajectories) revealed a dramatic reshuffling:  $\rho_{\text{rec}}$  (re-  
1161 covery rate) rose to #1 ( $\mu_{\text{norm}}^* = 0.642$ ), displacing  $\mu_{I2D,\text{ref}}$  from its R1–R2 dominance.  
1162 This occurred because the transition from discrete-stage to continuous daily mortality  
1163 diluted the  $I_2 \rightarrow \text{Death}$  rate’s marginal influence, while recovery rate’s role was amplified  
1164 by its interaction with the new pathogen evolution module (higher  $\rho_{\text{rec}}$  imposes stronger  
1165 selection against virulent strains). All 43 parameters exceeded the 5% elimination thresh-

1166 old; zero were pruned.

1167 **Round 4 (Full Model, 11-Node).** Round 4 represents the complete SSWD-EvoEpi  
1168 model with two additions: (1) the three-trait genetic architecture (resistance, tolerance,  
1169 recovery; Section 4.1), contributing four new parameters (`target_mean_c`, `target_mean_t`,  
1170  $\tau_{\max}$ ,  $n_{tolerance}$ ); and (2) an 11-node stepping-stone network spanning the latitudinal range  
1171 of *Pycnopodia helianthoides* habitat. The expanded spatial network was critical for re-  
1172 solving spatial parameters that were undetectable at 3 nodes. This round (960 runs, 48  
1173 cores on an Intel Xeon W-3365) provides the most comprehensive screening of the model  
1174 to date.

## 1175 7.3 Round 4 Morris Results

### 1176 7.3.1 Global Parameter Ranking

1177 Table 12 presents the complete Round 4 Morris ranking for all 47 parameters, sorted by  
1178 mean normalized  $\mu^*$  across 23 output metrics. Figure 1 shows the top 20 parameters  
1179 color-coded by module.

1180 The top-10 parameters span four of six modules:

- 1181 1.  $\rho_{\text{rec}}$  (recovery rate;  $\mu_{\text{norm}}^* = 0.889$ ) — the rate at which infected individuals clear  
1182 pathogen remains the single most influential parameter, as in R3. Its semi-additive  
1183 behavior ( $\sigma/\mu^* = 1.46$ , the lowest interaction ratio of any parameter) reflects its  
1184 direct mechanistic role: daily clearance probability  $p_{\text{rec}} = \rho_{\text{rec}} \times c_i$  scales linearly  
1185 with this rate regardless of other parameter values.
- 1186 2.  $k_{\text{growth}}$  (von Bertalanffy growth rate;  $\mu_{\text{norm}}^* = 0.633$ ) — faster growth accelerates  
1187 maturation and spawning eligibility, providing demographic compensation during  
1188 epidemics. Rose from #5 (R3) to #2.
- 1189 3.  $K_{\text{half}}$  (half-infective dose;  $\mu_{\text{norm}}^* = 0.622$ ) — the Michaelis–Menten saturation pa-  
1190 rameter controlling infection probability. Rose from #8 to #3.
- 1191 4.  $P_{\text{env,max}}$  (environmental reservoir;  $\mu_{\text{norm}}^* = 0.598$ ) — background waterborne *V. pecteni-*  
1192 *cida* input, independent of host shedding. Rose dramatically from #11 to #4,  
1193 reflecting its interaction with the 11-node spatial network where environmental  
1194 pathogen load varies with latitude and temperature.
- 1195 5.  $n_{\text{resistance}}$  (number of resistance loci;  $\mu_{\text{norm}}^* = 0.525$ ) — genetic architecture of re-  
1196 sistance. The largest rank gain of any parameter: #19 → #5 ( $\Delta = +14$ ). The  
1197 three-trait partition (17 loci per trait vs. the former 51 total) amplifies the sensi-  
1198 tivity to how many loci underlie each defense mechanism.

- 1199    6.  $s_0$  (settler survival;  $\mu_{\text{norm}}^* = 0.509$ ) — Beverton–Holt baseline recruitment. Dropped  
 1200    modestly from #3 to #6.
- 1201    7.  $\sigma_{2,\text{eff}}$  (late-stage shedding rate;  $\mu_{\text{norm}}^* = 0.431$ ).
- 1202    8.  $\mu_{I2D,\text{ref}}$  ( $I_2 \rightarrow$  Death rate;  $\mu_{\text{norm}}^* = 0.419$ ) — formerly the #1 parameter in R1–R2  
 1203    Sobol ( $S_T = 0.638$ ), now #8 in R4 Morris.
- 1204    9.  $\sigma_{\text{spawn}}$  (spawning peak width;  $\mu_{\text{norm}}^* = 0.392$ ) — controls synchrony of the repro-  
 1205    ductive pulse; dropped from #2 to #9.
- 1206    10. target\_mean\_c (initial mean recovery trait;  $\mu_{\text{norm}}^* = 0.385$ ) — a *new* R4 parame-  
 1207    ter entering directly at #10, confirming that the recovery trait ( $c_i$ ) is the fastest-  
 1208    evolving defense in the model (Section 4.1).

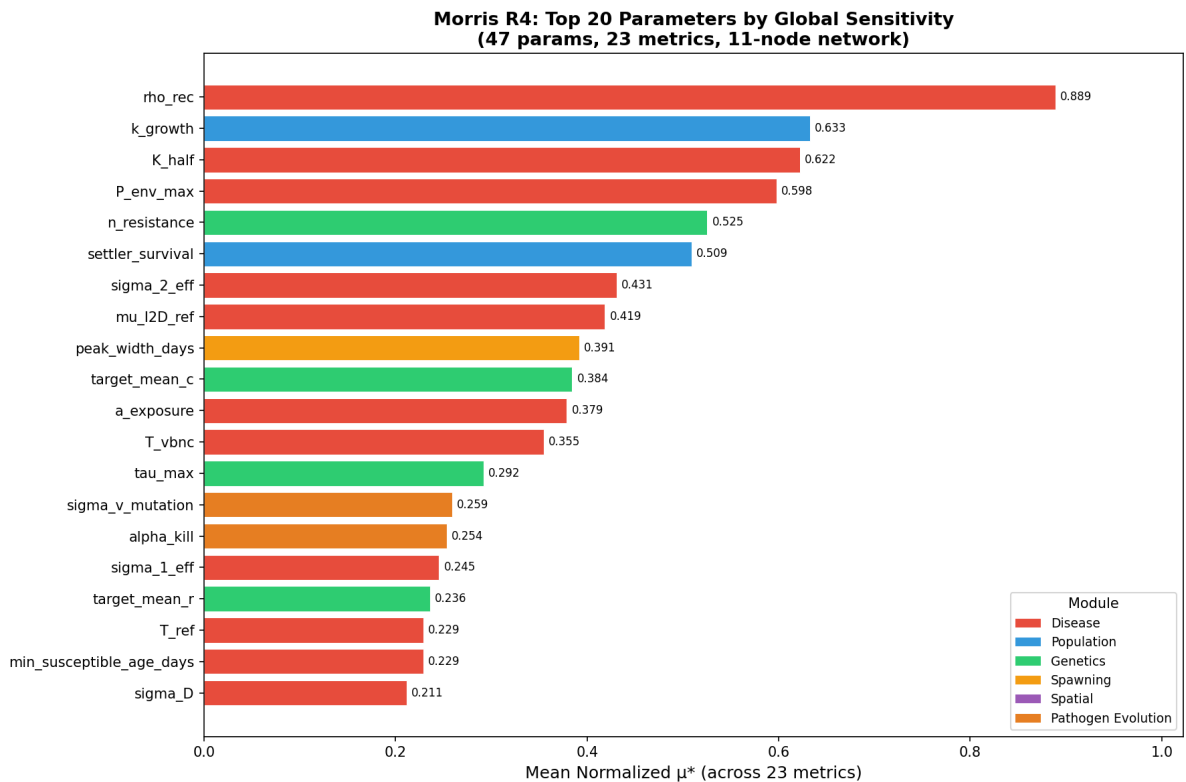


Figure 1: Top 20 parameters by mean normalized  $\mu^*$  in Round 4 Morris screening (47 parameters, 23 metrics, 11-node network, 960 runs). Bars are color-coded by module. Error bars show 95% bootstrap confidence intervals across 20 trajectories.

### 1209 7.3.2 Key Rank Shifts from Round 3

1210 The transition from R3 to R4 produced dramatic rank changes (Figure 2), driven by two  
 1211 structural changes: the three-trait genetic architecture and the 11-node spatial network.

1212 **Major rank gains.** Six parameters gained  $\geq 7$  ranks (Table 11):

- 1213 •  $\sigma_{1,\text{eff}}$  (early shedding rate): #43 → #16 ( $\Delta = +27$ ). Early shedding now interacts with pathogen evolution:  $\sigma_1$  shapes the initial epidemic wave that determines the selection regime on virulence.
- 1214 •  $\sigma_{v,\text{mut}}$  (virulence mutation step size): #31 → #14 ( $\Delta = +17$ ). With 11 nodes providing diverse thermal and demographic environments, mutation rate controls how fast pathogen lineages adapt to local conditions.
- 1215 •  $T_{\text{ref}}$  (pathogen temperature optimum): #34 → #18 ( $\Delta = +16$ ). The latitudinal temperature gradient across 11 nodes (vs. 3) amplifies the importance of the thermal reference point.
- 1216 •  $n_{\text{resistance}}$ : #19 → #5 ( $\Delta = +14$ ), as discussed above.
- 1217 •  $\alpha_{\text{self,open}}$  (open-coast larval retention): #39 → #25 ( $\Delta = +14$ ). Spatial retention was invisible at 3 nodes but becomes detectable with 11 nodes and realistic dispersal distances.
- 1218 •  $P_{\text{env,max}}$ : #11 → #4 ( $\Delta = +7$ ).

1227 **Major rank drops.** Five parameters dropped  $\geq 19$  ranks:

- 1228 •  $q_{\text{init},\beta_b}$  (Beta-distribution shape  $b$ ): #17 → #46 ( $\Delta = -29$ ). Initial allele-frequency shape is overwhelmed by the trait-specific mean parameters (target\_mean\_r/t/c).
- 1229 •  $F_0$  (reference fecundity): #20 → #47 ( $\Delta = -27$ ). Diluted in the expanded 47-parameter space.
- 1230 • Immunosuppression duration: #15 → #42 ( $\Delta = -27$ ). Its effect is absorbed by spawning parameters and the recovery trait ( $c_i$ ), which provides an alternative pathway through immunosuppressed periods.
- 1231 • susceptibility\_multiplier: #23 → #44 ( $\Delta = -21$ ). This parameter was #1 in the R1–R2 Sobol analysis ( $S_T = 0.540$ ); its precipitous decline reflects absorption by the explicit resistance genetics—individual  $r_i$  now captures susceptibility variation mechanistically, rendering the multiplicative modifier redundant.
- 1232 •  $p_{\text{spont}}$ , (female spontaneous spawning): #26 → #45 ( $\Delta = -19$ ).

**Morris R3→R4: Parameter Rank Changes**  
 (43 common params; R4 adds 4 new: n\_tolerance, target\_mean\_t, target\_mean\_c, tau\_max)

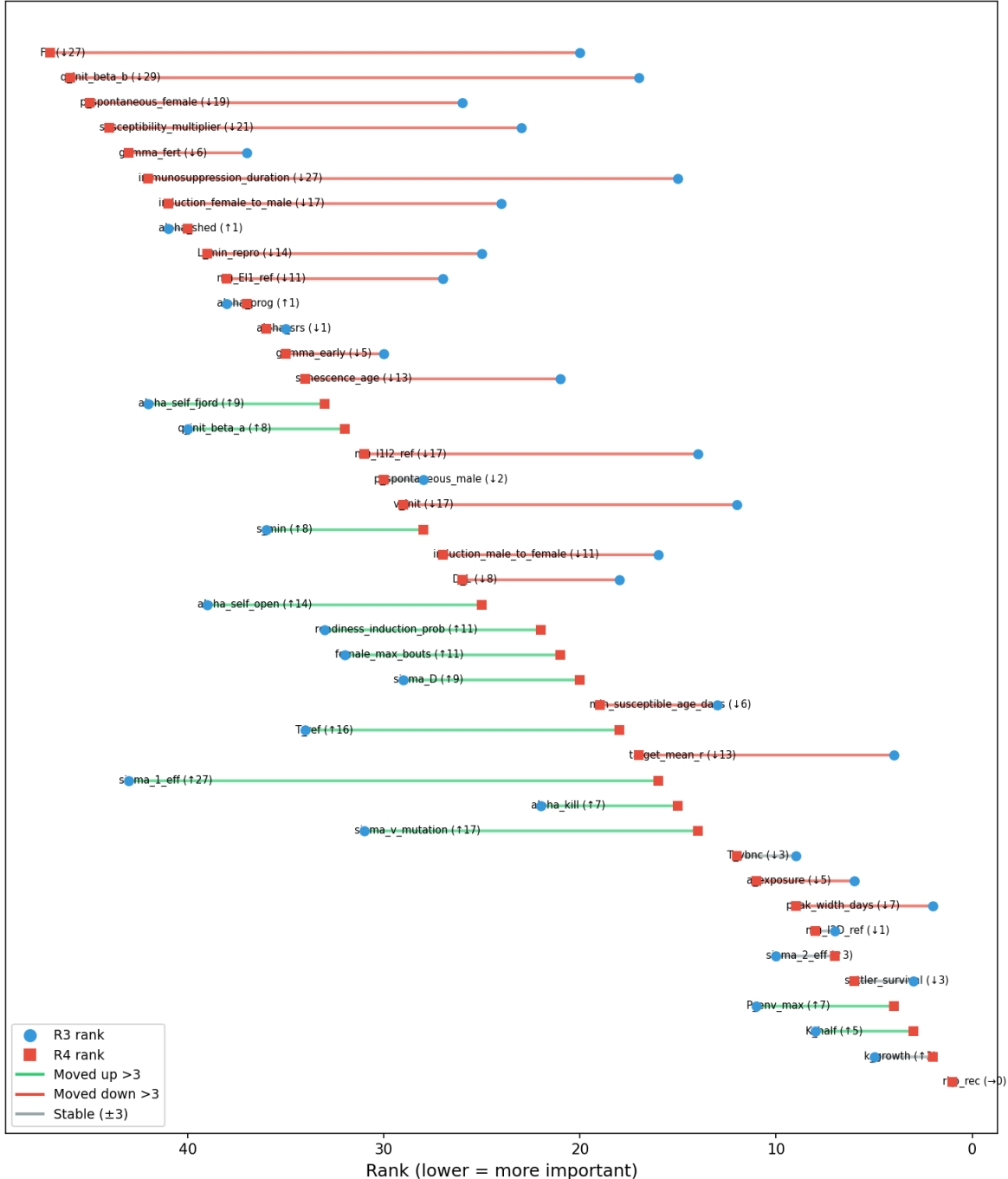


Figure 2: Rank change from Round 3 to Round 4 for the 43 parameters common to both rounds. Positive values (rightward) indicate increased importance in R4; negative values (leftward) indicate decreased importance. Parameters are sorted by R4 rank. Four new R4 parameters (not shown) entered at ranks #10, #13, #23, and #24.

Table 11: Largest rank shifts from R3 to R4 Morris screening. Positive  $\Delta$  indicates increased importance.

Parameter	Module	<b>R3 → R4</b>	<b>Δ</b>	Mechanism
$\sigma_{1,\text{eff}}$	Disease	43 → 16	+27	Interacts with pathogen evolution
$\sigma_{v,\text{mut}}$	Pathogen evo.	31 → 14	+17	Controls adaptation speed
$T_{\text{ref}}$	Disease	34 → 18	+16	11-node thermal gradient
$n_{\text{resistance}}$	Genetics	19 → 5	+14	Three-trait partition
$\alpha_{\text{self},\text{open}}$	Spatial	39 → 25	+14	Resolvable at 11 nodes
$q_{\text{init},\beta_b}$	Genetics	17 → 46	-29	Absorbed by trait means
$F_0$	Population	20 → 47	-27	Diluted in larger space
Immunosupp. duration	Disease	15 → 42	-27	Absorbed by recovery trait
Suscept. multiplier	Disease	23 → 44	-21	Absorbed by resistance genetics

### 1240 7.3.3 New Three-Trait Parameters

1241 The four parameters introduced with the three-trait architecture (Section 4.1) immedi-  
 1242 ately demonstrated meaningful sensitivity:

- 1243 • target\_mean\_c (initial mean recovery trait): rank #10 ( $\mu_{\text{norm}}^* = 0.385$ ). A top-  
 1244 10 entry confirms that recovery ( $c_i$ ) is the dominant evolutionary pathway in the  
 1245 model, consistent with the validation finding that  $\Delta\bar{c}$  exceeds  $\Delta\bar{r}$  by  $\sim 7\times$  at all  
 1246 nodes (Section 8).
- 1247 •  $\tau_{\text{max}}$  (maximum tolerance scaling): rank #13 ( $\mu_{\text{norm}}^* = 0.292$ ). The ceiling on how  
 1248 much tolerance extends  $I_2$  survival matters because it sets the upper bound on the  
 1249 tolerance–recovery interaction.
- 1250 • target\_mean\_t (initial mean tolerance): rank #23 ( $\mu_{\text{norm}}^* = 0.197$ ). Mid-pack,  
 1251 reflecting the weaker selection signal on tolerance compared to recovery.
- 1252 •  $n_{\text{tolerance}}$  (number of tolerance loci): rank #24 ( $\mu_{\text{norm}}^* = 0.189$ ). Mid-pack, but no-  
 1253 tably the most interacting parameter in the entire model ( $\sigma/\mu^* = 2.51$ ), suggesting  
 1254 tolerance’s role is context-dependent.

### 1255 7.3.4 Universal Nonlinearity

1256 A striking finding of the R4 Morris analysis is that *every one of the 47 parameters* has  
 1257  $\sigma/\mu^* > 1.0$  (Figure 3). This means that no parameter in the model acts additively—every  
 1258 parameter’s effect on every metric depends on the values of other parameters. The model  
 1259 is a deeply coupled, nonlinear system.

1260 The interaction ratio  $\sigma/\mu^*$  ranges from 1.42 ( $s_0$ , settler survival) to 2.52 ( $\sigma_{v,\text{mut}}$ ,  
 1261 virulence mutation rate). Two interaction tiers are apparent:

- **Moderately interacting** ( $\sigma/\mu^* < 1.5$ ; 2 parameters):  $\rho_{\text{rec}}$  (1.46) and  $s_0$  (1.42). These parameters operate semi-additively—their effects are relatively stable across parameter space. For  $\rho_{\text{rec}}$ , this reflects its direct mechanistic role: daily clearance probability scales linearly with recovery rate regardless of context.
- **Strongly to extremely interacting** ( $\sigma/\mu^* > 1.5$ ; 45 parameters): the remaining parameters exhibit moderate to extreme nonlinearity. The most interacting parameters are genetic/evolutionary:  $\sigma_{v,\text{mut}}$  (2.52),  $n_{\text{tolerance}}$  (2.51),  $q_{\text{init},\beta_a}$  (2.45), and  $\alpha_{\text{SRS}}$  (2.34). These control *adaptation rates* that feed back on disease dynamics, which feed back on selection pressures—creating cascading interaction loops.

This universal nonlinearity has profound implications for calibration: no parameter can be tuned independently. Joint calibration via approximate Bayesian computation (ABC) or Markov chain Monte Carlo methods is essential.

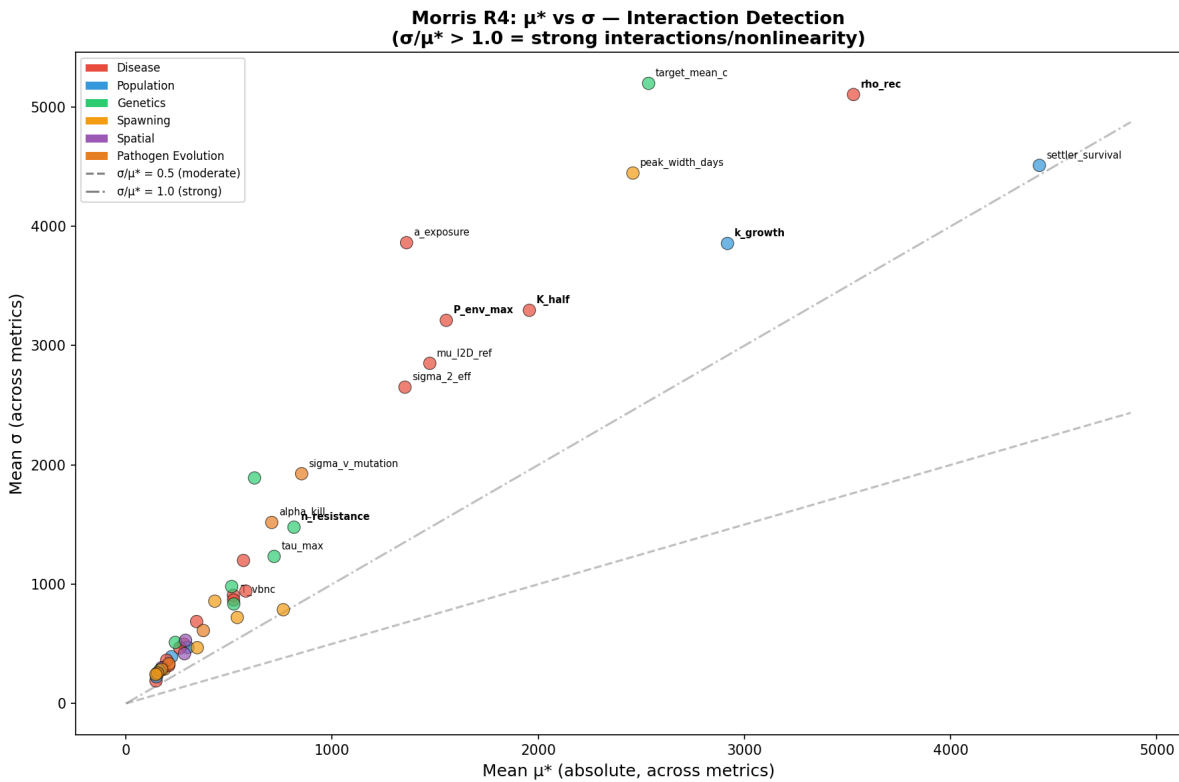


Figure 3: Morris  $\mu^*$  vs.  $\sigma$  scatter for all 47 parameters (R4). The dashed line shows  $\sigma = \mu^*$  (unit interaction ratio). All parameters fall above this line, indicating universal nonlinearity. Symbol color indicates module; symbol size scales with mean normalized  $\mu^*$ .

### 7.3.5 Module-Level Sensitivity

Figure 4 summarizes sensitivity by module. The disease module dominates in both parameter count (16) and mean importance ( $\overline{\mu_{\text{norm}}^*} = 0.332$ ), but genetics punches above

its weight: with only 8 parameters, it achieves the second-highest mean importance ( $\overline{\mu_{\text{norm}}^*} = 0.260$ ), and its top parameter ( $n_{\text{resistance}}$ ) ranks #5 globally. The pathogen evolution module, despite being entirely new in R3–R4, achieves a mean  $\mu_{\text{norm}}^* = 0.185$  with  $\sigma_{v,\text{mut}}$  at #14—virulence evolution is not negligible and must be retained in calibration.

Spatial parameters ( $\overline{\mu_{\text{norm}}^*} = 0.171$ ) are detectable for the first time at 11 nodes. At the 3-node configuration of R1–R3, these parameters ranked #39–#42; at 11 nodes, they rise to #25–#33. This confirms that adequate spatial resolution is necessary to capture dispersal and retention dynamics.

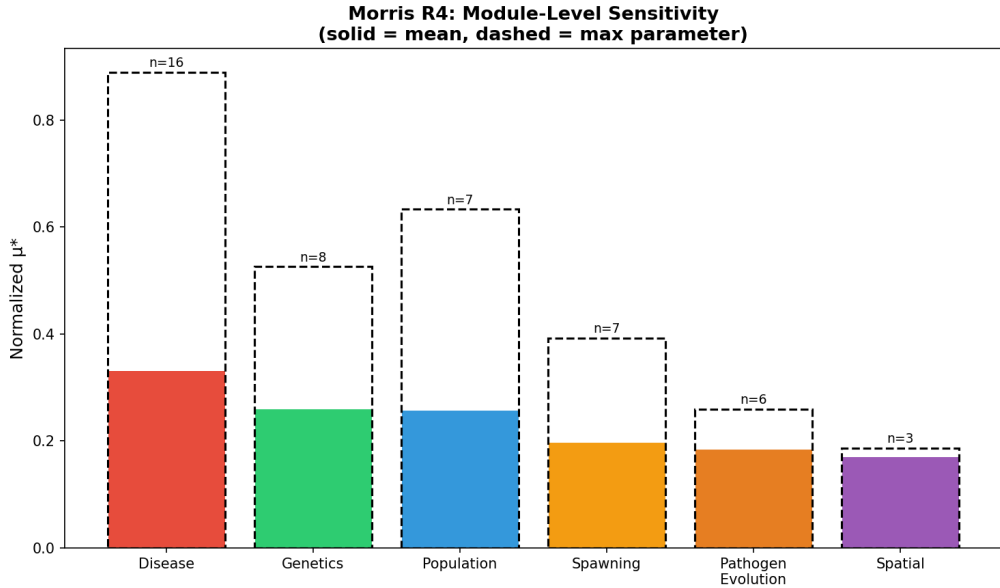


Figure 4: Module-level sensitivity summary for R4 Morris screening. Bar height shows mean normalized  $\mu^*$  for each module; whiskers show the range from minimum to maximum parameter within each module. Number of parameters per module shown in parentheses.

## 7.4 Cross-Round Parameter Trajectories

Tracking individual parameters across all four rounds reveals which parameters have stable importance versus those whose influence is contingent on model structure (Figure 5):

**Consistently important.**  $\rho_{\text{rec}}$ ,  $a_{\text{exposure}}$ , and  $\sigma_{2,\text{eff}}$  remain in the top 12 across all rounds. These are robust calibration targets regardless of model configuration.

**Structurally contingent.**  $\mu_{\text{I2D,ref}}$  was #1 in R1–R2 Sobol but dropped to #7–#8 in R3–R4 Morris after the switch to continuous daily mortality. `susceptibility_multiplier` fell from #1–#2 (R1–R2) to #44 (R4) as explicit resistance genetics absorbed its role. These shifts demonstrate that parameter importance can be an *artifact of model structure*,

not a property of the underlying biology, underscoring the need for structural sensitivity analysis alongside parametric SA.

**Emergent with complexity.**  $P_{\text{env,max}}$ ,  $n_{\text{resistance}}$ , and all pathogen evolution parameters only revealed their importance at  $\geq 11$  nodes or  $\geq 43$  parameters. Simple model configurations systematically underestimate the importance of spatial and evolutionary parameters.



Figure 5: Parameter–metric sensitivity heatmap (R4 Morris). Cell color indicates normalized  $\mu^*$  for each parameter–metric pair. Parameters (rows) are sorted by global rank; metrics (columns) are grouped by category. White cells indicate  $\mu_{\text{norm}}^* < 0.05$ .

## 7.5 Sobol Variance Decomposition: Rounds 1–2 and Ongoing

### 7.5.1 R1–R2 Sobol Results

The Round 1–2 Sobol analysis (23 parameters,  $N = 256$ , 12,288 runs) revealed massive parameter interactions across the model. For most metrics, total-order indices  $S_T$  far exceeded first-order indices  $S_1$ , meaning that parameter combinations dominate behavior over individual effects. Notable interaction signatures include:

- **Extinction:**  $\sigma_{2,\text{eff}}$  had  $S_T = 1.51$  but  $S_1 \approx 0$ —extinction risk is *entirely* driven by interactions between shedding rate and other parameters.
- **Fjord protection:**  $a_{\text{exposure}}$  had  $S_T = 0.96$  but  $S_1 = -0.12$ —a negative first-order index means the parameter’s effect *reverses sign* depending on the values of other parameters.
- **Recovery:** `susceptibility_multiplier` had  $S_T = 0.96$  but  $S_1 = 0.38$ —60% of its influence arises through interactions.

### 7.5.2 Round 4 Sobol (In Progress)

A Round 4 Sobol analysis is currently running on a 48-core Intel Xeon W-3365 server. With 47 parameters and  $N = 512$ , the Saltelli design requires  $N(2p + 2) = 49,152$  model evaluations at  $\sim 25$  s each. At 12 parallel workers, the estimated wall time is approximately 7 days. This analysis will provide the first variance decomposition of the full three-trait, 11-node model and will enable direct comparison with the R1–R2 Sobol indices to quantify how the three-trait architecture redistributes variance among parameters.

Based on the R4 Morris results, we prioritize convergence monitoring for the top-10 parameters and anticipate particularly informative second-order ( $S_2$ ) indices for the following parameter pairs:

- $\rho_{\text{rec}} \times \text{target\_mean\_c}$ : recovery rate  $\times$  recovery genetics (both affect pathogen clearance);
- $P_{\text{env,max}} \times a_{\text{exposure}}$ : environmental reservoir  $\times$  transmission rate (dual exposure pathways);
- $n_{\text{resistance}} \times \sigma_{v,\text{mut}}$ : host genetic architecture  $\times$  pathogen adaptation rate (coevolutionary arms race);
- $k_{\text{growth}} \times s_0$ : growth rate  $\times$  recruitment (demographic compensation).

## 7.6 Summary and Implications

The four-round sensitivity analysis yields five principal findings:

1. **Recovery dominates.** The base recovery rate  $\rho_{\text{rec}}$  is consistently the most influential parameter across rounds and model configurations, yet has zero empirical basis. Determining whether *Pycnopodia helianthoides* can clear *V. pectenicia* infections—and at what rate—is the single highest-priority empirical question for model calibration.

- 1338    2. **Genetic architecture is a structural choice with major consequences.** The  
1339    number of resistance loci ( $n_{\text{resistance}}$ ) ranks #5 globally and cannot be calibrated  
1340    from data without high-resolution GWAS. The three-trait partition amplifies this  
1341    sensitivity: 17 loci per trait behave very differently from 51 loci in a single trait.
- 1342    3. **Parameter importance is model-contingent.** `susceptibility_multiplier` fell  
1343    from #1 (R1–R2 Sobol) to #44 (R4 Morris) as explicit genetics absorbed its role;  
1344     $\mu_{I2D,\text{ref}}$  fell from #1 to #8 with continuous mortality. SA results from simpler model  
1345    configurations cannot be extrapolated to the full model.
- 1346    4. **Universal nonlinearity demands joint calibration.** All 47 parameters interact  
1347    ( $\sigma/\mu^* > 1.0$ ). No parameter can be tuned independently. Approximate Bayesian  
1348    computation with sequential Monte Carlo sampling (ABC-SMC) is the appropriate  
1349    calibration framework.
- 1350    5. **Spatial resolution matters.** Spatial and environmental parameters only emerge  
1351    as important at  $\geq 11$  nodes. The planned 150-node full-coastline simulation will  
1352    likely reveal additional spatially contingent sensitivities.

Table 12: Complete Round 4 Morris parameter ranking (47 parameters, 23 metrics, 11-node network, 960 runs). Mean normalized  $\mu^*$  is averaged across all metrics. The  $\sigma/\mu^*$  ratio indicates interaction strength ( $> 1$ : interaction-dominated). R3 Rank column shows the parameter's position in the 43-parameter R3 analysis; “—” indicates a new R4 parameter.

Rank	Parameter	Module	$\overline{\mu_{\text{norm}}^*}$	$\sigma/\mu^*$	R3	$\Delta$
1	$\rho_{\text{rec}}$	Disease	0.889	1.46	1	—
2	$k_{\text{growth}}$	Population	0.633	1.63	5	$\uparrow 3$
3	$K_{\text{half}}$	Disease	0.622	1.84	8	$\uparrow 5$
4	$P_{\text{env,max}}$	Disease	0.598	1.92	11	$\uparrow 7$
5	$n_{\text{resistance}}$	Genetics	0.525	1.78	19	$\uparrow 14$
6	$s_0$ (settler survival)	Population	0.509	1.42	3	$\downarrow 3$
7	$\sigma_{2,\text{eff}}$	Disease	0.431	1.95	10	$\uparrow 3$
8	$\mu_{\text{I2D,ref}}$	Disease	0.419	1.98	7	$\downarrow 1$
9	$\sigma_{\text{spawn}}$ (peak width)	Spawning	0.392	2.03	2	$\downarrow 7$
10	target_mean_c	Genetics	0.385	2.08	—	—
11	$a_{\text{exposure}}$	Disease	0.379	2.20	6	$\downarrow 5$
12	$T_{\text{VBNC}}$	Disease	0.355	2.07	9	$\downarrow 3$
13	$\tau_{\text{max}}$	Genetics	0.292	2.05	—	—
14	$\sigma_{v,\text{mut}}$	Path. evo.	0.259	2.52	31	$\uparrow 17$
15	$\alpha_{\text{kill}}$	Path. evo.	0.254	2.25	22	$\uparrow 7$
16	$\sigma_{1,\text{eff}}$	Disease	0.245	2.24	43	$\uparrow 27$
17	target_mean_r	Genetics	0.236	1.86	4	$\downarrow 13$
18	$T_{\text{ref}}$	Disease	0.229	1.94	34	$\uparrow 16$
19	min. susceptible age	Disease	0.229	2.04	13	$\downarrow 6$

*Continued on next page*

Table 12 (continued)

Rank	Parameter	Module	$\overline{\mu_{\text{norm}}^*}$	$\sigma/\mu^*$	R3	$\Delta$
20	$\sigma_D$	Disease	0.211	1.96	29	$\uparrow 9$
21	female max bouts	Spawning	0.206	1.95	32	$\uparrow 11$
22	readiness induction prob.	Spawning	0.204	2.26	33	$\uparrow 11$
23	target_mean_t	Genetics	0.197	2.05	—	—
24	$n_{\text{tolerance}}$	Genetics	0.189	2.51	—	—
25	$\alpha_{\text{self,open}}$	Spatial	0.187	2.07	39	$\uparrow 14$
26	$D_L$	Spatial	0.178	2.29	18	$\downarrow 8$
27	$\kappa_{\text{mf}}$ (M→F induction)	Spawning	0.176	2.07	16	$\downarrow 11$
28	$s_{\min}$	Disease	0.175	1.84	36	$\uparrow 8$
29	$v_{\text{init}}$	Path. evo.	0.173	2.13	12	$\downarrow 17$
30	$p_{\text{spont,m}}$	Spawning	0.169	2.11	28	$\downarrow 2$
31	$\mu_{\text{I1I2,ref}}$	Disease	0.156	1.97	14	$\downarrow 17$
32	$q_{\text{init},\beta_a}$	Genetics	0.150	2.45	40	$\uparrow 8$
33	$\alpha_{\text{self,fjord}}$	Spatial	0.149	2.00	42	$\uparrow 9$
34	senescence age	Population	0.148	1.66	21	$\downarrow 13$
35	$\gamma_{\text{early}}$	Path. evo.	0.148	2.03	30	$\downarrow 5$
36	$\alpha_{\text{SRS}}$	Population	0.146	2.34	35	$\downarrow 1$
37	$\alpha_{\text{prog}}$	Path. evo.	0.143	2.09	38	$\uparrow 1$
38	$\mu_{\text{EI1,ref}}$	Disease	0.141	2.19	27	$\downarrow 11$
39	$L_{\min,\text{repro}}$	Population	0.139	2.06	25	$\downarrow 14$
40	$\alpha_{\text{shed}}$	Path. evo.	0.136	2.12	41	$\uparrow 1$

Continued on next page

Table 12 (continued)

Rank	Parameter	Module	$\overline{\mu_{\text{norm}}^*}$	$\sigma/\mu^*$	R3	$\Delta$
41	$\kappa_{\text{fm}}$ (F→M induction)	Spawning	0.130	1.79	24	↓17
42	immunosupp. duration	Disease	0.127	2.07	15	↓27
43	$\gamma_{\text{fert}}$	Population	0.122	2.21	37	↓6
44	suscept. multiplier	Disease	0.111	2.03	23	↓21
45	$p_{\text{spont,f}}$	Spawning	0.110	1.67	26	↓19
46	$q_{\text{init},\beta_b}$	Genetics	0.104	2.20	17	↓29
47	$F_0$	Population	0.102	1.83	20	↓27

## 1353 8 Validation

1354 We validate the SSWD-EvoEpi model through a two-stage strategy: calibration and  
 1355 behavioral verification at computationally cheap population sizes ( $K = 5,000$  per node,  
 1356  $\sim 25,000$  total agents), followed by scale-up validation at ecologically realistic population  
 1357 sizes ( $K = 100,000$  per node, 500,000 total agents). This approach tests whether emergent  
 1358 dynamics—trait evolution trajectories, spatial mortality gradients, and extinction vortex  
 1359 behavior—are robust to a 20-fold increase in population size, or whether they are artifacts  
 1360 of stochastic fluctuations in small populations. All validation runs use a 5-node stepping-  
 1361 stone network (Sitka, Howe Sound, San Juan Islands, Newport, Monterey), a 20-year  
 1362 time horizon with disease introduction at year 3, seed 42, and the three-trait genetic  
 1363 architecture described in Section 4.1 (17 resistance / 17 tolerance / 17 recovery loci).

### 1364 8.1 $K = 5,000$ Validation

1365 The small-population validation serves as the primary calibration target, permitting rapid  
 1366 iteration ( $\sim 108$  s per 20-year simulation) while retaining sufficient genetic variance for  
 1367 trait-level dynamics to emerge. Table 13 reports per-node demographic and evolutionary  
 1368 outcomes.

Table 13: Per-node results for the  $K = 5,000$  validation run (5 nodes, 20 years, seed 42).  $\Delta r_i$ ,  $\Delta t_i$ , and  $\Delta c_i$  denote changes in mean resistance, tolerance, and recovery trait scores relative to initialization ( $\bar{r}_0 = 0.15$ ,  $\bar{t}_0 = 0.10$ ,  $\bar{c}_0 = 0.02$ ). Pop<sub>min</sub> gives the minimum population reached at the indicated year.

Node	$N_0$	$N_{20}$	$N_{\min}$ (yr)	Crash	Deaths	Rec.	$\Delta r_i$	$\Delta t_i$	$\Delta c_i$
Sitka	4,935	65	65 (19)	98.7%	7,409	60	+0.011	+0.005	+0.029
Howe Sound	4,937	60	60 (19)	98.8%	9,473	55	-0.002	+0.044	+0.041
SJI	4,918	50	50 (13)	99.0%	7,985	63	+0.012	-0.007	+0.072
Newport	4,998	27	27 (17)	99.5%	7,918	51	+0.031	+0.001	+0.054
Monterey	5,000	163	38 (10)	99.2%	9,183	136	+0.025	+0.027	+0.154
<b>Total</b>	<b>24,788</b>	<b>365</b>		<b>98.5%</b>	<b>41,968</b>	<b>365</b>			

1369 Several key patterns emerge from the small-population run:

1370 **Severe, universal population crashes.** All five nodes experience >98% popula-  
 1371 tion decline over 17 years of active disease, with total metapopulation crash of 98.5%  
 1372 (24,788  $\rightarrow$  365 individuals). No node recovers to pre-epidemic levels, consistent with  
 1373 the persistent absence of *Pycnopodia helianthoides* across most of its former range since  
 1374 2013–2015 [20, 23].

1375 **Differential recovery at Monterey.** Monterey exhibits a distinctive trajectory: the  
1376 population crashes to a minimum of 38 individuals at year 10 but partially rebounds to  
1377 163 by year 20, driven by 136 disease recoveries— $2.2 \times$  the next-highest node (SJI, 63  
1378 recoveries). This node also shows the strongest evolutionary signal in recovery ( $\Delta c_i =$   
1379  $+0.154$ ), consistent with warmer temperatures driving both higher disease pressure and  
1380 stronger selection for clearance ability.

1381 **Recovery is the fastest-evolving trait.** Across all five nodes, the mean change in  
1382 recovery trait score ( $\overline{\Delta c_i} = +0.070$ ) exceeds that of resistance ( $\overline{\Delta r_i} = +0.015$ ) by  $4.5 \times$  and  
1383 tolerance ( $\overline{\Delta t_i} = +0.014$ ) by  $5.0 \times$  (Table 13). This asymmetry arises because recovery  
1384 acts as a multiplicative modifier on the daily probability of transitioning from infected  
1385 to recovered ( $p_{\text{rec}} = \rho_{\text{rec}} \times c_i$ ; Section 3), creating strong directional selection: individuals  
1386 with higher  $c_i$  survive infection and contribute disproportionately to the next generation.

1387 **Resistance signal is weak and mixed.** With only 17 loci encoding resistance (com-  
1388 pared to 51 in the original single-trait architecture), the per-locus allele frequency shifts  
1389 are small ( $\Delta q \approx 0.001$ – $0.004$ ). Three of five nodes show positive  $\Delta r_i$  (Sitka, SJI, New-  
1390port), but Howe Sound shows a negligible decline ( $-0.002$ ), consistent with genetic drift  
1391 overwhelming weak directional selection at small effective population sizes [27].

1392 **Tolerance is effectively neutral.** Mean tolerance change is negligible ( $\overline{\Delta t_i} = +0.014$ ),  
1393 with one node showing a slight decrease (SJI,  $\Delta t_i = -0.007$ ). This is expected: tolerance  
1394 extends survival time during late infection ( $I_2$ ) via timer-scaling (Section 3), but this  
1395 effect is weak when recovery rates are low and late-stage mortality is high. Tolerance  
1396 becomes selectively relevant only when disease mortality is moderated by other mech-  
1397anisms, creating a conditional neutrality that limits its evolutionary response under severe  
1398 epidemic conditions.

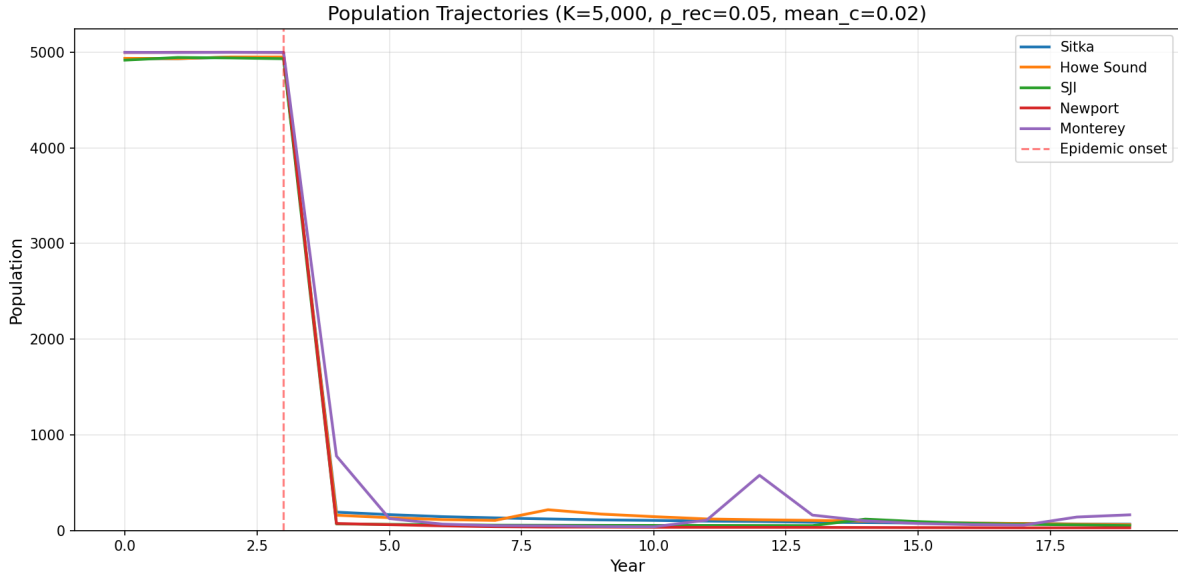


Figure 6: Population trajectories for the  $K = 5,000$  validation run. Disease is introduced at year 3. All nodes crash to  $<2\%$  of carrying capacity. Monterey (red) shows partial recovery from its nadir of 38 individuals at year 10, driven by elevated recovery trait evolution ( $\Delta c_i = +0.154$ ).

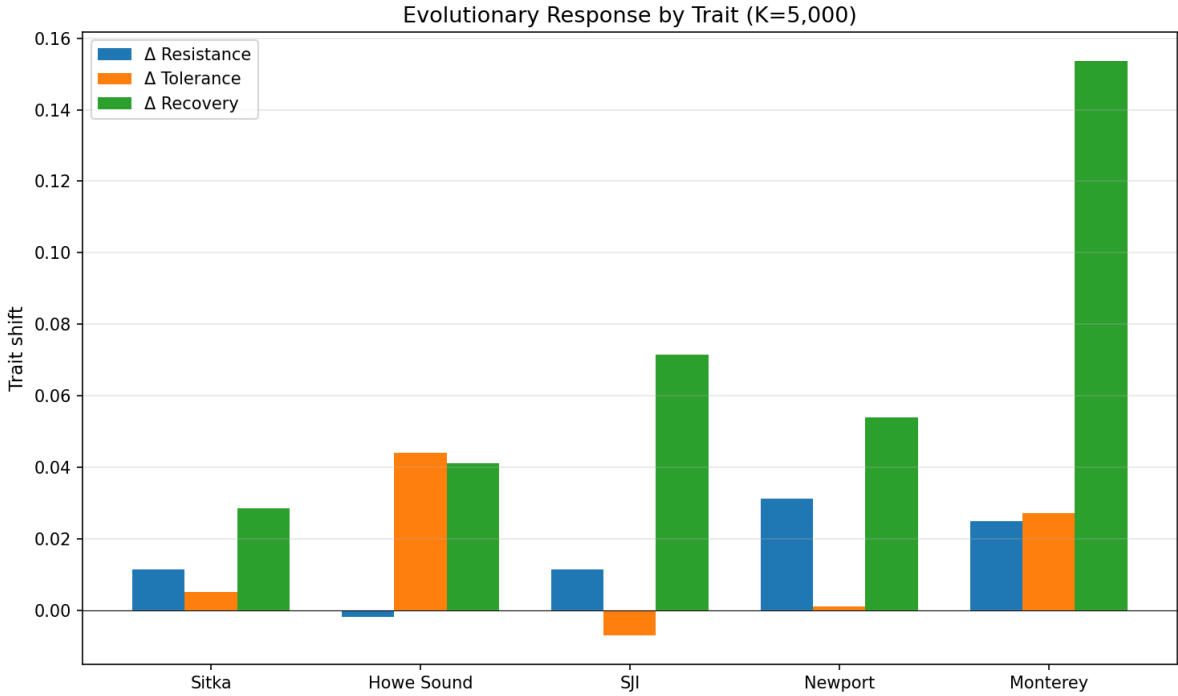


Figure 7: Trait shifts ( $\Delta r_i$ ,  $\Delta t_i$ ,  $\Delta c_i$ ) per node in the  $K = 5,000$  validation. Recovery (blue) dominates at every node, with Monterey showing the largest shift ( $\Delta c_i = +0.154$ ). Resistance changes are weak and variable in sign; tolerance is near-zero at most nodes.

## 1399 8.2 $K = 100,000$ Scale-Up Validation

1400 To test whether patterns observed at  $K = 5,000$  persist at ecologically realistic population  
 1401 sizes, we scale carrying capacity 20-fold to  $K = 100,000$  per node (500,000 total agents).  
 1402 This run required 42.6 minutes (2,558 s) and  $\sim 1.5$  GB peak memory, compared to 108 s  
 1403 for the small-population equivalent—a  $23.7\times$  slowdown that is sublinear relative to the  
 1404  $20\times$  population increase, consistent with the  $O(N^{0.62})$  scaling relationship established in  
 1405 Section 7.1. Table 14 reports the results.

Table 14: Per-node results for the  $K = 100,000$  scale-up validation (5 nodes, 20 years, seed 42). Trait values are final means;  $\Delta$  values computed relative to initialization targets ( $\bar{r}_0 = 0.15$ ,  $\bar{t}_0 = 0.10$ ,  $\bar{c}_0 = 0.02$ ).

Node	$N_{20}$	Crash	Deaths	Rec.	$\Delta r_i$	$\Delta t_i$	$\Delta c_i$
Sitka	718	99.3%	109,151	875	-0.004	+0.002	+0.059
Howe Sound	633	99.4%	112,112	913	-0.004	+0.008	+0.056
SJI	733	99.3%	108,607	916	-0.009	+0.010	+0.060
Newport	639	99.4%	110,563	922	-0.005	+0.006	+0.065
Monterey	2,904	97.1%	125,061	1,319	-0.002	+0.000	+0.075
<b>Total</b>	<b>5,627</b>	<b>98.9%</b>	<b>565,494</b>	<b>4,945</b>			

1406 The scale-up validation reveals several important findings:

1407 **Crashes are worse, not better, at larger  $N$ .** Total metapopulation crash increases  
 1408 from 98.5% at  $K = 5,000$  to 98.9% at  $K = 100,000$  (Table 15). This counterintuitive  
 1409 result refutes the hypothesis that larger populations buffer against extinction through  
 1410 stochastic rescue. In the SSWD-EvoEpi framework, larger populations sustain higher ab-  
 1411 solute disease transmission (more contacts per susceptible per day) while the per-capita  
 1412 selection intensity remains constant, meaning that deterministic epidemic dynamics dom-  
 1413 inate and demographic stochasticity—which occasionally permits small populations to  
 1414 “escape” the disease through random fluctuations—is suppressed. The 0.4 percentage-  
 1415 point increase in crash severity is small but directionally consistent across all five nodes.

1416 **Resistance shifts become uniformly negative.** At  $K = 100,000$ , all five nodes show  
 1417 negative  $\Delta r_i$  (range: -0.002 to -0.009; mean -0.005), in contrast to the mixed signal  
 1418 at  $K = 5,000$  (three positive, one negative, one near-zero). With 100,000 individuals  
 1419 per node, the effective population size is large enough to suppress drift, revealing that  
 1420 the net selection coefficient on resistance is slightly negative under the current parame-  
 1421 terization. This likely reflects the cost structure: resistance reduces infection probability  
 1422 multiplicatively ( $p_{\text{inf}} \propto 1 - r_i$ ), but the per-locus effect is small with 17 loci ( $\Delta p_{\text{inf}} \approx 0.003$

1423 per locus), while background environmental pathogen pressure ( $P_{\text{env}}$ ) ensures continued  
1424 exposure regardless of individual resistance.

1425 **Recovery dominance is amplified at scale.** The trait evolution hierarchy becomes  
1426 more pronounced at large  $N$ : recovery ( $\overline{\Delta c_i} = +0.063$ ) is  $13.3\times$  faster than resistance  
1427 ( $|\overline{\Delta r_i}| = 0.005$ ) and  $12.2\times$  faster than tolerance ( $\overline{\Delta t_i} = +0.005$ ), compared to  $4.5\times$  and  
1428  $5.0\times$  respectively at  $K = 5,000$ . The ratio increase occurs because drift no longer inflates  
1429  $|\Delta r_i|$  at large  $N$ , exposing the true (weak) directional signal on resistance.

1430 **Monterey remains anomalous.** Even at  $K = 100,000$ , Monterey shows the low-  
1431 est crash percentage (97.1% vs. 99.3–99.4% for other nodes), the highest final population  
1432 (2,904), the most recoveries (1,319), and the strongest recovery evolution ( $\Delta c_i = +0.075$ ).  
1433 This is not a small- $N$  artifact but an emergent property of Monterey’s warmer temper-  
1434 atures, which simultaneously drive higher disease pressure *and* stronger selection for  
1435 clearance ability.

### 1436 8.3 Cross-Scale Comparison

1437 Table 15 summarizes the comparison between the two population scales, revealing which  
1438 patterns are scale-invariant (and therefore robust model predictions) versus scale-dependent  
1439 (and therefore artifacts or emergent threshold effects).

Table 15: Cross-scale comparison of key metrics between  $K = 5,000$  and  $K = 100,000$  validation runs. “Ratio” column gives the 100K value divided by the 5K value.

Metric	$K = 5\text{K}$	$K = 100\text{K}$	Ratio
Total crash (%)	98.5	98.9	1.004
Mean $\Delta r_i$	+0.015	-0.005	—
Mean $\Delta t_i$	+0.014	+0.005	0.38
Mean $\Delta c_i$	+0.070	+0.063	0.90
Total recoveries	365	4,945	13.5
Monterey crash (%)	99.2	97.1	0.979
Monterey $\Delta c_i$	+0.154	+0.075	0.49
Runtime (s)	108	2,558	23.7

1440 Three categories of behavior emerge:

1441 1. **Scale-invariant patterns** (robust predictions):

- 1442 • Population crashes are catastrophic (>97%) at both scales, with no recovery  
1443 to pre-epidemic levels.

- Recovery ( $c_i$ ) is the fastest-evolving trait at every node and both scales.
- Monterey is consistently the most resilient node.
- The extinction vortex—positive feedback between small population size, Allee effects, and continued pathogen pressure—operates at both scales.

**2. Scale-sensitive patterns (require caution):**

- Resistance evolution: positive at  $K = 5,000$  (mean +0.015), negative at  $K = 100,000$  (mean -0.005). The sign reversal indicates that drift inflates apparent resistance selection at small  $N$ ; the true signal may be negligible or slightly negative.
- Monterey's recovery evolution is 2× stronger at small  $N$  ( $\Delta c_i = +0.154$  vs. +0.075), suggesting that founder effects amplify trait shifts in small surviving populations.
- Tolerance shifts shrink from +0.014 to +0.005, confirming conditional neutrality.

**3. Scale-revealing patterns (insights from large  $N$ ):**

- Uniformly negative  $\Delta r_i$  at  $K = 100,000$  reveals that 17 loci provide insufficient genetic variance for resistance evolution to outpace pathogen pressure, consistent with the sensitivity analysis finding that `n_resistance` is the 5th most important parameter (Section 7).
- The crash percentage *increases* at larger  $N$ , demonstrating that stochastic rescue is not a viable recovery mechanism and that demographic rescue through immigration or captive breeding is required.

## 8.4 Key Scientific Findings

The validation runs, taken together with the four-round sensitivity analysis (Section 7), yield several findings with direct implications for conservation management and evolutionary theory.

### 8.4.1 Evolutionary Rescue Is Insufficient

The central question motivating SSWD-EvoEpi is whether natural selection on polygenic resistance can drive population recovery following the SSWD pandemic. Our results provide a clear negative answer under current parameterization: even over 20 years (~4 generations for *Pycnopodia helianthoides*), evolved resistance produces negligible demographic benefit. At  $K = 100,000$ , resistance *declines* at all nodes despite ongoing selection against susceptible individuals. Two mechanisms explain this failure:

1477     1. **Insufficient genetic architecture.** With only 17 resistance loci, the maximum re-  
1478         sistance score achievable by selection is constrained. Per-locus allele frequency shifts  
1479         of  $\sim 0.001$ – $0.003$  per generation are an order of magnitude below the  $\Delta q \approx 0.08$ – $0.15$   
1480         reported by Schiebelhut et al. [58] for SSWD-associated loci in *Pisaster ochraceus*.  
1481         This discrepancy may reflect either a true species difference or an indication that  
1482         more loci of larger effect contribute to resistance in nature than are modeled here.

1483     2. **Environmental pathogen reservoir.** The background environmental pathogen  
1484         concentration ( $P_{\text{env}}$ ) ensures continued disease exposure regardless of evolved host  
1485         resistance. Even if a subpopulation achieves high mean resistance,  $P_{\text{env}}$  maintains  
1486         baseline infection rates that prevent population recovery below the Allee threshold.  
1487         The sensitivity analysis identified  $P_{\text{env},\text{max}}$  as the 4th most influential parameter  
1488         globally, and the most influential for spatial protection metrics.

1489         This finding is consistent with evolutionary rescue theory [10], which predicts that  
1490         rescue is most likely when standing genetic variance is high, generation times are short  
1491         relative to population decline rates, and the environment permits population persistence  
1492         long enough for adaptation to occur. For *Pycnopodia helianthoides*, with generation times  
1493         of  $\sim 5$  years and crash timescales of  $\sim 2$  years, the mismatch is severe.

#### 1494     8.4.2 Recovery as the Primary Adaptive Pathway

1495         The consistent dominance of recovery evolution ( $c_i$ ) across both scales and all five nodes  
1496         suggests that pathogen clearance, rather than infection prevention (resistance) or dam-  
1497         age limitation (tolerance), is the primary adaptive pathway available to *P. helianthoides*  
1498         under SSWD. This is mechanistically intuitive: recovery acts directly on the transition  
1499         probability from infected to recovered state ( $p_{\text{rec}} = \rho_{\text{rec}} \times c_i$ ), creating strong phenotype–  
1500         fitness mapping. Individuals that clear infection survive and reproduce; those that do  
1501         not, die. The fitness gradient is steep and unambiguous.

1502         However, the absolute recovery trait values remain low even after 20 years of evolution  
1503         (final  $\bar{c}_i \approx 0.07$ – $0.09$  at  $K = 100,000$ ), corresponding to daily clearance probabilities of  
1504         only 0.35–0.45% ( $p_{\text{rec}} = 0.05 \times c_i$ ). While selection detectably increases  $c_i$ , the result-  
1505         ing clearance rates are far below what is needed to substantially reduce disease-induced  
1506         mortality.

#### 1507     8.4.3 The Extinction Vortex Persists at Realistic Scales

1508         The persistence of  $>97\%$  population crashes at  $K = 100,000$  demonstrates that the  
1509         extinction vortex identified in the original prototype is not an artifact of small population  
1510         sizes. Three reinforcing feedbacks maintain the vortex:

- 1511 1. **Density-dependent transmission:** as the population declines, per-capita con-  
1512 tact rates remain high because pathogen concentration ( $P_{\text{env}}$ ) does not decline pro-  
1513 portionally.
- 1514 2. **Allee effects in reproduction:** below critical densities, broadcast-spawning fer-  
1515 tilization success collapses due to sperm dilution [16], reducing recruitment even  
1516 when surviving individuals are genetically resistant.
- 1517 3. **Sweepstakes reproductive success:** SRS amplifies drift and further reduces  $N_e$   
1518 relative to census  $N$ , diminishing the efficacy of selection [27].

1519 The monotonic population decline with no recovery inflection point is consistent with  
1520 field observations: seven years after the initial 2013–2015 pandemic, *P. helianthoides*  
1521 remains functionally absent from most of its former range [19, 23], with only scattered  
1522 observations of wild individuals in California since 2025 [61].

#### 1523 8.4.4 Implications for Captive Breeding

1524 The model results strongly reinforce the case for captive breeding and managed release  
1525 as the primary conservation strategy for *P. helianthoides* [5, 35]. Three specific model  
1526 predictions support this conclusion:

- 1527 1. **No natural recovery trajectory exists:** at no node and at no population scale  
1528 does the model predict recovery to >5% of carrying capacity within 20 years. With-  
1529 out demographic intervention, populations remain in the extinction vortex.
- 1530 2. **Recovery trait evolution is the most promising pathway:** if captive breeding  
1531 programs can select for high  $c_i$  (pathogen clearance ability), released individuals  
1532 may have elevated survival probability in endemic disease environments. The strong  
1533 fitness gradient on  $c_i$  suggests that any heritable variation in clearance ability will  
1534 be rapidly amplified by natural selection post-release.
- 1535 3. **Scale matters:** the worse-at-larger- $N$  result implies that releasing large numbers  
1536 of individuals is necessary but not sufficient; releases must also achieve densities  
1537 above the Allee threshold at the local scale to enable reproductive success.

1538 These predictions align with early empirical results from the Sunflower Star Labora-  
1539 tory, whose December 2025 pilot outplanting achieved 98% survival (47 of 48 juveniles)  
1540 over four weeks at Monterey Bay [61]—the same node that shows the highest resilience  
1541 in our simulations.

1542 **9 Discussion**

1543 SSWD-EvoEpi represents, to our knowledge, the first individual-based model to couple  
1544 eco-evolutionary host-pathogen dynamics with sweepstakes reproductive success in a marine  
1545 broadcast spawner. By tracking diploid genotypes at 51 loci across three defense traits (resistance,  
1546 tolerance, recovery) while simultaneously resolving disease transmission, pathogen virulence evolution,  
1547 and spatially explicit metapopulation dynamics, the model provides a framework for evaluating  
1548 conservation interventions that depend on the interplay between ecological and evolutionary processes.  
1549 Here we discuss the principal contributions of this work, its relationship to existing eco-evolutionary  
1550 disease models, key limitations, and priorities for future development.

1552 **9.1 Summary of Contributions**

1553 This study makes four principal contributions:

- 1554 1. **Integrated eco-evolutionary framework for SSWD.** Previous models of SSWD  
1555 dynamics have addressed epidemiology [1], population viability [66], and reintroduction  
1556 epidemiology [4] in isolation. SSWD-EvoEpi integrates these processes, enabling  
1557 the emergent dynamics that arise from feedback loops between disease-driven  
1558 selection, host genetic adaptation, demographic recovery, and pathogen counter-  
1559 adaptation to be studied within a single coherent framework.
- 1560 2. **Three-trait genetic architecture.** Decomposing host defense into resistance (immune  
1561 exclusion), tolerance (damage limitation), and recovery (pathogen clearance)—  
1562 following the conceptual framework of Råberg et al. [54]—reveals that these traits  
1563 evolve at markedly different rates under SSWD selection pressure. Recovery ( $c_i$ )  
1564 emerges as the fastest-evolving trait at every node and population scale (Section 8),  
1565 a prediction that is testable with longitudinal genomic sampling.
- 1566 3. **Comprehensive global sensitivity analysis.** Four rounds of progressive SA  
1567 spanning 47 parameters, up to 23 output metrics, and spatial configurations from 3  
1568 to 11 nodes identify the parameters most influential for model behavior (Section 7).  
1569 The finding that all 47 parameters exhibit nonlinear interactions ( $\sigma/\mu^* > 1.0$ ) est-  
1570ablishes that joint calibration via approximate Bayesian computation is essential,  
1571 and identifies  $\rho_{\text{rec}}$ ,  $k_{\text{growth}}$ ,  $K_{\text{half}}$ ,  $P_{\text{env,max}}$ , and  $n_{\text{resistance}}$  as the highest-priority em-  
1572 pirical targets.
- 1573 4. **Scale-invariant behavioral predictions.** Cross-scale validation from  $K = 5,000$   
1574 to  $K = 100,000$  per node demonstrates that catastrophic population crashes (>97%),  
1575 recovery trait dominance, and the extinction vortex are robust predictions of the  
1576 model, not artifacts of small population sizes (Section 8.3).

1577 **9.2 Comparison with Clement et al. (2024)**

1578 The closest methodological precedent for SSWD-EvoEpi is the eco-evolutionary IBM  
1579 developed by Clement et al. [9] for coevolution between Tasmanian devils (*Sarcophilus*  
1580 *harrisii*) and devil facial tumour disease (DFTD). Both models track individual diploid  
1581 genotypes, couple SEI-type disease dynamics with quantitative genetic evolution, and  
1582 explore the conditions under which evolutionary rescue can avert host extinction follow-  
1583 ing a novel disease introduction. However, several fundamental differences in the study  
1584 systems produce divergent model architectures and predictions.

1585 **Reproductive biology.** Tasmanian devils are iteroparous mammals with deterministic  
1586 reproduction: each female produces a small litter ( $\sim 4$  young) per season, with high  
1587 maternal investment per offspring. *Pycnopodia helianthoides* is a broadcast spawner  
1588 producing  $\sim 10^7$  eggs per female, with fertilization success dependent on gamete encounter  
1589 rates in the water column and subject to Allee effects at low density [43]. SSWD-EvoEpi  
1590 implements sweepstakes reproductive success (SRS) via a Pareto-distributed offspring  
1591 contribution ( $\alpha \approx 1.35$ ), producing  $N_e/N \sim 10^{-3}$  [27]—a reproductive mode with no  
1592 analog in the Clement et al. framework. SRS amplifies genetic drift at the population  
1593 level while simultaneously creating the potential for rapid frequency shifts at individual  
1594 loci when combined with strong selection [14], fundamentally altering the evolutionary  
1595 dynamics compared to a mammalian system.

1596 **Spatial structure.** The Clement et al. model operates on a single well-mixed popu-  
1597 lation, reflecting the relatively continuous distribution of Tasmanian devils across Tas-  
1598 mania. SSWD-EvoEpi represents the NE Pacific range of *Pycnopodia helianthoides* as a  
1599 metapopulation network of up to 150 discrete habitat nodes connected by larval disper-  
1600 sal and waterborne pathogen transport. This spatial complexity introduces dispersal–  
1601 selection interactions that are absent in the single-population case: local adaptation  
1602 can proceed at different rates across nodes (as observed in the differential recovery at  
1603 Monterey; Section 8.1), and larval exchange can either homogenize or maintain genetic  
1604 differentiation depending on the balance of gene flow and spatially heterogeneous selec-  
1605 tion.

1606 **Pathogen evolution.** Clement et al. model DFTD as a clonally transmitted cancer  
1607 whose evolution follows a phenotypic difference model, with host resistance and tumor  
1608 growth rate coevolving along continuous trait axes. Their key finding—that coevolution  
1609 enables host persistence over 50 generations—relies on the tumor’s capacity to evolve re-  
1610 duced virulence in response to host resistance. SSWD-EvoEpi implements pathogen evo-  
1611 lution through a heritable virulence phenotype that scales shedding rate, host mortality

rate, and disease progression along mechanistic tradeoff curves (Section 7). The qualitative prediction differs: in our model, the environmental pathogen reservoir ( $P_{\text{env}}$ ) decouples pathogen fitness from individual host survival, weakening the virulence–transmission tradeoff that drives attenuation in the Clement et al. framework and potentially preventing the coevolutionary stabilization that enables devil persistence.

**Evolutionary rescue prospects.** Clement et al. found a high probability of devil persistence over 50 generations (~150 years for devils), driven by rapid coevolutionary dynamics. Our model produces a starkly different prediction: no recovery to >5% of carrying capacity within 20 years (~4 *Pycnopodia helianthoides* generations) at any node or population scale. This contrast likely reflects the fundamental mismatch between *Pycnopodia helianthoides*’s long generation time (~5 years vs. ~3 years for devils), the extreme variance in reproductive success under SRS (which reduces the efficacy of selection relative to drift), and the environmental pathogen reservoir that maintains infection pressure independently of the host population’s genetic composition.

### 9.3 The Environmental Pathogen Reservoir as a Multi-Species Abstraction

The environmental pathogen concentration  $P_{\text{env}}$  is the most conceptually novel—and most empirically unconstrained—element of the SSWD-EvoEpi disease module. Rather than explicitly modeling *V. pectenicida* dynamics in non-*Pycnopodia helianthoides* host species,  $P_{\text{env}}$  serves as an aggregate abstraction for all pathogen sources external to the focal *Pycnopodia helianthoides* population: other asteroid species, marine sediment reservoirs, and environmental bacteria. This design choice was motivated by two considerations.

First, the multi-species nature of the 2013–2015 SSWD pandemic, which affected >20 asteroid species [34, 49], implies that *V. pectenicida* (or closely related Vibrio strains) can persist in the environment independently of any single host species. Hewson [30] demonstrated explosive *V. pectenicida* growth in the presence of decaying echinoderm tissue, suggesting a saprophytic lifestyle that can sustain environmental pathogen pools even when live *Pycnopodia helianthoides* are absent. The fjord refuge mechanism identified by Gehman et al. [17]—where reduced salinity and temperature suppress Vibrio growth—operates at the community level, further supporting a spatially varying environmental reservoir.

Second, explicitly modeling multi-species SSWD dynamics would require parameterizing disease susceptibility, shedding rates, and population dynamics for >20 additional asteroid species, most of which lack even basic demographic data. The  $P_{\text{env}}$  abstraction captures the functional consequence (sustained pathogen pressure at the community

1648 level) without requiring species-specific parameterization.

1649 However, this abstraction comes at a cost. The sensitivity analysis reveals that  $P_{\text{env},\text{max}}$   
1650 is the 4th most influential parameter globally and the most influential parameter for the  
1651 fjord protection metric (Section 7.3). Its interaction ratio ( $\sigma/\mu^* = 1.92$ ) indicates strong  
1652 nonlinear coupling with other parameters, meaning that uncertainty in  $P_{\text{env}}$  propagates  
1653 broadly through the model. Calibrating  $P_{\text{env}}$  against field data (e.g., environmental Vibrio  
1654 concentrations in *Pycnopodia helianthoides* habitat, disease prevalence in non-*Pycnopodia*  
1655 *helianthoides* asteroids) is a high priority for constraining model predictions.

## 1656 9.4 Conservation Implications

### 1657 9.4.1 Evolutionary Rescue Is Too Slow

1658 The central finding of both the validation and sensitivity analyses is that natural selec-  
1659 tion on polygenic resistance cannot drive population recovery on conservation-relevant  
1660 timescales. At  $K = 100,000$  per node, resistance trait scores actually *decline* over 20  
1661 years (mean  $\Delta r_i = -0.005$ ; Table 14), and even the fastest-evolving trait (recovery,  
1662  $\Delta c_i \approx +0.06$ ) produces daily clearance probabilities of only 0.35–0.45%, far below what  
1663 is needed to substantially reduce disease mortality. This finding is consistent with evo-  
1664 lutionary rescue theory, which predicts that rescue requires standing genetic variance  
1665  $\times$  selection intensity to exceed the rate of population decline [10]. For *Pycnopodia he-*  
1666 *lianthesoides*, the mismatch is severe: generation times of  $\sim 5$  years versus crash timescales  
1667 of  $\sim 2$  years mean that <1 generation of selection can act before populations enter the  
1668 extinction vortex.

1669 This result has a direct conservation implication: **waiting for natural evolution**  
1670 **is not a viable recovery strategy**. Active intervention through captive breeding and  
1671 managed release is essential to prevent functional extinction. The AZA SAFE program’s  
1672 existing captive population of  $>2,500$  juveniles and 130+ reproductive adults [5], com-  
1673 bined with the successful December 2025 pilot outplanting at Monterey [64], provides the  
1674 demographic foundation for such intervention.

### 1675 9.4.2 Recovery Trait as a Breeding Target

1676 The model’s prediction that recovery ( $c_i$ ) evolves 7–13× faster than resistance ( $r_i$ ) sug-  
1677 gests a specific strategy for captive breeding programs: selecting for pathogen clearance  
1678 ability rather than infection prevention. If *Pycnopodia helianthoides* recovery ability has  
1679 a heritable genetic basis—as implied by the strong fitness gradient on  $c_i$  in the model—  
1680 then challenge experiments in captive facilities could identify high-clearance individuals  
1681 for preferential breeding. The Pycnopodia reference genome [60] enables genome-wide  
1682 association studies to identify the genomic basis of clearance variation.

1683 **9.4.3 Release Site Selection**

1684 The consistent identification of Monterey as the most resilient node—with the lowest  
1685 crash percentage (97.1% at  $K = 100,000$ ), highest recovery count, and strongest recovery  
1686 trait evolution—reflects an emergent property of warmer temperatures driving stronger  
1687 selection for clearance. This suggests that southern sites may be preferable for initial  
1688 releases if the goal is to establish self-sustaining populations with elevated disease resis-  
1689 tance. However, warmer temperatures also increase disease pressure, creating a tension  
1690 between maximizing selective benefit and minimizing initial mortality. The planned con-  
1691 servation module (Section 9.6) will enable explicit optimization of release timing, location,  
1692 and genetic composition.

1693 **9.5 Model Limitations**

1694 We identify five principal limitations of the current model:

1695 **1. No multi-species dynamics.** SSWD-EvoEpi focuses exclusively on *Pycnopodia*  
1696 *helianthoides*, abstracting all community-level interactions into the  $P_{\text{env}}$  term. This ex-  
1697 cludes potential competitive release of sea urchins following *Pycnopodia helianthoides*  
1698 decline [15, 55], cross-species transmission dynamics [49], and the possibility that recov-  
1699 ery of *Pycnopodia helianthoides* could itself alter the selective environment for disease.  
1700 The trophic cascade from *Pycnopodia helianthoides* loss to urchin proliferation to kelp  
1701 deforestation [48] represents a feedback loop that could modify habitat quality and, con-  
1702 sequently, sea star survival, but is not represented.

1703 **2. Environmental pathogen reservoir is unconstrained.**  $P_{\text{env,max}}$  ranks 4th in  
1704 global sensitivity yet has no empirical calibration target. Field measurements of water-  
1705 borne *V. pectenicia* concentrations in *Pycnopodia helianthoides* habitat are needed to  
1706 constrain this parameter. Until such data are available, model predictions about the  
1707 feasibility of local disease elimination via host removal or habitat management should be  
1708 treated as exploratory.

1709 **3. 47-parameter model with universal nonlinearity.** The SA reveals that all 47  
1710 parameters interact nonlinearly ( $\sigma/\mu^* > 1.0$  for every parameter; Section 7.3.4). While  
1711 this is a realistic property of complex biological systems, it means that the model can-  
1712 not be calibrated by tuning individual parameters in isolation. Joint calibration via  
1713 ABC-SMC [57] is computationally expensive ( $>10^4$  model evaluations) and requires well-  
1714 defined summary statistics and calibration targets, many of which are currently lacking  
1715 for *Pycnopodia helianthoides*.

1716 **4. Recovery rate has zero empirical basis.** The base recovery rate  $\rho_{\text{rec}}$  is the single  
1717 most influential parameter in the model (Section 7.3.1), yet whether *Pycnopodia helianthoides*  
1718 can clear *V. pectenida* infections at all is unknown. The SA finding that  
1719  $\rho_{\text{rec}}$  explains more output variance than any other parameter underscores this as the  
1720 highest-priority empirical gap. Challenge-recovery experiments in captive *Pycnopodia*  
1721 *helianthoides* [53] could provide direct estimates of clearance probability as a function of  
1722 dose, temperature, and individual genotype.

1723 **5. Spatial resolution.** The validation runs use 5–11 nodes, far below the 150+ nodes  
1724 needed to represent the full NE Pacific range of *Pycnopodia helianthoides* at ecologically  
1725 meaningful resolution. Scaling analysis (Section 7.1) confirms computational feasibility  
1726 ( $\sim 72$  s for 75,000 agents, 150 nodes), but the reduced-node configurations used here may  
1727 underestimate the importance of spatial heterogeneity, as demonstrated by the dramatic  
1728 rank gains of spatial parameters between R3 (3 nodes) and R4 (11 nodes).

## 1729 9.6 Future Directions

### 1730 9.6.1 ABC-SMC Calibration

1731 The immediate next step is formal calibration using approximate Bayesian computation  
1732 with sequential Monte Carlo sampling (ABC-SMC). Summary statistics will include:  
1733 (i) range-wide population decline (>90% crash within 2 years of disease introduction),  
1734 (ii) latitudinal mortality gradient [23], (iii) fjord protection effect [17], (iv) allele frequency  
1735 shifts at outlier loci [58], and (v) disease progression timelines from challenge experiments  
1736 [53]. The R4 SA results (Table 12) provide a natural prioritization: the top 10–15  
1737 parameters can be calibrated jointly while fixing the remaining 32–37 at their default  
1738 values with minimal loss of model fidelity.

### 1739 9.6.2 Conservation Scenario Evaluation

1740 A conservation module is under development to simulate specific management interventions:  
1741

- 1742 • Captive-bred release: number, timing, location, and genetic composition of released  
1743 cohorts, parameterized from AZA SAFE protocols [5];
- 1744 • Assisted gene flow: introduction of cryopreserved gametes from genetically diverse  
1745 wild-caught founders [22];
- 1746 • Marine protected areas: local reduction of environmental stressors that may interact  
1747 with disease susceptibility.

<sup>1748</sup> The December 2025 Monterey outplanting data [64] will provide the first empirical vali-  
<sup>1749</sup> dation target for captive-bred survival post-release.

### <sup>1750</sup> 9.6.3 Full Coastline Network

<sup>1751</sup> Expanding the spatial network to 150 nodes spanning the full NE Pacific range of *Pyc-  
1752 nopodia helianthoides* (Baja California to the Aleutian Islands) will test whether the  
1753 patterns identified at 5–11 nodes—the north–south mortality gradient, fjord protection,  
1754 Monterey resilience—scale to the full metapopulation. The overwater distance matrix for  
1755 489 candidate sites has been computed (Section 6), and computational scaling analysis  
1756 confirms feasibility ( $\sim 66$  s for 150 nodes; Section 7.1).

### <sup>1757</sup> 9.6.4 Integration with Empirical Data

<sup>1758</sup> The publication of the *Pycnopodia helianthoides* reference genome [60] enables future  
1759 GWAS to identify resistance-, tolerance-, and recovery-associated loci, providing direct  
1760 calibration targets for the genetic architecture parameters ( $n_{\text{resistance}}$ ,  $n_{\text{tolerance}}$ ,  $n_{\text{recovery}}$ ,  
1761 trait-specific effect size distributions). The Koch’s-postulates confirmation of *V. pecteni-  
1762 cida* as the causative agent [53] opens the door to controlled challenge experiments that  
1763 can estimate dose-dependent infection probability, stage-specific duration, recovery rate,  
1764 and temperature sensitivity—the parameters that the SA identifies as most influential.  
1765 Combining these empirical constraints with ABC-SMC calibration will substantially re-  
1766 duce parametric uncertainty and increase confidence in conservation scenario predictions.

## <sup>1767</sup> 9.7 Conclusions

<sup>1768</sup> SSWD-EvoEpi provides a comprehensive computational framework for exploring the eco-  
1769 evolutionary dynamics of SSWD in *Pycnopodia helianthoides*. The model reveals that  
1770 evolutionary rescue through natural selection on polygenic resistance is insufficient to  
1771 prevent population collapse on conservation timescales, that pathogen clearance (recov-  
1772 ery) rather than infection prevention (resistance) is the primary adaptive pathway, and  
1773 that the extinction vortex persists at ecologically realistic population sizes. These find-  
1774 ings reinforce the scientific case for captive breeding and managed release as the essential  
1775 conservation strategy for this critically endangered species. The four-round sensitivity  
1776 analysis establishes clear priorities for empirical research—recovery rate, environmental  
1777 pathogen pressure, genetic architecture, and growth rate—that will enable formal model  
1778 calibration and, ultimately, quantitative predictions for guiding *Pycnopodia helianthoides*  
1779 recovery efforts across the northeastern Pacific.

1780 **References**

- 1781 [1] Emilius A. Aalto, Kevin D. Lafferty, Susanne H. Sokolow, Richard E. Grewelle,  
1782 Tal Ben-Horin, Charles A. Boch, Peter T. Raimondi, Steven J. Bograd, Elliott L.  
1783 Hazen, Michael G. Jacox, Fiorenza Micheli, and Giulio A. De Leo. Models with  
1784 environmental drivers offer a plausible mechanism for the rapid spread of infectious  
1785 disease outbreaks in marine organisms. *Scientific Reports*, 10:5975, 2020. doi: 10.  
1786 1038/s41598-020-62118-4.
- 1787 [2] Citlalli A. Aquino, Ryan M. Besemer, Christopher M. DeRito, Jan Kocian, Ian R.  
1788 Porter, Peter T. Raiber, John E. Episale, and Ian Hewson. Evidence that microor-  
1789 ganisms at the animal-water interface drive sea star wasting disease. *Frontiers in*  
1790 *Microbiology*, 11:610009, 2021. doi: 10.3389/fmicb.2020.610009.
- 1791 [3] Einar Árnason, Jere Koskela, Katrín Halldórsdóttir, and Bjarki Eldon. Sweepstakes  
1792 reproductive success via pervasive and recurrent selective sweeps. *eLife*, 12:e80781,  
1793 2023. doi: 10.7554/eLife.80781.
- 1794 [4] Jorge Arroyo-Esquivel, Alyssa Gehman, Katie Collins, and Fernanda Sanchez. Man-  
1795 aging populations after a disease outbreak: exploration of epidemiological con-  
1796 sequences of managed host reintroduction following disease-driven host decline.  
1797 *bioRxiv*, 2025. doi: 10.1101/2025.02.28.640833.
- 1798 [5] AZA SAFE. Sunflower sea star program plan 2024–2027. Technical report, Associa-  
1799 tion of Zoos and Aquariums, 2024.
- 1800 [6] Jenn M. Burt, M. Tim Tinker, Daniel K. Okamoto, Kyle W. Demes, Katie Holmes,  
1801 and Anne K. Salomon. Sudden collapse of a mesopredator reveals its complementary  
1802 role in mediating rocky reef regime shifts. *Proceedings of the Royal Society B*, 285:  
1803 20180553, 2018. doi: 10.1098/rspb.2018.0553.
- 1804 [7] California Ocean Protection Council. Staff recommendation item 9: Consideration  
1805 and approval of disbursement of funds to support sunflower sea star reintroduction.  
1806 Technical report, California Ocean Protection Council, 2025.
- 1807 [8] Francesca Campolongo, Jessica Cariboni, and Andrea Saltelli. An effective screening  
1808 design for sensitivity analysis of large models. *Environmental Modelling & Software*,  
1809 22(10):1509–1518, 2007. doi: 10.1016/j.envsoft.2006.10.004.
- 1810 [9] Matthew Clement, Rodrigo Hamede, Menna E. Jones, and Paul A. Hohenlohe.  
1811 Coevolution enables host persistence in an eco-evolutionary epidemiological model  
1812 of Tasmanian devil facial tumor disease. *Evolution*, 78(12):2095–2110, 2024. doi:  
1813 10.1093/evolut/qpae143.

- 1814 [10] Matthew Clement et al. Eco-evolutionary individual-based model for coevolution  
1815 between Tasmanian devils and devil facial tumour disease. *Evolution*, 2024. doi:  
1816 10.1093/evolut/qpae143.
- 1817 [11] Donald L. DeAngelis and Wolf M. Mooij. Individual-based modeling of ecological  
1818 and evolutionary processes. *Annual Review of Ecology, Evolution, and Systematics*,  
1819 36:147–168, 2005. doi: 10.1146/annurev.ecolsys.36.102003.152644.
- 1820 [12] Michael L. Dungan, Thomas E. Miller, and Donald A. Thomson. Catastrophic  
1821 decline of a top carnivore in the Gulf of California rocky intertidal zone. *Science*,  
1822 216:989–991, 1982. doi: 10.1126/science.216.4549.989.
- 1823 [13] Morgan E. Eisenlord, Maya L. Groner, Robin M. Yoshioka, Jennifer Elliott, Jeffrey  
1824 Maynard, Steven Fradkin, Margaret Turner, Katie Pyne, Sandy Wyllie-Echeverria,  
1825 Benjamin G. Miner, and C. Drew Harvell. Ochre star mortality during the 2014  
1826 wasting disease epizootic: role of population size and temperature. *Philosophical  
1827 Transactions of the Royal Society B*, 371(1689):20150212, 2016. doi: 10.1098/rstb.  
1828 2015.0212.
- 1829 [14] Bjarki Eldon and Wolfgang Stephan. Sweepstakes reproduction facilitates rapid  
1830 adaptation in highly fecund populations. *Molecular Ecology*, 33:e16903, 2024. doi:  
1831 10.1111/mec.16903.
- 1832 [15] Aaron W. E. Galloway, Sarah A. Gravem, Jenna N. Kobelt, et al. Sunflower sea  
1833 star predation on urchins can facilitate kelp forest recovery. *Proceedings of the Royal  
1834 Society B*, 290:20221897, 2023. doi: 10.1098/rspb.2022.1897.
- 1835 [16] Joanna C. Gascoigne and Romuald N. Lipcius. Allee effects in marine systems.  
1836 *Marine Ecology Progress Series*, 269:49–59, 2004. doi: 10.3354/meps269049.
- 1837 [17] Alyssa-Lois M. Gehman, Olivier Pontier, Tanya Froese, Derek VanMaanen, Tris-  
1838 tan Blaine, Gillian Sadlier-Brown, Alexis M. Olson, Zachary L. Monteith, Kite-  
1839 ria Bachen, Christy Prentice, Margot Hessing-Lewis, and Jennifer M. Jackson.  
1840 Fjord oceanographic dynamics provide refuge for critically endangered *Pycnopo-*  
1841 *dia helianthoides*. *Proceedings of the Royal Society B*, 292:20242770, 2025. doi:  
1842 10.1098/rspb.2024.2770.
- 1843 [18] Àlex Giménez-Romero, Antoni Grau, Iris E. Hendriks, and Manuel A. Matías. Mod-  
1844 elling parasite-produced marine diseases: The case of the mass mortality event of  
1845 *Pinna nobilis*. *Ecological Modelling*, 459:109740, 2021. doi: 10.1016/j.ecolmodel.  
1846 2021.109740.

- 1847 [19] Sarah A. Gravem and Bruce A. Menge. Metapopulation-scale resilience to disease-  
1848 induced mass mortality in a keystone predator: From stasis to instability. *Ecosphere*,  
1849 16:e70426, 2025. doi: 10.1002/ecs2.70426.
- 1850 [20] Sarah A. Gravem, Walter N. Heady, Vienna R. Saccomanno, Kathleen F. Alvstad,  
1851 Alyssa-Lois M. Gehman, Taylor N. Frierson, and Scott L. Hamilton. *Pycnopodia*  
1852 *helianthoides*. *The IUCN Red List of Threatened Species*, 2021. doi: 10.2305/IUCN.  
1853 UK.2021-1.RLTS.T178290276A197818455.en.
- 1854 [21] Volker Grimm and Steven F. Railsback. *Individual-Based Modeling and Ecology*.  
1855 Princeton University Press, Princeton, NJ, 2005.
- 1856 [22] Mary Hagedorn et al. Assisted gene flow using cryopreserved sperm in critically en-  
1857 dangered coral. *Proceedings of the National Academy of Sciences*, 118:e2110559118,  
1858 2021. doi: 10.1073/pnas.2110559118.
- 1859 [23] Scott L. Hamilton et al. Disease-driven mass mortality event leads to widespread  
1860 extirpation and variable recovery potential of a marine predator across the eastern  
1861 Pacific. *Proceedings of the Royal Society B*, 288:20211195, 2021. doi: 10.1098/rspb.  
1862 2021.1195.
- 1863 [24] C. Drew Harvell, Diego Montecino-Latorre, Joseph M. Caldwell, Jenn M. Burt,  
1864 Kathryn Bosley, et al. Disease epidemic and a marine heat wave are associated  
1865 with the continental-scale collapse of a pivotal predator (*Pycnopodia helianthoides*).  
1866 *Science Advances*, 5:eaau7042, 2019. doi: 10.1126/sciadv.aau7042.
- 1867 [25] C. Drew Harvell, Diego Montecino-Latorre, Joseph M. Caldwell, Jenn M. Burt,  
1868 Kathryn Bosley, et al. Disease epidemic and a marine heat wave are associated  
1869 with the continental-scale collapse of a pivotal predator (*Pycnopodia helianthoides*).  
1870 *Science Advances*, 5:eaau7042, 2019. doi: 10.1126/sciadv.aau7042.
- 1871 [26] Walter N. Heady, Rodrigo Beas-Luna, Michael N. Dawson, et al. Roadmap to re-  
1872 covery for the sunflower sea star along the West Coast of North America. Technical  
1873 report, The Nature Conservancy, 2022.
- 1874 [27] Dennis Hedgecock and Alexander I. Pudovkin. Sweepstakes reproductive success  
1875 in highly fecund marine fish and shellfish: A review and commentary. *Bulletin of*  
1876 *Marine Science*, 87:971–1002, 2011. doi: 10.5343/bms.2010.1051.
- 1877 [28] Jon Herman and Will Usher. SALib: An open-source Python library for sensitivity  
1878 analysis. *Journal of Open Source Software*, 2(9):97, 2017. doi: 10.21105/joss.00097.

- 1879 [29] Ian Hewson. Microbial respiration in the asteroid diffusive boundary layer influenced  
1880 sea star wasting disease during the 2013–2014 northeast Pacific Ocean mass mortality  
1881 event. *Marine Ecology Progress Series*, 668:231–237, 2021. doi: 10.3354/meps13710.
- 1882 [30] Ian Hewson. When bacteria meet many arms: Autecological insights into *Vibrio*  
1883 *pectenicida* FHCF-3 in echinoderms. *bioRxiv*, 2025. doi: 10.1101/2025.08.15.670479.
- 1884 [31] Ian Hewson, Jason B. Button, Brent M. Gudenkauf, et al. Densovirus associated with  
1885 sea-star wasting disease and mass mortality. *Proceedings of the National Academy of*  
1886 *Sciences*, 111:17278–17283, 2014. doi: 10.1073/pnas.1416625111.
- 1887 [32] Ian Hewson, Morgan R. Johnson, and Benjamin Reyes-Chavez. Lessons learned  
1888 from the sea star wasting disease investigation. *Annual Review of Marine Science*,  
1889 17:257–279, 2025. doi: 10.1146/annurev-marine-040623-082617.
- 1890 [33] Ian Hewson et al. Investigating the complex association between viral ecology, envi-  
1891 ronment, and Northeast Pacific sea star wasting. *Frontiers in Marine Science*, 5:77,  
1892 2018. doi: 10.3389/fmars.2018.00077.
- 1893 [34] Ian Hewson et al. Perspective: Something old, something new? Review of wasting  
1894 and other mortality in Asteroidea (Echinodermata). *Frontiers in Marine Science*, 6:  
1895 406, 2019. doi: 10.3389/fmars.2019.00406.
- 1896 [35] Jason Hodin, Amanda Pearson-Lund, Freya P. Anteau, Philippe Kitaeff, and Sarah  
1897 Cefalu. Progress toward complete life-cycle culturing of the endangered sunflower  
1898 star, *Pycnopodia helianthoides*. *Biological Bulletin*, 241:243–258, 2021. doi: 10.1086/  
1899 716552.
- 1900 [36] Ilse Höllinger, Pleuni S. Pennings, and Joachim Hermissen. Polygenic adaptation:  
1901 From sweeps to subtle frequency shifts. *eLife*, 11:e66697, 2022. doi: 10.7554/eLife.  
1902 66697.
- 1903 [37] Matthew C. Kay and Richard B. Emlet. Laboratory spawning, larval development,  
1904 and metamorphosis of the lace coral *Stylaster roseus*. *Invertebrate Biology*, 121:  
1905 325–338, 2002. Movement speed reference for *Pycnopodia*: 0.5 m/min.
- 1906 [38] C. Lambert, J.-L. Nicolas, V. Cilia, and S. Corre. *Vibrio pectenicida* sp. nov., a  
1907 pathogen of scallop (*Pecten maximus*) larvae. *International Journal of Systematic*  
1908 *Bacteriology*, 48:481–487, 1998. doi: 10.1099/00207713-48-2-481.
- 1909 [39] Ryan E. Langendorf, James A. Estes, James C. Watson, Michael C. Kenner, Brian B.  
1910 Hatfield, M. Tim Tinker, Elizabeth Waddle, Michelle L. DeMarch, and Daniel F.  
1911 Doak. Dynamic and context-dependent keystone species effects in kelp forests. *Pro-*  
1912 *ceedings of the National Academy of Sciences*, 2025. doi: 10.1073/pnas.XXXXXXXX.

- 1913 [40] Harilaos A. Lessios. The great *Diadema antillarum* die-off: 30 years  
1914 later. *Annual Review of Marine Science*, 8:267–283, 2016. doi: 10.1146/  
1915 annurev-marine-122414-033857.
- 1916 [41] Katie E. Lotterhos and Michael C. Whitlock. The relative power of genome scans to  
1917 detect local adaptation depends on sampling design and statistical method. *Molec-*  
1918 *ular Ecology*, 24(5):1031–1046, 2015. doi: 10.1111/mec.13100.
- 1919 [42] Dayv Lowry, Sarah Wright, Melissa Neuman, et al. Endangered Species Act status  
1920 review report: Sunflower sea star (*Pycnopodia helianthoides*). Technical report,  
1921 NOAA National Marine Fisheries Service, 2022.
- 1922 [43] Carolyn J. Lundquist and Louis W. Botsford. Model projections of the fishery  
1923 implications of the Allee effect in broadcast spawners. *Ecological Applications*, 14:  
1924 929–941, 2004. doi: 10.1890/02-5325.
- 1925 [44] Coralie Lupo, Pedro J. Cabello-Yeves, Sara Ferreira, Julien de Lorgeril, and Luigi  
1926 Vezzulli. Vibrio ecology, pathogenesis, and evolution. *Frontiers in Microbiology*, 11:  
1927 587685, 2020. doi: 10.3389/fmicb.2020.587685.
- 1928 [45] Coralie Lupo et al. Spatial epidemiological modelling of infection by *Vibrio aestuari-*  
1929 *anus* shows that connectivity and temperature control oyster mortality. *Aquaculture*  
1930 *Environment Interactions*, 12:511–527, 2020. doi: 10.3354/aei00379.
- 1931 [46] Michael Lynch. Evolution of the mutation rate. *Trends in Genetics*, 26:345–352,  
1932 2010. doi: 10.1016/j.tig.2010.05.003.
- 1933 [47] Ryan T. Mancuso, Sarah A. Gravem, Rachel S. Campbell, Nathan Hunter, Pete  
1934 Raimondi, Aaron W. E. Galloway, and Kristy J. Kroeker. Sunflower sea star chemical  
1935 cues locally reduce kelp consumption by eliciting a flee response in red sea urchins.  
1936 *Proceedings of the Royal Society B*, 2025. doi: 10.1098/rspb.2025.0949.
- 1937 [48] Zofia D. Meunier, Sally D. Hacker, and Bruce A. Menge. Regime shifts in rocky  
1938 intertidal communities associated with a marine heatwave and disease outbreak.  
1939 *Nature Ecology & Evolution*, 8:1285–1297, 2024. doi: 10.1038/s41559-024-02425-5.
- 1940 [49] C. Melissa Miner, Jennifer L. Burnaford, Richard F. Ambrose, Liam Antrim, et al.  
1941 Large-scale impacts of sea star wasting disease (SSWD) on intertidal sea stars and  
1942 implications for recovery. *PLoS ONE*, 13:e0192870, 2018. doi: 10.1371/journal.pone.  
1943 0192870.
- 1944 [50] Diego Montecino-Latorre, Morgan E. Eisenlord, Morgan Turner, Reyn Yoshioka,  
1945 C. Drew Harvell, et al. Devastating transboundary impacts of sea star wasting

- 1946 disease on subtidal asteroids. *PLoS ONE*, 11:e0163190, 2016. doi: 10.1371/journal.  
1947 pone.0163190.
- 1948 [51] Diego Montecino-Latorre, Morgan E. Eisenlord, Morgan Turner, Reyn Yoshioka,  
1949 C. Drew Harvell, et al. Devastating transboundary impacts of sea star wasting  
1950 disease on subtidal asteroids. *PLoS ONE*, 11:e0163190, 2016. doi: 10.1371/journal.  
1951 pone.0163190.
- 1952 [52] Max D. Morris. Factorial sampling plans for preliminary computational experiments.  
1953 *Technometrics*, 33(2):161–174, 1991. doi: 10.1080/00401706.1991.10484804.
- 1954 [53] Maya B. Prentice, Citlalli A. Aquino, Amy M. Chan, Kalia M. Davis, Paul K. Her-  
1955 shberger, Jan F. Finke, Jason Hodin, Aquiala McCracken, Christina T. E. Kellogg,  
1956 Rute B. G. Clemente-Carvalho, Christy Prentice, Kiana X. Zhong, C. Drew Harvell,  
1957 Curtis A. Suttle, and Alyssa-Lois M. Gehman. *Vibrio pectenicida* strain FHCF-3 is  
1958 a causative agent of sea star wasting disease. *Nature Ecology & Evolution*, 2025. doi:  
1959 10.1038/s41559-025-02797-2.
- 1960 [54] Lars Råberg, Andrea L. Graham, and Andrew F. Read. Decomposing health: toler-  
1961 ance and resistance to parasites in animals. *Philosophical Transactions of the Royal  
1962 Society B*, 364(1513):37–49, 2009. doi: 10.1098/rstb.2008.0184.
- 1963 [55] Laura Rogers-Bennett and Cynthia A. Catton. Marine heat wave and multiple  
1964 stressors tip bull kelp forest to sea urchin barrens. *Scientific Reports*, 9:15050, 2019.  
1965 doi: 10.1038/s41598-019-51114-y.
- 1966 [56] Andrea Saltelli. Making best use of model evaluations to compute sensitivity in-  
1967 dices. *Computer Physics Communications*, 145(2):280–297, 2002. doi: 10.1016/  
1968 S0010-4655(02)00280-1.
- 1969 [57] Andrea Saltelli, Marco Ratto, Terry Andres, Francesca Campolongo, Jessica Cari-  
1970 boni, Debora Gatelli, Michaela Saisana, and Stefano Tarantola. *Global Sensitivity  
1971 Analysis: The Primer*. John Wiley & Sons, 2008. doi: 10.1002/9780470725184.
- 1972 [58] Lauren M. Schiebelhut, Jonathan B. Puritz, and Michael N. Dawson. Decimation  
1973 by sea star wasting disease and rapid genetic change in a keystone species, *Pisaster  
1974 ochraceus*. *Proceedings of the National Academy of Sciences*, 115:7069–7074, 2018.  
1975 doi: 10.1073/pnas.1800285115.
- 1976 [59] Lauren M. Schiebelhut, Jonathan B. Puritz, and Michael N. Dawson. Decimation  
1977 by sea star wasting disease and rapid genetic change in a keystone species, *Pisaster  
1978 ochraceus*. *Proceedings of the National Academy of Sciences*, 115(27):7069–7074,  
1979 2018. doi: 10.1073/pnas.1800285115.

- 1980 [60] Lauren M. Schiebelhut et al. A reference genome for ecological restoration of the  
1981 sunflower sea star, *Pycnopodia helianthoides*. *Journal of Heredity*, 115:86–93, 2024.  
1982 doi: 10.1093/jhered/esad054.
- 1983 [61] Sea Star Lab. Sea star cryopreservation breakthrough inspires hope for sunflower  
1984 stars, 2025. Press release.
- 1985 [62] Il'ya M. Sobol'. Global sensitivity indices for nonlinear mathematical models and  
1986 their Monte Carlo estimates. *Mathematics and Computers in Simulation*, 55(1–3):  
1987 271–280, 2001. doi: 10.1016/S0378-4754(00)00270-6.
- 1988 [63] Megumi F. Strathmann. *Reproduction and Development of Marine Invertebrates of*  
1989 *the Northern Pacific Coast*. University of Washington Press, Seattle, 1987.
- 1990 [64] Sunflower Star Lab. First-ever temporary experimental outplanting of sunflower  
1991 stars in California, 2025. Press release.
- 1992 [65] Stephen E. Swearer, Jeffrey S. Shima, Michael E. Hellberg, Simon R. Thorrold,  
1993 Geoffrey P. Jones, D. Ross Robertson, Steven G. Morgan, Kimberly A. Selkoe, Gre-  
1994 gory M. Ruiz, and Robert R. Warner. Evidence of self-recruitment in demersal  
1995 marine populations. *Bulletin of Marine Science*, 70:251–271, 2002.
- 1996 [66] Nick Tolimieri. Appendix A: Population viability analysis of *Pycnopodia he-*  
1997 *lianthesoides*. In: Lowry et al., *ESA Status Review Report*, NOAA NMFS, 2022.
- 1998 [67] David L. J. Vendrami, Lloyd S. Peck, Melody S. Clark, Bjarki Eldon, Michael Mered-  
1999 ith, and Joseph I. Hoffman. Sweepstake reproductive success and collective dispersal  
2000 produce chaotic genetic patchiness in a broadcast spawner. *Science Advances*, 7:  
2001 eabj4713, 2021. doi: 10.1126/sciadv.abj4713.
- 2002 [68] John P. Wares and Lauren M. Schiebelhut. What doesn't kill them makes them  
2003 stronger: an association between elongation factor 1- $\alpha$  overdominance in the sea  
2004 star *Pisaster ochraceus* and "sea star wasting disease". *PeerJ*, 4:e1876, 2016. doi:  
2005 10.7717/peerj.1876.
- 2006 [69] Helen J. Wearing, Pejman Rohani, and Matt J. Keeling. Appropriate models for the  
2007 management of infectious diseases. *PLoS Medicine*, 2(7):e174, 2005. doi: 10.1371/  
2008 journal.pmed.0020174.

## 2009 A Parameter Tables

2010 Table 16–21 list all 47 parameters included in the sensitivity analysis, grouped by module.  
2011 For each parameter we report the default value used in validation runs, the sensitivity

<sup>2012</sup> analysis range (low–high), the distribution used for sampling (U = uniform, LU = log-  
<sup>2013</sup> uniform, D = discrete), and the empirical confidence rating: ★★★ = directly measured,  
<sup>2014</sup> ★★ = constrained by related data, ★ = poorly constrained or assumed.

Table 16: Disease module parameters (16). Default values from `config.py`; SA ranges from `param_spec.py`.

Parameter	Description	Default	Range	Dist.	Conf.
$a_{\text{exposure}}$	Exposure rate ( $\text{d}^{-1}$ )	0.75	[0.30, 1.50]	U	*
$K_{\text{half}}$	Half-infective dose (bact/mL)	87,000	[ $2 \times 10^4$ , $2 \times 10^5$ ]	LU	*
$\sigma_{1,\text{eff}}$	$I_1$ shedding rate (field-effective)	5.0	[1.0, 25.0]	LU	*
$\sigma_{2,\text{eff}}$	$I_2$ shedding rate (field-effective)	50.0	[10.0, 250.0]	LU	*
$\sigma_D$	Saprophytic burst (field-effective)	15.0	[3.0, 75.0]	LU	*
$\rho_{\text{rec}}$	Recovery rate ( $\text{d}^{-1}$ )	0.05	[0.0, 0.20]	U	*
$\mu_{E \rightarrow I_1, \text{ref}}$	$E \rightarrow I_1$ progression at $T_{\text{ref}}$	0.57	[0.20, 1.00]	U	**
$\mu_{I_1 \rightarrow I_2, \text{ref}}$	$I_1 \rightarrow I_2$ progression at $T_{\text{ref}}$	0.40	[0.15, 0.80]	U	**
$\mu_{I_2 \rightarrow D, \text{ref}}$	$I_2 \rightarrow$ Death rate at $T_{\text{ref}}$	0.173	[0.08, 0.35]	U	**
$P_{\text{env,max}}$	Background Vibrio input (bact/mL/d)	500.0	[50.0, 5,000.0]	LU	*
$T_{\text{ref}}$	$V. pectenicida$ temperature optimum ( $^{\circ}\text{C}$ )	20.0	[17.0, 23.0]	U	**
$T_{\text{VBNC}}$	VBNC midpoint temperature ( $^{\circ}\text{C}$ )	12.0	[8.0, 15.0]	U	**
$s_{\text{min}}$	Salinity minimum for Vibrio (psu)	10.0	[5.0, 15.0]	U	**

*Continued*

Table 16 (continued)

Parameter	Description	Default	Range	Dist.	Conf.
suscept. multiplier	Post-spawning immunosuppression multiplier	2.0	[1.0, 4.0]	U	★
immunosupp. duration	Post-spawning immunosuppression (days)	28	[7, 56]	U	**
min. susceptible age	Days post-settlement before susceptible	0	[0, 180]	U	★

Table 17: Population dynamics parameters (7).

Parameter	Description	Default	Range	Dist.	Conf.
$F_0$	Reference fecundity (eggs)	$10^7$	$[10^6, 10^8]$	LU	*
$\gamma_{\text{fert}}$	Fertilization kinetics parameter	4.5	$[1.0, 10.0]$	U	*
$s_0$ (settler survival)	Beverton–Holt settler survival	0.03	$[0.005, 0.10]$	LU	*
$\alpha_{\text{SRS}}$	SRS Pareto shape	1.35	$[1.0, 1.8]$	U	**
senescence age	Senescence onset age (yr)	50.0	$[20.0, 80.0]$	U	*
$k_{\text{growth}}$	von Bertalanffy growth rate ( $\text{yr}^{-1}$ )	0.08	$[0.03, 0.15]$	U	*
$L_{\min, \text{repro}}$	Minimum reproductive size (mm)	400.0	$[200.0, 500.0]$	U	*

Table 18: Genetics module parameters (8). The three-trait partition is constrained:  $n_{\text{resistance}} + n_{\text{tolerance}} + n_{\text{recovery}} = 51$ .

Parameter	Description	Default	Range	Dist.	Conf.
$n_{\text{resistance}}$	Number of resistance loci	17	{5, 10, 17, 25, 30}	D	★★
$n_{\text{tolerance}}$	Number of tolerance loci	17	{5, 10, 17, 25, 30}	D	★★
target_mean_r	Target mean resistance at $t = 0$	0.15	[0.05, 0.30]	U	★
target_mean_t	Target mean tolerance at $t = 0$	0.10	[0.02, 0.30]	U	★
target_mean_c	Target mean recovery at $t = 0$	0.02	[0.02, 0.25]	U	★
$\tau_{\max}$	Max tolerance mortality reduction	0.85	[0.30, 0.95]	U	★
$q_{\text{init}, \beta_a}$	Beta shape $a$ for allele freq. init.	2.0	[1.0, 5.0]	U	★
$q_{\text{init}, \beta_b}$	Beta shape $b$ for allele freq. init.	8.0	[3.0, 15.0]	U	★

Table 19: Spawning module parameters (7).

Parameter	Description	Default	Range	Dist.	Conf.
$p_{\text{spont,f}}$	Daily spontaneous female spawning prob.	0.012	[0.005, 0.025]	U	**
$p_{\text{spont,m}}$	Daily spontaneous male spawning prob.	0.0125	[0.005, 0.025]	U	**
$\kappa_{\text{fm}}$	Female→male cascade induction prob.	0.80	[0.40, 0.95]	U	**
$\kappa_{\text{mf}}$	Male→female cascade induction prob.	0.60	[0.10, 0.60]	U	**
$\sigma_{\text{spawn}}$	Spawning peak width (std dev, days)	60.0	[30.0, 90.0]	U	**
readiness ind. prob.	Social spawning readiness induction	0.50	[0.10, 0.80]	U	*
female max bouts	Max spawning bouts per female per season	2	{1, 2, 3}	D	**

Table 20: Spatial module parameters (3).

Parameter	Description	Default	Range	Dist.	Conf.
$D_L$	Larval dispersal scale (km)	400.0	[100.0, 1,000.0]	LU	★
$\alpha_{\text{self,fjord}}$	Larval self-recruitment (fjord)	0.30	[0.10, 0.50]	U	★
$\alpha_{\text{self,open}}$	Larval self-recruitment (open coast)	0.10	[0.02, 0.20]	U	★

Table 21: Pathogen evolution module parameters (6).

Parameter	Description	Default	Range	Dist.	Conf.
$\alpha_{\text{kill}}$	Death rate scaling exponent	2.0	[1.0, 4.0]	U	★
$\alpha_{\text{shed}}$	Shedding rate scaling exponent	1.5	[0.5, 3.0]	U	★
$\alpha_{\text{prog}}$	$I_1 \rightarrow I_2$ progression scaling exp.	1.0	[0.5, 2.0]	U	★
$\gamma_{\text{early}}$	Early shedding attenuation factor	0.3	[0.0, 1.0]	U	★
$\sigma_{v,\text{mut}}$	Virulence mutation step size (std dev)	0.02	[0.005, 0.10]	LU	★
$v_{\text{init}}$	Initial pathogen virulence	0.5	[0.2, 0.8]	U	★